# Josephson Plasma Phenomena in High Temperature Superconductor $Bi_2Sr_2CaCu_2O_{8+\delta}$

Itsuhiro Kakeya

Dissertation in Physics

Osaka University
Graduate School of Science
Toyonaka, Osaka

March, 1998

| | | |
|---|---|---|
| **Promoters:** | Prof. K. Kindo | KYOKUGEN, Osaka University |
| | Prof. K. Kadowaki | University of Tsukuba |
| **Referees:** | Prof. Y. Miyako | Graduate School of Science |
| | Prof. S. Kawarazaki | Graduate School of Science |
| | Prof. Y. Akutsu | Graduate School of Science |

## abstract

A systematic study of the Josephson plasma phenomena in high temperature superconductor $Bi_2Sr_2CaCu_2O_{8+\delta}$ was performed using microwave resonance technique.

The Josephson plasma is a new state of matter discovered in highly layered superconducting systems such as high temperature superconductors and is known to be collective oscillations among Cooper pairs, which tunnel through the weakly coupled Josephson junction. The collective excitations are, in general, known to possess two proper modes, one of which is longitudinal and one of which is transverse mode. In previous studies of the Josephson plasma, however, no attention had been paid concerning these two modes. We have succeeded in observing the Josephson plasma resonance at microwave frequency region in $Bi_2Sr_2CaCu_2O_{8+\delta}$ and achieved to separate these modes clearly using the difference of the dispersion relation of the modes. In practice, this was performed by making use of the sample size dependence of the two modes, which can be excited by the different configurations of the microwave electromagnetic fields $\boldsymbol{E}_{\rm rf}$ and $\boldsymbol{H}_{\rm rf}$. As a result, the longitudinal Josephson plasma mode is clearly separated in the condition of $\boldsymbol{E}_{\rm rf} \parallel c$ from the transverse mode that is observable only in the condition of $\boldsymbol{H}_{\rm rf} \parallel ab$. This separation of two modes implies that the Nambu-Goldstone mode, which is the Goldstone mode associated with superconducting phase transition is observed for the first time.

The vortex state of high temperature superconductors is also fascinating subject for investigations in relation to the Josephson plasma phenomena. Since the Josephson plasma senses the difference of the interlayer phase coherence, the Josephson plasma resonance techniques can provide us with a new experimental tool for studying dynamical nature of vortex state. This is very important, since most of studies done are related with the static properties, and therefore the Josephson plasma is a complementary experimental technique. Introducing the general scaling law in the anisotropic superconductors, a universal picture is given for the results of the Josephson plasma resonance as functions of external field direction, temperature, and irradiation dose. In the vicinity of the $ab$ plane, however, it turned out that the general scaling law is violated gradually as the field approaches to the $ab$ plane. The angle where the deviation occurs from the scaling law depends on the degree of the coupling strength determined by the effective anisotropy parameter $\alpha$. Using the $\alpha$ parameter, it is proposed that the vortex phases as functions of temperature and field can be described coherently and transportantly.

# Contents

# Chapter 1

# Introduction

Plasma is one of the most fundamental phenomena which can exist in whatever substances because there is no electron which does not interact with any other electrons at all. In a solid, a contribution of the electron-electron interaction to the whole Hamiltonian provides one of the most important factor which makes solid state physics fascinating, and the plasma oscillation is a unique phenomenon as an elementary excitation derived from the electron-electron interaction.

The plasma oscillation is the collective oscillation of the density of electron gas due to the long-range Coulomb interaction. The plasma oscillation is realized without interactions between the electrons as well as the classic plasma (ionized gas). A plasmon, a quantum of the plasma oscillation, is well defined in the long wavelength limit as a longitudinal excitation in a solid, and described by a longitudinal dielectric function $\epsilon(\omega, \boldsymbol{k})$, which provides not only the dielectric response of the system but also total representation of the electron system despite of its simplicity [1]. The plasmon energy is obtained by zeros of the dielectric function, so that we can comprehend the nature of the electron system by investigations of the plasma or plasmon.

Plasma in a superconductor has more exciting physical meanings. The superconducting plasma which is the Nambu-Goldstone mode with spontaniously symmetry breaking [2, 3] resolves problem of the gauge invariance for a longitudinal electromagnetic excitations in the BCS theory [4, 5]. Although the plasma of Cooper pairs is really important to understand the superconductivity, the gap of the plasma mode is so large comparing to the superconducting gap that the plasma mode cannot be observed due to damping of the quasi-particles. Since then, it had been believed that the plasma mode of the superconducting electrons is unobservable.

In 1990, after the discovery of high-$T_c$ superconductors, Fertig and Das Sarma pointed out theoretically that a longitudinal plasma mode in high-$T_c$ superconductors may lie inside the superconducting gap for their strongly layered structure [6]. Subsequently, a plasma edge in $La_{2-x}Sr_xCuO_4$ [7] and a magnetoabsortive phenomenon in $Bi_2Sr_2CaCu_2O_{8+\delta}$ [8] were observed and interpreted as Josephson plasma phenomena due to the existence of weak Josephson couplings in the substances [9, 10]. Therefore, the Josephson plasma is a unique collective excitation occurring in a superconducting system, that is a Nambu-Goldstone mode which has not been confirmed experimentally in the field of superconductivity.

In this thesis, the Josephson plasma phenomena studied in the course of graduate study during two years is described in the following plans;

**Chapter 2** The notion and the formulations of the Josephson plasma (resonance) are intro-

duced in detail. The description is started from the derivation of the dielectric function of the free electron gas, and the controversy about the superconducting collective excitations around BCS is dealt. Finally, we arrive at the formulation of the Josephson plasma in highly anisotropic layered superconductors.

**Chapter 3** The experimental techniques and principles are given. We employ a microwave bridge balance circuit with a cavity resonator for the measurement. The sample preparation is also described.

**Chapter 4** Mode separation of the two Josephson plasma modes (longitudinal and transverse) is described on the basis of the recent theory of the Josephson plasma: Maxwell's equations for electricity and magnetism in cooperated with intrinsic Josephson effect in $Bi_2Sr_2CaCu_2O_{8+\delta}$. A particular configurations of microwave $\boldsymbol{E}_{\rm rf}$ and $\boldsymbol{H}_{\rm rf}$ vectors and sample are examined and confirmed to excite the longitudinal and the transverse Josephson plasma independently in excellent accord with the dispersion relation calculated theoretically.

**Chapter 5** The Josephson plasma resonance has been studied in the vortex state of $Bi_2Sr_2CaCu_2O_{8+\delta}$ as functions of temperature, field direction, and interlayer coherency of the sample. Josephson plasma resonance is a sensitive probe of the interlayer coherency in the vortex state of high-$T_c$ superconductors, so we expect that the behavior of the Josephson plasma resonance is strongly affected by introducing columnar defects which enhance the interlayer coherency by pinning aligned with the $c$ axis. As a typical case, we have studied the Josephson plasma resonance in a vortex state of $Bi_2Sr_2CaCu_2O_{8+\delta}$ with columnar defects. The results show that the strong coherent vortex state is realized below $T^* \simeq 80$ K irrespective of irradiation doses. Above $T^*$ close similarity in the dynamics of vortex states between dosed and pristine sample is found. We also present data for $\boldsymbol{H} \parallel ab$ as a function of temperature, which requires to be accounted for by theoretical studies.

# Bibliography


[1] D. Pines, *Elementary Excitations in Solids*, Benjamin, 1964.

[2] Y. Nambu, Phys. Rev. **111**, 648 (1960).

[3] J. Goldstone, A. Salam, and S. Weinberg, Phys. Rev. **127**, 965 (1962).

[4] P. W. Anderson, Phys. Rev. **110**, 827 (1958).
P. W. Anderson, Phys. Rev. **112**, 1900 (1958).

[5] J. R. Schrieffer, *Theory of superconductivity*, Addison-Wesley, 1964.

[6] H. A. Fertig and S. Das Sarma, Phys. Rev. B **44**, 4480 (1991).

[7] K. Tamasaku, Y. Nakamura, and S. Uchida, Phys. Rev. Lett. **69**, 1455 (1992).

[8] Ophelia K. C. Tsui, N. P. Ong, Y. Matsuda, Y. F. Yan, and J. B. Perterson, Phys. Rev. Lett. **73**, 724 (1994).

[9] M. Tachiki, T. Koyama, and S. Takahashi, Phys. Rev. B **50**, 7065 (1994).

[10] L. N. Bulaevskii, M. P. Marley and M. Tachiki, Phys. Rev. Lett. **74**, 801 (1995)

# Chapter 2

# Plasma

## 2.1 Solid state plasmon in the context of elementary excitations

Whenever we discuss a solid which consists of $10^{23}$ atoms par $cm^3$, the many-body problem has to be considered. In such a situation, the rigorous solution cannot be obtained, so that we have to introduce approximations which are reasonable for the facing problem. A picture that a solid is regarded as a collection of independent elementary excitations is one of the best approximation.

A requirement for the picture is that the elementary excitation has a well-defined energy. If the elementary excitation is described by its momentum, that means the system has translation invariance, the energy of the excitation is expressed as

$$\tilde{\xi}_p = \xi_p - i\gamma_p, \tag{2.1}$$

where $\gamma_p$ is the imaginary part of the energy, which is proportional to the inverse of the lifetime of the elementary excitation. A long lifetime is necessary for existence of a well-defined elementary excitation, thus the imaginary part should be much smaller than the real part $\xi_p$:

$$\gamma_p \ll \xi_p. \tag{2.2}$$

We can approximate the basic Hamiltonian of a solid as

$$\mathcal{H} = \mathcal{H}_{\text{ion}} + \mathcal{H}_{\text{electron}} + \mathcal{H}_{\text{electron-ion}}. \tag{2.3}$$

Here $\mathcal{H}_{\text{ion}}$ denotes the Hamiltonian of a group of ions, and represents interactions by the potential $V(\boldsymbol{R}_i - \boldsymbol{R}_j)$ which depends on only the distance between the ions. $\mathcal{H}_{\text{electron}}$ denotes the Hamiltonian of valence electrons, and dominated by Coulomb interactions between the electrons. Finally, $\mathcal{H}_{\text{electron-ion}}$ denotes the interactions between the electrons and the ions.

When we are interested in the interaction between electrons in a solid, only $\mathcal{H}_{\text{electron}}$ should be considered and the effects of ion cores are replaced with a positively charged uniform background. In this system, the Coulomb interaction yields a collective excitation of the electron density, that is plasma oscillation. As discussed later, the frequency of the oscillation is given by the plasma frequency described in the long wavelength limit as

$$\omega_p = \left(\frac{4\pi n e^2}{m}\right)^{1/2}, \tag{2.4}$$

where $n$ is the electron density. The plasma oscillation directly corresponds to a oscillation of the classical ionized gas commonly called plasma since the interaction between the particles is indispensable for both of the plasmas. The plasma oscillation is quantized to the *plasmon*, which is a sort of bosons and has a characteristic distribution function for bosons as

$$f_p(T) = \frac{1}{\exp[\beta\xi_p] - 1} \tag{2.5}$$

with $\beta = 1/k_{\mathrm{B}}T$.

Although the plasmon is not a perfectly well-defined elementary excitation, Eq. (2.2) is satisfied in the long wave-length limit because the imaginary part of the energy of a plasmon with a momentum $\boldsymbol{p}$ is proportional to $(p/p_F)^2\omega_p$. As a result, the plasmon is not damped and established as a certain elementally excitation.

## 2.2 Electromagnetic response of normal electrons

In the case that we discuss the screening effect between electrons such as the plasmon in metals, a formalism which describe the longitudinal response of the electron gas is needed. Thus we introduce here the dielectric function $\epsilon(\omega, \boldsymbol{k})$ as the formulation of the electron gas. Considering $\epsilon(\omega, \boldsymbol{k})$, not only the dielectric response but also much more information about the nature of the electron gas. Actually, $\epsilon(\omega, \boldsymbol{k})$ is recognized the notion which unifies various theories of the electron gas.

### 2.2.1 Dielectric function of materials

The dielectric constant $\epsilon$ of the electrostatics is defined in terms of the electric field $\boldsymbol{E}$ and the polarization $\boldsymbol{P}$, the electric flux density (electric displacement) $\boldsymbol{D}$ as

$$\boldsymbol{D} = \boldsymbol{E} + 4\pi\boldsymbol{P} = \epsilon\boldsymbol{E}. \tag{2.6}$$

This means that the dielectric constant $\epsilon$ represents how easily the electron system is polarized by applying unit electric field, and therefore it is purely material's parameter. Table 2.1 gives a list of the dielectric constant of various substances common to us. Since the electric polarizability of the materials depends on the microscopic dynamics of electrons constituting of the substance, it is easily to expect that the dielectric constant should exhibit frequency dependence in alternating electric field. The values shown in Table 2.1 are all for a low frequency limit.

#### Description of metals in terms of $\epsilon$

The characters of metals are existence of mobile electrons, which respond to the applied electric field $\boldsymbol{E}$ and shield the effect of the electric field very well at low frequency and in the long wave length limit. The long wavelength dielectric response $\epsilon(\omega, 0)$ or $\epsilon(\omega)$ of an electron gas is obtained from the equation of motion of a free electron in an electric field $\boldsymbol{E}$:

$$m\frac{d^2x}{dt^2} = -eE. \tag{2.7}$$

| Material | $\epsilon$ |
|---|---|
| $Al_2O_3$ | 8.5 |
| sapphire | 9.4 |
| diamond | 5.68 |
| polyethylene | 2.2-2.4 |
| benzene | 2.28 |
| water | 80.26 |
| Liq. $N_2$ | 1.45 |
| Liq. He | 1.048 |
| $O_2$ (gas) | 1.06055 |

Table 2.1: Dielectric constants for various materials. These values are all for low frequency limit.

Provided $x$ and $E$ have the time dependence $\exp[-i\omega t]$, the polarization, defined as the dipole moment per unit volume, is given by

$$P = -nex = -\frac{ne^2}{m\omega^2}E, \tag{2.8}$$

where $n$ is the electron concentration.

The dielectric function at frequency $\omega$ is

$$\epsilon(\omega) \equiv \frac{D(\omega)}{E(\omega)} = 1 + 4\pi\frac{P(\omega)}{E(\omega)}. \tag{2.9}$$

The dielectric function of the free electron gas follows from Eqs. (2.8) and (2.9):

$$\epsilon(\omega) = 1 - \frac{4\pi ne^2}{m\omega^2} = 1 - \frac{\omega_p^2}{\omega^2}, \tag{2.10}$$

where plasma frequency $\omega_p$ is defined by the relation

$$\omega_p \equiv \left(\frac{4\pi ne^2}{m}\right)^{1/2}. \tag{2.11}$$

It is noted that the plasma frequency depends only on the density of electron $n$. Equation (2.11) is plotted in Fig. 2.1. If $\omega < \omega_p$, the dielectric function is negative, then incident electromagnetic wave is reflected. On the contrary, in the case of $\omega > \omega_p$, $\epsilon$ is positive and electromagnetic wave is propagate without damping in the substance. For example, plasma frequencies of metals lie in the region of ultraviolet, so that the visible light is almost perfectly reflected.

If the positive ion core background has a dielectric constant $\epsilon(\infty)$ which is essentially constant up to frequencies well above $\omega_p$, then Eq. (2.10) becomes

$$\epsilon(\omega) = \epsilon(\infty) - 4\pi\frac{ne^2}{m\omega^2} = \epsilon(\infty)\left[1 - \frac{\tilde{\omega}_p^2}{\omega^2}\right], \tag{2.12}$$

where $\tilde{\omega}_p$ is defined as

$$\tilde{\omega}_p^2 = 4\pi ne^2/\epsilon(\infty)m. \tag{2.13}$$

Notice that $\epsilon = 0$ at $\omega = \tilde{\omega}_p$.

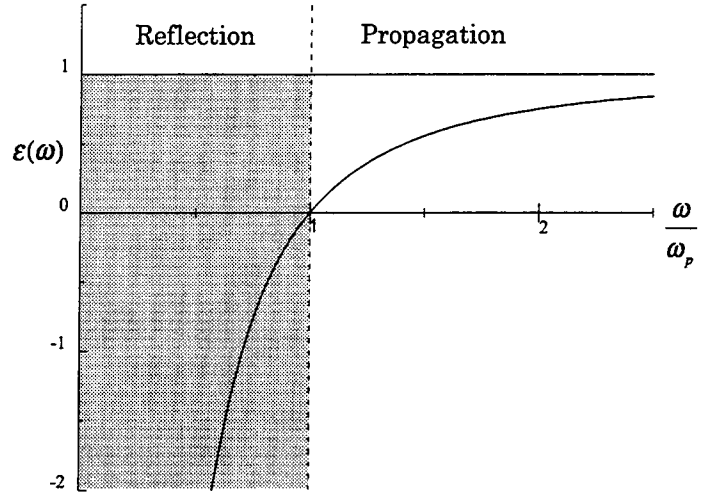


Figure 2.1: Dielectric function $\epsilon(\omega)$ of a free electron gas plotted versus frequency in units of the plasma frequency $\omega_p$. Incident electromagnetic wave propagates without damping when $\epsilon > 0$. and are reflected when $\epsilon < 0$.

### Eelectromagnetic waves in plasma

Electromagnetic phenomena in plasma can be described by the Maxwell equation (in CGS Gaussian unit):

$$\nabla \times \boldsymbol{H} = \frac{4\pi}{c}\boldsymbol{i} + \frac{1}{c}\frac{\partial \boldsymbol{D}}{\partial t} \quad \text{Ampére's law,} \tag{2.14}$$

$$\nabla \times \boldsymbol{E} = -\frac{1}{c}\frac{\partial \boldsymbol{B}}{\partial t} \quad \text{Faraday's law,} \tag{2.15}$$

$$\nabla \cdot \boldsymbol{E} = 4\pi\rho, \tag{2.16}$$

with

$$\begin{cases} \boldsymbol{i} = \sigma \boldsymbol{E}, \\ \boldsymbol{D} = \boldsymbol{E} + 4\pi \boldsymbol{P} = \epsilon \boldsymbol{E}, \\ \boldsymbol{B} = \boldsymbol{H} + 4\pi \boldsymbol{M} = \mu \boldsymbol{H}, \\ c = 2.99793 \times 10^{10} \text{cm/sec}. \end{cases}$$

In a nonmagnetic isotropic medium ($\mu = 1$) the electromagnetic wave equation is obtained by Eqs. (2.14) and (2.15) as

$$\frac{\partial^2 \boldsymbol{D}}{\partial t^2} = c^2 \nabla^2 \boldsymbol{E}. \tag{2.17}$$

We look for a solution with $\boldsymbol{E} \propto \exp[-i\omega t + i\boldsymbol{k} \cdot \boldsymbol{r}]$ and $\boldsymbol{D} = \epsilon(\omega, \boldsymbol{k})\boldsymbol{E}$; then we have the dispersion relation for electromagnetic waves:

$$\omega^2 = \frac{c^2 \boldsymbol{k}^2}{\epsilon(\omega, \boldsymbol{k})}. \tag{2.18}$$

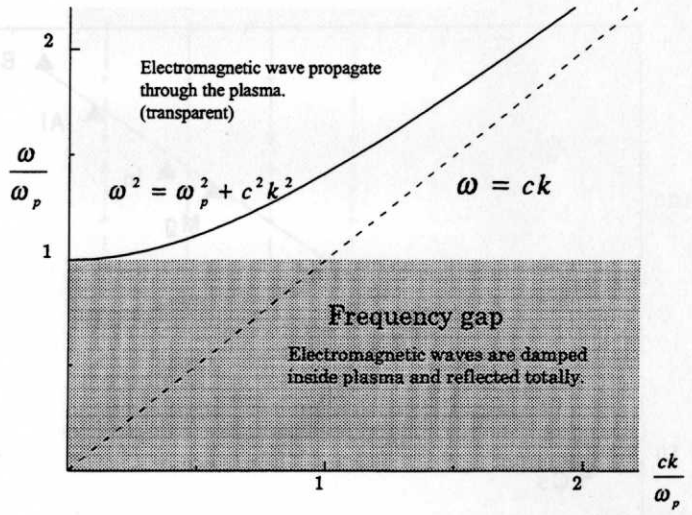


Figure 2.2: Dispersion relation for the transverse electromagnetic waves in plasma. Electromagnetic wave propagates when $\omega > \omega_p$, with $\omega = \sqrt{\omega_p^2 + c^2k^2}$.

| | Li | Na | K | Rb | Cs |
|---|---|---|---|---|---|
| $\lambda_p$, calculated | 1500 | 2100 | 2900 | 3200 | 3600 |
| $\lambda_p$, observed | 2050 | 2100 | 3150 | 3600 | 4400 |

Table 2.2: Ultraviolet transmission limits of alkali metals, in Å. After Mott and Jones [3].

**Dispersion relation in free electron gas**

In free electron gas we use Eq. (2.12) into Eq. (2.6), then one obtain the dispersion for $\epsilon(\omega)$,

$$\epsilon(\omega)\omega^2 = \epsilon(\infty)(\omega^2 - \tilde{\omega}_p^2) = c^2k^2. \tag{2.19}$$

For $\omega < \tilde{\omega}_p$ we have $k^2 < 0$, so that $k$ is imaginary. The solutions of the wave equation are of the form $\exp(-|\boldsymbol{k}|x)$ in the frequency region $0 < \omega \leq \tilde{\omega}_p$. Waves incident on the medium in this frequency do not propagate, but will be totally reflected.

When $\omega > \tilde{\omega}_p$, an electron gas is transparent and the dielectric function is positive real. The dispersion relation in this region may be written as

$$\omega^2 = \tilde{\omega}_p^2 + c^2k^2/\epsilon(\infty); \tag{2.20}$$

this describes transverse electromagnetic waves in plasma (Fig. 2.2).

Since $\omega_p$ depends only on $n$ in the case of free electron gas, the frequency can be estimate as a function of $n$. This is shown in Fig. 2.3. This simple consequence in free electron gas can be compared with the experimental fact first discovered by Wood [1] and explained by Zener [2] that the simple metals should reflect light in the visible region and transparent to ultraviolet light. A comparison of calculated and observed cutoff wavelength is given in Table 2.2 [3].

All electromagnetic phenomena can be understood through this dispersion relation. We now consider various cases corresponding various physical situations in terms of $\epsilon$ with various $\omega$ and $\boldsymbol{k}$.

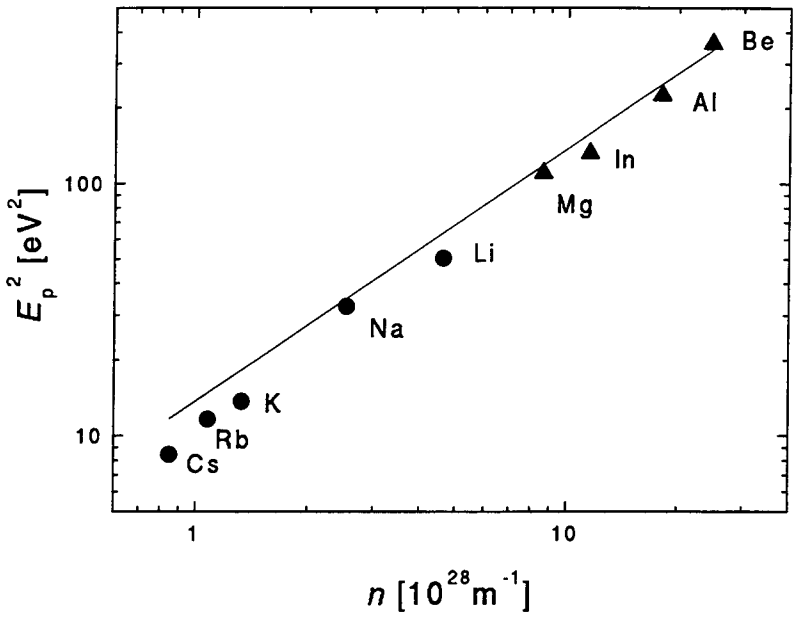


Figure 2.3: A graph plotted square of observed plasma energy $E_p$ versus carrier density $n$. Circles and triangles indicate alkali and transition metals, respectively. After Raether [4] and references therein.

- When $\epsilon$ is real and positive, $\boldsymbol{k}$ is real for $\omega$ being real. In this case, the transverse electromagnetic wave propagates with the phase velocity $c/\sqrt{\epsilon}$.
- When $\epsilon$ is real but negative, then $\boldsymbol{k}$ becomes imaginary for $\omega$ being real. Therefore, the electromagnetic wave propergates with a damping propotional to $\exp[-k''r]$. ($k = k' + ik''$, $k'$ and $k''$ are real)
- When $\epsilon$ is complex, $k$ becomes complex for $\omega$ being real. The waves are damped in space.
- When $\epsilon = \infty$, this means that the plasma has a response in the absence of external forces. Thus, the poles of $\epsilon$ define the frequencies of the free oscillations of the plasma.
- When $\epsilon = 0$, it is noted that the longitudinal waves are possible as shown in the following section.

### Zeros of the dielectric function

As described in the previous section, the zeros of the dielectric function has a special meaning in determining the frequencies of the longitudinal modes of oscillation. That is,

$$\epsilon(\omega_L) = 0, \tag{2.21}$$

which determines the longitudinal plasma oscillation frequency $\omega_L$.

Since the dielectric function of this mode is zero, the total dielectric flux density $\boldsymbol{D}$ must be zero. Therefore,

$$\boldsymbol{E} = -4\pi\boldsymbol{P}. \tag{2.22}$$

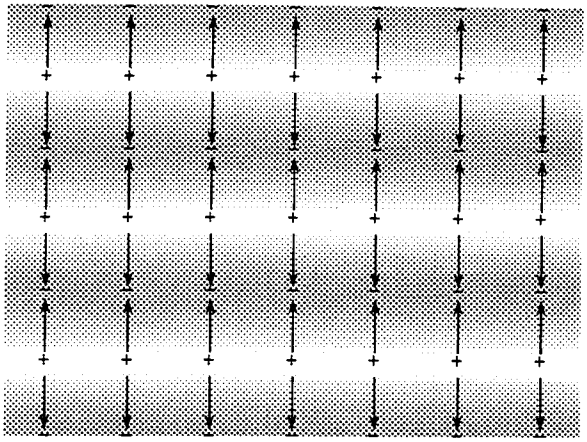

Figure 2.4: A longitudinal plasma oscillation. The arrows indicate the direction of displacement of the electrons.

This means that there is an oscillating depolarization field due to $\boldsymbol{P}$ in a manner shown in Fig. 2.4. For a free electron gas, at zero of the dielectric function

$$\epsilon(\omega_L) = 1 - \omega_p^2/\omega_L^2 = 0, \tag{2.23}$$

whence $\omega_L = \omega_p$. Thus there is a free longitudinal oscillation mode similar to Fig. 2.4 of an electron gas at the plasma frequency described by Eq. (2.19) as the low-frequency cutoff of transverse electromagnetic waves.

As a special case a longitudinal plasma oscillation with $k = 0$ is shown in Fig. 2.5 as a uniform displacement of an electron gas in a thin metallic slab. The electron gas is shifted as a whole with respect to the positive ion background. The displacement $u$ of the electron gas creates an electric field $E = 4\pi neu$ that acts as a restoring force on the gas.

The equation of motion of a unit volume of the electron gas of concentration $n$ is

$$nm\frac{d^2u}{dt^2} = -neE = -4\pi n^2e^2u \tag{2.24}$$

then

$$\frac{d^2u}{dt^2} + \omega_p^2 u = 0, \tag{2.25}$$

with

$$\omega_p = \left(\frac{4\pi ne^2}{m}\right)^{1/2}. \tag{2.26}$$

This equation of motion is for a simple harmonic oscillator of frequency $\omega_p$, the plasma frequency, of which expression is identical with Eq.(2.11), although this is obtained from very different physical situations. It is worth while mentioning that the same plasma frequency $\omega_p$ at $k = 0$ in Eqs. (2.11) and (2.26) arise in a different connection.

### 2.2.2 Plasmons

A plasma oscillation in a metal described by Eq. (2.25) is a collective longitudinal excitation of the conduction electron gas, which is a plasmon. To excite a plasmon, a technique passing

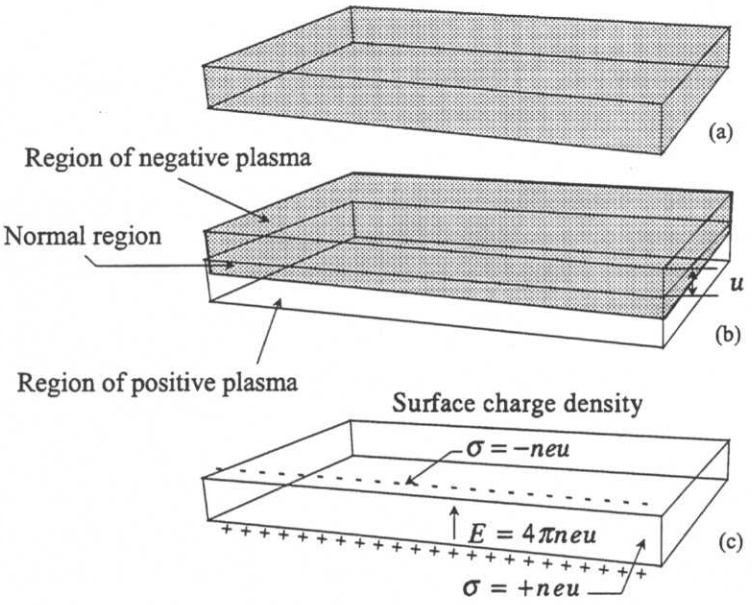


Figure 2.5: In (a) a thin slab or film of a metal with equal number of the positive ion cores and electrons. In (b) the negative charge has been displaced upward uniformly by a small distance $u$, shown exaggerated in the figure. As in (c), this displacement establishes a surface charge density $-neu$ on the upper surface of the slab and $+neu$ on the lower surface, where $n$ is the electron concentration. An electric field $E = 4\pi neu$ is produced inside the slab. This field tends to restore the electron sea to its equilibrium position (a).

| Material | Observed | Calculated $\hbar\omega_p$ | Calculated $\hbar\tilde{\omega}_p$ |
|---|---|---|---|
| *Metals* | | | |
| Li | 7.12 | 8.02 | 7.96 |
| Na | 5.71 | 5.95 | 5.58 |
| K | 3.72 | 4.29 | 3.86 |
| Mg | 10.6 | 10.9 | |
| Al | 15.3 | 15.8 | |
| *Dielectrics* | | | |
| Si | 16.4–16.9 | 16.0 | |
| Ge | 16.0–16.4 | 16.0 | |
| InSb | 12.0–13.0 | 12.0 | |

Table 2.3: Volume plasmon energies of alkali and alkaline-earth metals, and semiconductors. Data are given in a unit of eV. Recall that $\tilde{\omega}_p$ as defined by Eq. (2.13) includes the ion core effects by use of $\epsilon(\infty)$.

an electron through a thin metallic film or by reflecting an electron or photon from a film is commonly used, since charge of the electron couples with the electrostatic field fluctuations of the plasma oscillations. The reflected or transmitted electron will show an energy loss equal to integer multiples of the plasmon energy. A comparison of observed and calculated values of plasmon energies is given in Table 2.3; further data are given in the reviews by Raether [4] and by Daniels [5]. It will be shown later in more detail that microwave can also excite a plasmom in high $T_c$ superconductor $Bi_2Sr_2CaCu_2O_{8+\delta}$ in the superconducting state by making use of highly anisotropic superconducting properties of thin compound. Since the wavelength of the electromagnetic wave at plasma frequency in a conventional metal is a few thousand Ångstroms, it is practically impossible to directly excite the plasmon mode with $\boldsymbol{k} \simeq 0$. A free electron plasma oscillation with a small finite wavevector $\boldsymbol{k}$ can be described by the dispersion relation

$$\omega \simeq \omega_p\Big(1 + \frac{3k^2 v_{\mathrm{F}}^2}{10\omega_p^2} + \cdots\Big), \tag{2.27}$$

where $v_{\mathrm{F}}$ is the Fermi velocity.

We further note that it is possible to excite collective plasma oscillations in dielectric materials; results for several dielectrics are also included in Table 2.3. The calculated plasma energies of Si, Ge, and InSb are based on four valence electrons per atom. In a dielectric the plasma oscillation is physically the same as in a metal: the entire valence electron sea oscillates back and forth with respect to the ion cores [6].

## 2.3 Collective excitations in isotropic superconductors

### 2.3.1 Problem of gauge invariance in BCS theory

The electrical resistivity of many metals and alloys drops suddenly to zero when the specimen is cooled to a sufficiently low temperature, often a temperature in the liquid helium temperature range. This phenomenon, called superconductivity, was observed first by Kamerlingh

Onnes, in Leiden 1911, three years after he first liquefied helium [7]. Subsequently, many experimental and theoretical studies were performed, the most remarkable development was given 45 years after Onnes' discovery. Bardeen, Cooper and Schrieffer [8] — later, we call BCS— presented the microscopic theory of superconductivity, which can achieve remarkably good understanding of the superconducting features for the existence of an energy gap. A mathematical formulation of the BCS theory has been developed in a very elegant way by Bogoliubov [9], who introduced coherent mixtures of particles and holes to describe a superconductor. Such "quasi-particles" are not eigenstates of charge and particle number, and reveal a very bold departure, inherent in the BCS theory, from the conventional approach to many-Fermion problems. However, this creates at the same time certain theoretical difficulties which are matters of principle. Thus the derivation of the Meissner effect in the original BCS theory is not gauge-invariant, as is obvious from the viewpoint of the quasi-particle picture, and posses a serious problem as to the correctness of the results obtained in such a theory.

This question of the gauge invariance has been taken up by many people [10, 11, 12, 13]. In the Meissner effect, one deals with a linear relation between the Fourier components of the external vector potential $\boldsymbol{A}$ and the induced current $\boldsymbol{J}$, which is given by the expression

$$J_i(\boldsymbol{q}) = \sum_{j=1}^{3} K_{ij}(\boldsymbol{q}) A_j(\boldsymbol{q}), \tag{2.28}$$

with

$$K_{ij}(\boldsymbol{q}) = -\frac{e^2}{m}\langle 0|\rho|0\rangle\delta_{ij} + \sum_n \Big( \frac{\langle 0|j_i(\boldsymbol{q})|n\rangle\langle n|j_j(-\boldsymbol{q})|0\rangle}{E_n} + \frac{\langle 0|j_i(-\boldsymbol{q})|n\rangle\langle n|j_j(\boldsymbol{q})|0\rangle}{E_n} \Big). \tag{2.29}$$

$\rho$ and $j$ are the charge and current density, and $|0\rangle$ refers to the superconducting ground states. In the BCS model, the second term vanishes in the limit $\boldsymbol{q} \to 0$, leaving the first term alone to give a non-gauge invariant result. However, that there is a significant difference between the transversal and longitudinal current operators in their matrix elements. Namely, there exist collective excited states of quasi-particle pairs, as was first derived by Bogoliubov [9], which can be exited only by the longitudinal current.

As a result, the second term does not vanish for a longitudinal current, but cancels the first term (the longitudinal sum rule) to produce no physical effect; whereas for transverse field, the original result will remain essentially correct. Therefore longitudinal collective excitations extract gauge invariance of BCS theory, and transverse collective excitations contribute to the Meissner current.

There are now a number of formalisms for including the backflow and the collective mode. One of the simplest way to handle the problem rigorously is to make use of a "Ward-Takahashi's identity [14, 15]," which is the Green's function analysis of the continuity equation. By making approximations which are consistent with this identity, one can ensure local charge conservation and therefore gauge invariance. This approach was first discussed by Nambu [16] and his line of argument is followed in Ref. [17, 18] in detail.

### 2.3.2 Energy gap of the plasma mode

The quasi-particle picture of the collective excited states was firstly derived by Bogoliubov [9] and followed by Anderson [10, 11] using generalized random-phase approximation, so that the excited states are commonly called Anderson-Bogoliubov (AB) mode. In a hypothetical neutral superconductor, AB mode is soft and lies in the superconducting gap $\Delta$ (the details are mentioned in the following section). It can be interpreted either as a first-sound-like mode propagation in the condensate, or as bound electron pairs with nonzero momentum. In the physical case of a charged superconductor, the AB mode is pushed up to high frequencies by the long-range Coulomb interaction, and becomes indistinguishable from the "normal" plasmon in energy [11, 12]. That is, the energy gap of this plasma mode is given by

$$E_g = \hbar\omega_p = \hbar\left(\frac{4\pi n_s e^2}{m^*}\right)^{\frac{1}{2}}, \tag{2.30}$$

where $n_s$ and $m^*$ are the density and effective mass of the quasi-particles. In the case of conventional superconductors, no low-lying plasma mode can be observed for damping of quasi-particles, because the Coulomb gap $E_g$ is the order of 1 eV, which lies far beyond the superconducting gap $\Delta$ of a few meV. Furthermore, if the plasma excitations are observed, the plasma frequency derived from Eq. (2.30) is probably identical to the normal plasmon expressed by Eq. (2.26) (the only difference is the density of carriers), thus the excited state cannot be identified with the AB mode.

### 2.3.3 Spontaneous symmetry breaking in a superconductor

Next, let us consider the superconducting transition in the context of phase transitions in the quantum field theory.

Superconductivity is one of the ordered states, in which phases of wave functions are coherent in a macroscopic range. This situation is the same as ferromagnetism of magnets in a sense of destruction of symmetry; the phases of wave functions in superconductivity and the directions of magnetic moments in ferromagnetism lose a rotation symmetry accompanied with the ferromagnetic transitions. In the field theory, a destruction of symmetry with phase transition is known to be as a "spontaneous symmetry breaking."

Nambu [19] and Goldstone [20] have examined that any spontaneously symmetry broken systems have low-lying and continuous collective excitations which tend to zero in the limit of $k \to 0$. This theorem (Nambu-Goldstone theorem) was proved by Goldstone *et al.* [21], and the collective excitation is called Nambu-Goldstone mode. Nambu-Goldstone (NG) mode appears as many practical examples in condensates, such as a spin wave (magnon) in a ferromagnet, which has the dispersion relation of $\omega \propto k^2$.

In a superconductor, the longitudinal collective excitation is the NG mode, (the transverse mode contributes the Meissner effect). Taking the Coulomb interaction into account, NG field $\chi$ satisfies equations

$$\left[\frac{\partial^2}{\partial t^2} - v_B^2(\nabla^2)\nabla^2 + e^2\eta^2(\nabla^2)v_B^2(\nabla^2)\right]\chi = 0, \tag{2.31}$$

$$\nabla^2\chi = 0, \tag{2.32}$$

where $v_B(\nabla^2)$ is defined by the NG boson energy $\omega_k$ with $\omega_k^2 = v_B(-k^2)k^2$, and $\eta(\nabla^2)$ is a differential operator which satisfies $\eta(0) = 1/c$ with $c$ being a complex number [22]. Equation

(2.31) gives the plasma frequency $\omega_p = e\eta(0)v_B(0)$ in low $k$ limit, and Eq. (2.32) gives $\chi$ at zero momentum[1]. This means that NG mode is pushed up into the plasma mode by Coulomb interaction except for $k = 0$, and this mechanism is named Anderson-Higgs-Kibble (AHK) mechanism [10, 23, 24]. Hence, we can understand that the longitudinal plasma mode in superconductors is a Nambu-Goldstone mode with a finite plasma gap which originate from AHK mechanism. It is noted that the plasma mode is quantized to a "phason" mode.

## 2.4 Plasma excitation in high-$T_c$ superconductors

Now, ten years after the discovery of high-temperature superconductors by Bednorz and Müller [25], we have a consensus that the superconductivity in copper oxide compounds is due to the Cooper pairs concentrated to the $CuO_2$ planes. This picture was derived from the crystal structure, and the extremely short perpendicular coherence length $\xi_\perp$, which is subatomic range.

Anisotropic layered superconductors such as transition-metal dichalcogenides and their intercalated compounds ($NbSe_2$, $TaS_2$, $TaSe_2$), the organic superconductors (the Bechgaard salts and the BEDT-TTF family), and artificial multilayers (Nb-Cu, Nb-$NbO_x$, Pb-Ge, Au-Ge, Pb-Au) have been under research since the early 1970s [26, 27, 28]. In all of the structures, superconducting layers alternate with weakly superconducting, normal or even insulating layers. In some of the compounds, the Ginzburg-Landau coherence length perpendicular to the layers is comparable or smaller than the interlayer spacing, so that these materials cannot be treated simply as extremely anisotropic but still homogeneous materials. Even in a perfect single crystal, the amplitude of the superconducting order parameter should vary strongly between the layers. This situation, which is well known from Josephson junctions, leads to the ideas that, at least for the most anisotropic materials, the superconducting layers are coupled by the Josephson effect. A macroscopic theory for such system has been proposed by Lawrence and Doniach [29]. The theory was quite successful in explaining various physical phenomena in layered superconductors.

### 2.4.1 Historical surveys of the Josephson plasma

The pioneering work on collective excitations in layered superconductors was given by Fertig and Das Sarma [30]. From the analogy of their studies in layered semiconductors [31, 32], they pointed out the collective (plasma) excitation mode of the well-layered superconductors can be less than the gap $\Delta$, because the tunneling of quasi-particles between planes is small enough. Mishonov also predicted plasma excitations in $Bi_2Sr_2CaCu_2O_{8+\delta}$ (BSCCO) with an electric field polarized perpendicular to the $CuO_2$ plane [33]. He remarked at the giant effective-mass anisotropy $m_c/m_a \cong 3000$ obtained by magnetometry [34], and was motivated a plasma edge measurement at a far-infrared frequency region in polycrystalline high-$T_c$ samples by Noh *et al.* [35].

The first observation of the plasma edge in single crystalline high-$T_c$ materials was reported by Tamasaku *et al.* [36] in the $c$ axis polarized infrared reflectivity measurements on high-quality single crystal $La_{2-x}Sr_xCuO_4$ (LSCO). The spectrum below $T_c$ shows a distinct edge around 50 $cm^{-1}$, which is much lower than the estimated BCS gap $2\Delta = 3.56T_c \sim 150$

[1]Solutions of this Laplace equation (2.32) lead vortices in the superconducting mixed state. See chapter 6 in Ref. [22].

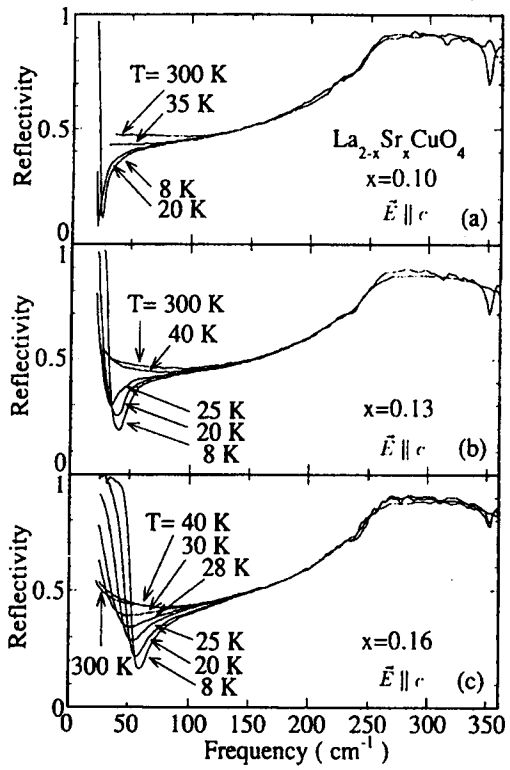


Figure 2.6: Infrared reflectivity spectra of $La_{2-x}Sr_xCuO_4$ with polarization perpendicular to the $CuO_2$ planes ($\boldsymbol{E} \parallel c$) above and below $T_c$ for (a) $x = 0.10$ ($T_c = 27$ K), (b) $x = 0.13$ ($T_c = 32$ K), and (c) $x = 0.16$ ($T_c = 34$ K). After Tamasaku *et al.* [36].

$cm^{-1}$, and changes drastically above $T_c$ (Fig. 2.6). This result was interpreted by the plasma edge which is due to the coherent conduction of supercurrents along the $c$ axis. This experimental fact implies that the Josephson effect drives the interlayer ($c$ axis) superconducting current. Subsequently, Tachiki *et al.* [37] concluded that the plasma excitation is characteristic of the high-$T_c$ superconductors which have layered structures through a systematic calculation of electromagnetic responses in Josephson coupling multi-layered superconductors.

Although this view of superconductors as a sequence of intrinsic Josephson junctions had already been implied by several researchers, its striking confirmation was firstly reported by Kleiner *et al.* on BSCCO and $Tl_2Bi_2Ca_2Cu_3O_{10}$ (TBCCO) small single crystals [38, 39]. The current-voltage ($I - V$) characteristics exhibit large hysteresis and multiple branches, which are the same number of $CuO_2$ layers. Moreover, $I$–$V$ characteristics under microwave irradiation show multiple steps which determined by the number of Josephson junctions and microwave frequency (Shapiro step). These experiments have unambiguously revealed the superconductor-insulator-superconductor (SIS) tunneling character of the $c$ axis transport current in highly anisotropic superconductors. Thus they presented an attractive idea that these materials are equivalent to the stacked Josephson junction arrays in which Josephson junctions exist as many as insulating ($Bi_2O_2$ in BSCCO) layers. The crystal structure of BSCCO is shown in Fig 2.7. Similar experimental phenomena had been observed in several other experiments [40, 41, 42], and the idea was recognized as the basic notion in the high-

temperature superconductor.

In 1994, Tsui *et al.* discovered a broad electromagnetic resonance in the surface impedance measurements of BSCCO as a function of perpendicular external magnetic field ($\boldsymbol{H}_{\rm ext} \parallel c$) in a microwave frequency range (30-60GHz) [43]. The resonance lines obtained by them is represented in Fig. 2.8. Despite that the detail configuration of RF electromagnetic field around the sample is arbitrary since the sample was simply put on the inside of the waveguide in this experiment, several new experimental features were revealed:

1. A surface impedance has an anomaly (a kind of resonance) and it appears in the finite magnetic field.

2. The frequency dependence of the resonance field $\boldsymbol{H}_{\rm res}$ shows an anti-cyclotronic behavior.

3. The temperature dependence of $\boldsymbol{H}_{\rm res}$ exhibits a cusp, which corresponds to the irreversibility line[2] of the specimen.

Similar experiment with theirs was performed by using a microwave cavity. Matsuda *et al.* [44] can remove the ambiguity concerning the RF fields. They observed a sharp resonance in perpendicular RF electric filed ($\boldsymbol{E}_{\rm rf} \parallel c$). Therefore, the resonance is interpreted by the Josephson plasma resonance, which is a unique phenomenon of the system of Josephson coupled superconducting multilayer, as suggested by Bulaevskii *et al.* [45], and Tachiki *et al.* [46]. In particular, the latter authors pointed out that the Josephson plasma has two different modes —longitudinal and transverse— considering the charge screening length $\mu$ which is neglected in the treatment of conventional Josephson junctions. We will follow their line in the following Sec.2.4.3.

### 2.4.2 Single Josephson junction

Before discussing Josephson plasma in high-$T_c$ superconductors in more detail, we first consider a single Josephson junction to help understanding Josephson plasma to distinguish it from conventional plasma. The point to be considered first, is that charged particles concerned with the Josephson plasma are not the whole electrons but only the Cooper pairs passing through the weak Josephson coupling. Physically, we should consider a single Josephson junction as follows. Figure 2.9 shows a system in which two layered superconductors A, B are coupled with a medium of insulating layer which has a thickness of $d$ and a dielectric constant of $\epsilon$. In this system, Cooper pairs can move from A to B and vice versa, since the wave functions in A and B penetrate into the insulating layer and interfere each other.

In 1962, Josephson predicted that the tunneling current of Cooper pairs through weak coupling can be described by [47]

$$I = I_{\rm c} \sin \Delta\varphi, \tag{2.33}$$

when $I_{\rm c}$ is the maximum current through barriers and $\Delta\varphi$ is the phase difference between the two superconductors. Applying the Ginzburg-Landau theory, the maximum current density $j_{\rm cr}$ can be expressed as

$$j_{\rm cr} = \frac{2e\hbar n_s}{m^* d^2} = \frac{I_{\rm c}}{A}, \tag{2.34}$$

[2]The irreversibility line separets the $B-T$ phase diagram into two regions, where the manetization curve has no hysteresis abve the line and it has hysterisis below the line. See Ref. [28].

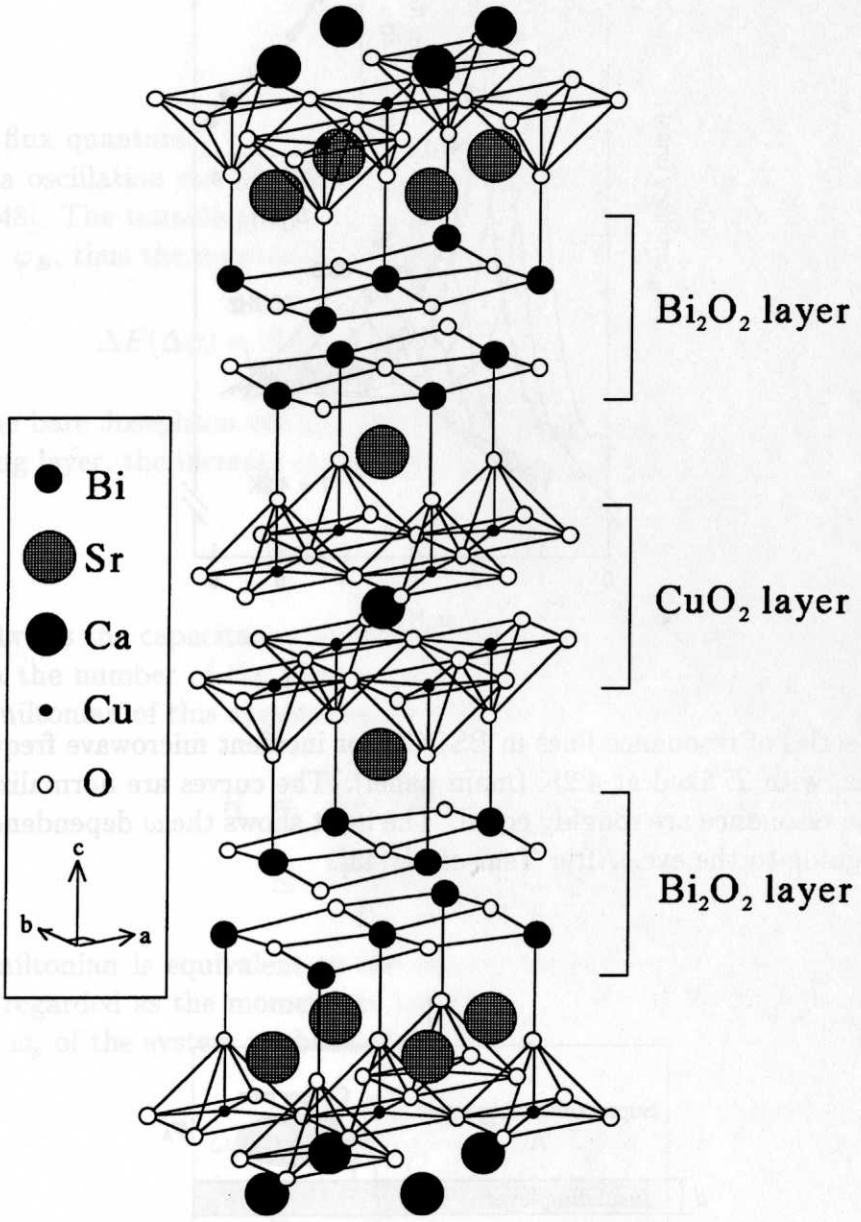


Figure 2.7: Crystal structure of $Bi_2Sr_2CaCu_2O_{8+\delta}$. Superconducting $CuO_2$ layers are well separated by semiconductive $Bi_2O_2$ layers.

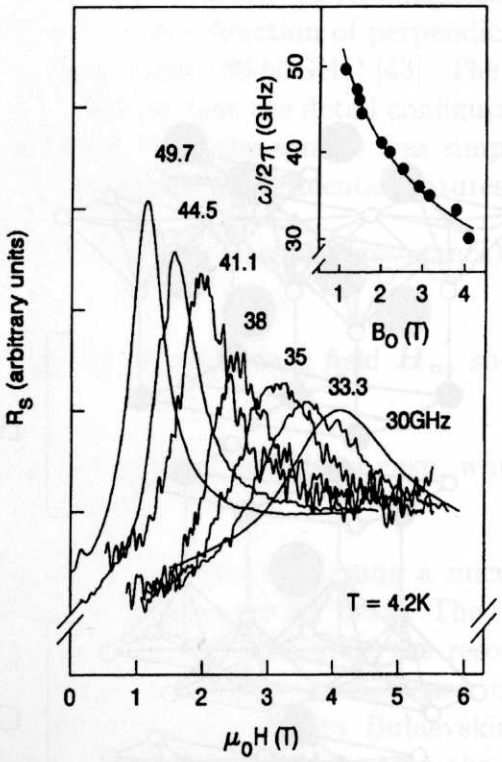


Figure 2.8: A series of resonance lines in BSCCO for incident microwave frequency between 30 and 50 GHz, with $T$ fixed at 4.2K (main panel). The curves are normalized so that the areas under the resonance are roughly equal. The inset shows the $\omega$ dependence of $B_{\rm res}$. The solid line is a guide to the eye. After Tsui *et al.* [43].

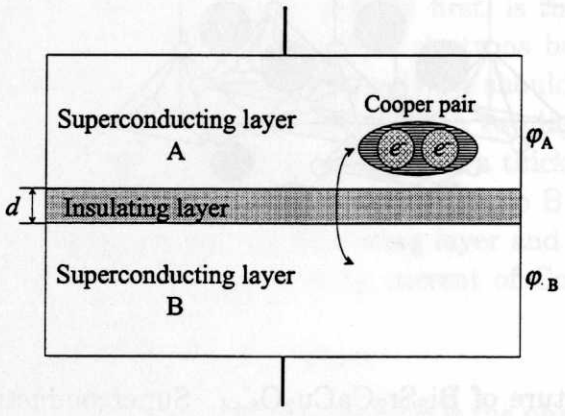


Figure 2.9: Schematic diagram of a sigle Josephson junction. Only Cooper pairs can pass through the junction, and drives Josephson plasma. $\varphi_A$ and $\varphi_B$ indicate phases of order parameters of superconductor A and B, respectively.

where $A$ is the area of junction, $n_s$ is the superconducting Cooper pair density, $m^*$ is the effective mass of the pair perpendicular to the junction, $d$ is the distance between two superconducting layers. The penetration depth of current along the the junction $\lambda_J$ associated with the tunneling current density $j_{\rm cr}$ is expressed by

$$\lambda_J = \sqrt{\frac{c\phi_0}{8\pi^2 j_{\rm cr} d}}, \tag{2.35}$$

with $\phi_0$ being flux quantum.

The plasma oscillation can be determined in a simple Josephson junction as described by Anderson [48]. The tunneling of Cooper pairs yields the phase difference between A and B, $\Delta\varphi = \varphi_A - \varphi_B$, thus the increment of the superconducting energy is given by

$$\Delta E(\Delta\varphi) = E_J(1 - \cos\Delta\varphi) = \frac{\hbar}{2e} j_{\rm cr}(1 - \cos\Delta\varphi), \tag{2.36}$$

where $E_J$ is the bare Josephson energy. Since the Cooper pairs move from one to the other superconducting layer, the increase of electrostatic potential $\Delta E(n)$ results in

$$\Delta E(n) = \frac{Q}{2C} = \frac{(2en)^2}{2C}, \tag{2.37}$$

where $C = \epsilon/4\pi d$ is the capacitance of the single-junction, $Q = 2en$ is the charge, and $n$ is assocated with the number of the Cooper pairs $n_s$ penetrated through the junction. As a result, the Hamiltonian of this system can be written as

$$\begin{aligned} \mathcal{H} &= \frac{Q^2}{2C} + E(1 - \cos\Delta\varphi) \\ &\simeq \frac{(2e)^2 n^2}{2C} + \frac{\hbar}{2e} j_{\rm cr} \cdot \frac{\Delta\varphi^2}{2}. \end{aligned} \tag{2.38}$$

Since this Hamiltonian is equivalent to the one for a simple harmonic oscillator in which $n$ and $\Delta\varphi$ are regarded as the momentum and the coordinate, respectively. Therefore, the eigenfrequency $\omega_p$ of the system is obtained as

$$\omega_p = \frac{1}{\hbar}\sqrt{\frac{(2e)^2 E}{C}} = \sqrt{\frac{8\pi e d j_{\rm cr}}{\epsilon\hbar}} \tag{2.39}$$

$$= \frac{c}{\sqrt{\epsilon}\lambda_J} \tag{2.40}$$

with

$$\lambda_J = \sqrt{\frac{\hbar c^2}{8\pi e j_{\rm cr} d}} = \sqrt{\frac{c\phi_0}{8\pi^2 j_{\rm cr} d}}. \tag{2.41}$$

This expression corresponds to Eq. (2.35).

Using typical values of $\epsilon = 25$, $d = 15$Å, and $j_{\rm cr} = 10\,\text{emu}\cdot\text{A/cm}^2$for BSCCO, the plasma frequency is estimated to be

$$\omega_p = 2\pi\nu_p = 7.2 \times 10^{11}\,\text{rad/sec},$$
$$\nu_p \approx 100\,\text{GHz}.$$

This frequency lies in the microwave range, and the corresponding energy (0.43 meV) is well below the superconducting energy gap $2\Delta \sim 8$ meV. This result implies that the Josephson plasma mode exists in the superconducting gap. Since the damping of quasi-particles (Landau damping) should not occur in this condition, the Josephson plasma mode does not decay within the microwave time scale. This sort of plasma is also expected in the multilayer system, Lawrence and Doniach, for the first time, applied their model to calculate plasma frequency in Josephson coupling layered system [29], which is identical to Eq. (2.40).

Although the Josephson plasma phenomenon is understood by considering the simplified single Josephson junction, the following two points should be added in high temperature superconductors. The first point is that the superconducting layers are much thinner (several Å) than the the conventional Josephson junction, so that the shielding effect is incomplete. The corresponding screening length can be estimated to be $\sim$ 10 Åin high-$T_c$ superconductors. Because of this incomplete shielding effect the local Josephson relation is broken, resulting in the unusual $I-V$ characteristics as predicted by Koyama and Tachiki [49]. The second is the effect of multi-stacking of Josephson junction. This gives rise to the longitudinal charge oscillation (longitudinal plasma mode), characteristic excitation mode originated from the gauge invariance of the superconductivity. This will be discussed further in the following section.

### 2.4.3 Josephson plasma in Josephson coupled layer system

Let us consider a system in which the superconducting layers are stacked along the $z$ axis with an interval $d$ and the adjacent layers are assumed to be coupled by the Josephson effect as shown in Fig. 2.10. In order to investigate electromagnetic properties of the system, one may choose the Lawrence-Doniach model [29] as a most appropriate model for the systems, where $\xi_\perp \ll d$ must be satisfied. This condition is apparently satisfied for most high-$T_c$ superconductors, especially very anisotropic compounds such as $Bi_2Sr_2CaCu_2O_8$, used in the present study, since $\xi_\perp \sim 0.2$ Å$\ll d \sim$ 12Å. Tachiki *et al.* calculated the dispersion relations of such a layered system for longitudinal and transverse excitations —longitudinal and transverse Josephson plasma modes [46]. We will follow their procedure below.

The free energy of the Josephson coupling is given phenomenologically using the order parameter on each layer, $\Psi_\ell(\boldsymbol{r})(\boldsymbol{r} \equiv (x,y))$, in the presence of an electromagnetic field [29]

$$E = \frac{\hbar^2}{4md^2}\sum_\ell \int d\boldsymbol{r}\left|\Psi_{\ell+1}(\boldsymbol{r})\exp\left[-\frac{2ie}{\hbar c}\int_{z_\ell}^{z_{\ell+1}} dz A_z(\boldsymbol{r},z)\right] - \Psi_\ell(\boldsymbol{r})\right|^2, \tag{2.42}$$

with $z_\ell = \ell d$ and $m$ being constant with the dimension of mass. In the case that the amplitude of the order parameter $|\Psi_\ell|$ is constant; i.e. independent of $\boldsymbol{r}$ and $\ell$,

$$\Psi_\ell(\boldsymbol{r}) = \Psi_0 \exp[i\varphi_\ell(\boldsymbol{r})], \tag{2.43}$$

with $\varphi_\ell(\boldsymbol{r})$ being the phase of $\ell$ th layer, Eq. (2.42) is reduced to

$$E = \frac{\hbar^2\Psi_0^2}{2md^2}\sum_\ell \int d\boldsymbol{r}(1-\cos\varphi_{\ell+1,\ell}(\boldsymbol{r})). \tag{2.44}$$

Here $\varphi_{\ell+1,\ell}(\boldsymbol{r})$ is the gauge invariant phase difference between the $\ell$ and $\ell+1$ th layers defined as

$$\varphi_{\ell+1,\ell}(\boldsymbol{r}) = \varphi_{\ell+1}(\boldsymbol{r}) - \varphi_\ell(\boldsymbol{r}) - \frac{2\pi}{\phi_0}\int_{z_\ell}^{z_{\ell+1}} dz A_z(\boldsymbol{r},z), \tag{2.45}$$

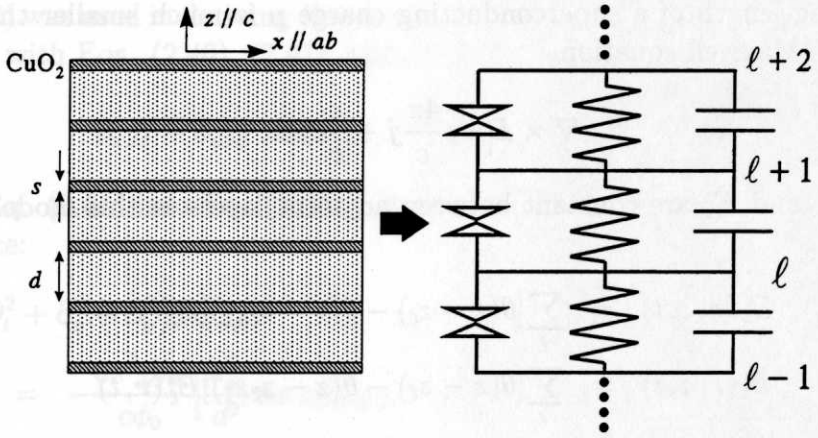


Figure 2.10: A model for strongly layered high-$T_c$ superconductors as a stack of $CuO_2$ layers (left). The equivalent circuit of this model as a 1D Josephson junction array (right). The $CuO_2$ layers are coupled with the adjacent $CuO_2$ layers through the Josephson effect. $s$ is the thickness of $CuO_2$ layers and $d$ is the distance between the layers. A condition that $s \ll d$ is different from the single junction where $s \gg d$.

where $\phi_0 = hc/2e$ is the flux quantum. In this system the current along the $z$ axis is given by the Josephson tunneling current as

$$j_z(\boldsymbol{r}, z) = -c\frac{\delta E}{\delta A_z} = j_{\rm cr}\sum_{\ell}[\theta(z - z_\ell) - \theta(z - z_{\ell+1})]\sin\varphi_{\ell+1,\ell}(\boldsymbol{r}), \tag{2.46}$$

where $\theta(z)$ is the step function and $j_{\rm cr} = 2e\hbar\Psi_0^2/md^2$. Components of the current flowing inside the layers is formed by the basis of the London theory,

$$j_\nu(\boldsymbol{r}, z) = d\sum_{\ell}\delta(z - z_\ell)j_\ell^\nu(\boldsymbol{r}) \qquad (\nu = x, y), \tag{2.47}$$

where $j_\ell^\nu(\boldsymbol{r})$ is defined by

$$j_\ell^\nu(\boldsymbol{r}) = -\frac{c}{4\pi\lambda_{ab}^2}\Big(A_\nu(\boldsymbol{r}, z_\ell) - \frac{\phi_0}{2\pi}\partial_\nu\varphi_\ell(\boldsymbol{r})\Big), \tag{2.48}$$

with $\lambda_{ab}$ being the London penetration depth of the current parallel to the $ab$ plane ($CuO_2$ layers).

We assume in the following discussion that the Eqs. (2.46) and (2.48) are also valid for the ac current. This assumption is allowed in the frequency range well below the superconducting gap at low temperatures. From the analogy of London equation Eq. (2.47), we obtain an equation of charge, which is used for complete description of an electrodynamics of a superconductor,

$$\rho(\boldsymbol{r}, z, t) = d\sum_{\ell}\delta(z - z_\ell)\rho_\ell(\boldsymbol{r}, t), \tag{2.49}$$

where

$$\rho_\ell(\boldsymbol{r}, t) = -\frac{1}{4\pi\mu}\Big(A_0(\boldsymbol{r}, z_\ell, t) + \frac{\phi_0}{2\pi c}\partial_t\varphi_\ell(\boldsymbol{r}, t)\Big). \tag{2.50}$$

Here the screening length of a superconducting charge $\mu$ is much smaller than $\lambda_{ab}$. The $z$ component of the Maxwell equation

$$\nabla \times \boldsymbol{B} = \frac{4\pi}{c}\boldsymbol{j} + \frac{\epsilon}{c}\partial_t \boldsymbol{E} \tag{2.51}$$

indicates that $B_\nu$ and $E_z$ are constant between adjacent layers in this model, so that they are expressed by

$$B_\nu(\boldsymbol{r}, z, t) = \sum_\ell [\theta(z - z_\ell) - \theta(z - z_{\ell+1})] B_\ell^\nu(\boldsymbol{r}, t), \tag{2.52}$$

$$E_z(\boldsymbol{r}, z, t) = \sum_\ell [\theta(z - z_\ell) - \theta(z - z_{\ell+1})] E_\ell^z(\boldsymbol{r}, t). \tag{2.53}$$

Thus the $z$ component of Eq. (2.51) yields the relation on each layer

$$\partial_x B_\ell^y - \partial_y B_\ell^x = \frac{4\pi j_{\rm cr}}{c} \sin\varphi_{\ell+1,\ell} + \frac{\epsilon}{c} E_\ell^z. \tag{2.54}$$

Equation for the $z$ component of magnetic field is derived from $x$ and $y$ components of Eq. (2.51), using $\nabla \times \boldsymbol{E} = -(1/c) \cdot \partial_t \boldsymbol{B}$ and Eq. (2.47) as

$$\Big[-\frac{\epsilon}{c^2}\partial_t^2 + \nabla^2\Big] B_z = \frac{d}{\lambda_{ab}^2} \sum_\ell \delta(z - z_\ell) \Big[B_z - \frac{\phi_0}{2\pi}[\partial_x, \partial_y]\varphi_\ell\Big], \tag{2.55}$$

where $[\partial_x, \partial_y]$ is a commutator as

$$[\partial_x, \partial_y]\varphi_\ell \equiv (\partial_x\partial_y - \partial_y\partial_x)\varphi_\ell = (\nabla \times \nabla\varphi_\ell)_z. \tag{2.56}$$

The formulation described above means that the $z$ component of the magnetic field (perpendicular layers) is determined independently of the $x$ and $y$ components.

Next, we remark on the equation for the gauge invariant phase $\varphi_{\ell+1,\ell}$ given in Eq. (2.45). Differentiating Eq. (2.45) with respect to $x$, $y$ and $t$, and noting Eq.(2.48), then we obtain the relations

$$\frac{\phi_0}{2\pi}\partial_x\varphi_{\ell+1,\ell} = \frac{4\pi\lambda_{ab}^2}{c}\Big[j_{\ell+1}^x - j_\ell^x\Big] + dB_\ell^y, \tag{2.57}$$

$$\frac{\phi_0}{2\pi}\partial_y\varphi_{\ell+1,\ell} = \frac{4\pi\lambda_{ab}^2}{c}\Big[j_{\ell+1}^y - j_\ell^y\Big] - dB_\ell^x, \tag{2.58}$$

$$\frac{\phi_0}{2\pi c}\partial_t\varphi_{\ell+1,\ell} = -4\pi\mu^2\Big[\rho_{\ell+1} - \rho_\ell\Big] + dE_\ell^z. \tag{2.59}$$

It is noted that Eq. (2.59) is the modified Josephson relation ($\partial_t\varphi = (2e/\hbar)V$) for the case of thin electrode and can be reduced to the conventional Josephson relation ($\partial_t\varphi = (2e/\hbar)V$) when the charging effect on the layers is neglected. From Eqs. (2.57) - (2.59) one can obtain that

$$\begin{aligned}\Big[-\frac{\epsilon}{c^2}\partial_t^2 + \partial_x^2 + \partial_y^2\Big]\varphi_{\ell+1,\ell} &= \frac{8\pi^2\lambda_{ab}^2}{c\phi_0}\Big[(\partial_x j_{\ell+1}^x + \partial_y j_{\ell+1}^y) - (\partial_x j_\ell^x + \partial_y j_\ell^y)\Big] \\ &\quad + \frac{8\pi^2 d}{c\phi_0} j_{\rm cr} \sin\varphi_{\ell+1,\ell} + \frac{8\pi^2\epsilon\mu^2}{c\phi_0}\Big[\partial_t\rho_{\ell+1} - \partial_t\rho_\ell\Big].\end{aligned} \tag{2.60}$$

Equation (2.52) was used in deriving this equation. The current conservation law, $\nabla\cdot\boldsymbol{j}+\partial_t\rho = 0$, is rewritten with Eqs. (2.46), (2.47), and (2.49) as

$$\partial_x j_\ell^x + \partial_y j_\ell^y = -\partial_t\rho_\ell - \frac{j_{\rm cr}}{d}\Big[\sin\varphi_{\ell+1,\ell} - \sin\varphi_{\ell,\ell-1}\Big]. \tag{2.61}$$

Substituting Eq. (2.61) into Eq. (2.60), we have the final equation for the gauge invariant phase difference:

$$\begin{aligned}\Big(-\frac{\epsilon}{c^2}\partial_t^2 + \partial_x^2 + \partial_y^2\Big)\varphi_{\ell+1,\ell} \\ = -\frac{8\pi^2 d j_{\rm cr}}{c\phi_0}\Big[\frac{\lambda_{ab}^2}{d^2}\sin\varphi_{\ell+2,\ell+1} - \Big(\frac{2\lambda_{ab}^2}{d^2}+1\Big)\sin\varphi_{\ell+1,\ell} + \frac{\lambda_{ab}^2}{d^2}\sin\varphi_{\ell,\ell-1}\Big] \\ - \frac{8\pi^2\epsilon\lambda_{ab}^2}{c\phi_0}\Big(1-\frac{\epsilon\mu^2}{\lambda_{ab}^2}\Big)(\partial_t\rho_{\ell+1} - \partial_t\rho_\ell).\end{aligned} \tag{2.62}$$

In the following sections, the solutions of Eq. (2.62) corresponding to the plasma oscillations are discussed.

### Longitudinal plasma mode

We assume that the phase difference between the layers is uniform in the direction parallel to the layers ($\varphi_{\ell+1,\ell}(\boldsymbol{r},t) = \varphi_{\ell+1,\ell}(t)$) in the absence of an external magnetic field in this section. In this case, Eq. (2.62) is reduced to

$$\begin{aligned}-\frac{\epsilon}{c^2}\partial_t\varphi_{\ell+1,\ell}(t) &= -\frac{1}{\lambda_c^2}\Big[\frac{\lambda_{ab}^2}{d^2}\varphi_{\ell+2,\ell+1}(t) - \Big(\frac{2\lambda_{ab}^2}{d^2}+1\Big)\varphi_{\ell+1,\ell}(t) + \frac{\lambda_{ab}^2}{d^2}\varphi_{\ell,\ell-1}(t)\Big] \\ &\quad - \frac{8\pi^2\lambda_{ab}^2}{c\phi_0}\Big(1-\frac{\epsilon\mu^2}{\lambda_{ab}^2}\Big)[\partial_t\rho_{\ell+1}(t) - \partial_t\rho_\ell(t)],\end{aligned} \tag{2.63}$$

where $\lambda_c = \sqrt{c\phi_0/8\pi^2 d j_{\rm cr}}$ denotes the penetration depth of the current flowing parallel to the $c$ axis (Josephson current). Provided this equation has plane wave solution for $\varphi_{\ell+1,\ell}(t)$ and $\rho_\ell(t) \propto \exp[ik_z\ell d - i\omega t]$, Eq. (2.63) is described in a long wavelength region ($d \ll 1/k_z$) as

$$\Big(\frac{\epsilon}{c^2}\omega^2 - \frac{1}{\lambda_c^2}[(\lambda_{ab}k_z)^2+1]\Big)\varphi(k_z) = -\frac{8\pi d\lambda_{ab}^2}{c\phi_0}\Big(1-\frac{\epsilon\mu^2}{\lambda_{ab}^2}\Big)\omega k_z\rho(k_z). \tag{2.64}$$

From the Maxwell equation $\nabla\cdot\boldsymbol{E} = 4\pi\rho$ and Eq. (2.59), we obtain another relation for $\varphi_{\ell+1,\ell}(t)$ and $\rho_\ell(t)$;

$$\rho_{\ell+1}(t) - \Big(2+\frac{d^2}{\epsilon\mu^2}\Big)\rho_\ell(t) + \rho_{\ell-1}(t) = -\frac{\phi_0}{8\pi^2 c\mu^2}[\partial_t\varphi_{\ell+1,\ell}(t) - \partial_t\varphi_{\ell,\ell-1}(t)], \tag{2.65}$$

which gives the equation in $\boldsymbol{k}$ space of

$$(\epsilon\mu^2 k_z^2 + 1)\rho(k_z) = \frac{\phi_0\epsilon}{8\pi^2 cd}\omega k_z\varphi(k_z). \tag{2.66}$$

This relation was also derived for $d \ll 1/k_z$. Combining Eqs. (2.64) and (2.66), we have a simple equation for the gauge invariant phase difference as

$$\Big[\frac{\epsilon}{c^2}\Big[1+\Big(1-\frac{\epsilon\mu^2}{\lambda_{ab}}\Big)\frac{\lambda_{ab}^2 k_z^2}{\epsilon\mu^2 k_z^2+1}\Big]\omega^2 - \frac{1}{\lambda_c^2}(\lambda_{ab}^2 k_z^2+1)\Big]\varphi(k_z) = 0, \tag{2.67}$$

therefore, the dispersion relation of the longitudinal plasma mode is described by

$$\begin{aligned}\omega_{\rm L}(k_z) &= \left[\frac{c^2}{\epsilon\lambda_c^2}\frac{(\lambda_{ab}k_z)^2+1}{1+(1-\epsilon\mu^2/\lambda_{ab}^2)(\lambda_{ab}k_z)^2/(\epsilon^2\mu^2k_z^2+1)}\right]^{1/2}, \\ &\simeq \omega_p\sqrt{1+\epsilon\mu^2k_z^2}, \end{aligned} \tag{2.68}$$

with

$$\omega_p = \frac{c}{\sqrt{\epsilon}\lambda_c}. \tag{2.69}$$

Since $\epsilon \sim 10$ and $\mu \sim 10$Åin BSCCO, this dispersion relation is almost independent of $k_z$ in the microwave frequency region ($k_z \sim 1\,\mathrm{cm}^{-1}$). This mode represents a wave with charge polarization propagating parallel to the polarization direction.

### Transverse plasma mode

When the phase difference is uniform in the direction of $c$ axis but can be spatially dependent over the plane, that is, $\varphi_{\ell+1,\ell}(\boldsymbol{r},t) = \varphi(\boldsymbol{r},t)$, we obtain the equation for the phase difference using Eq. (2.62),

$$\left[-\frac{\epsilon}{c^2}\partial_t^2 + \partial_x^2 + \partial_y^2\right]\varphi(\boldsymbol{r},t) = \frac{1}{\lambda_c^2}\sin\varphi(\boldsymbol{r},t). \tag{2.70}$$

It is noted that this equation has the same form as the one for a single junction system. Equation (2.70) is linearized and solved for small phase difference ($\sin\varphi(\boldsymbol{r},t) \simeq \varphi(\boldsymbol{r},t)$), we obtain the dispersion relation of the transverse plasma as

$$\omega_T(\boldsymbol{k}) = \omega_p\sqrt{1+\lambda_c^2k^2}, \tag{2.71}$$

with $\boldsymbol{k} = (k_x, k_y)$. Here we assume the plane wave solution propagating parallel to the layers. The transverse plasma is a composite wave of the Josephson current wave and the electromagnetic wave. The frequency dependence of the reflectivity in LSCO by Tamasaku *et al.* [36] is in good agreement with the theoretical dispersion of the transverse plasma. Assuming the $d$-pairing for superconductivity, they calculated the reflectivity for a film thickness $100\mu$m, the result is shown in Fig. 2.11. This calculated frequency spectrum of the reflectivity well explains the experimental result.

As seen in Eqs.(2.68) and (2.71), The frequency of the longitudinal plasma mode coincides with that of the transverse mode at zero wave number. However, the dispersion relations are very different: the dispersion is extremely weak compared with that of the transverse mode since $\mu^2/\lambda_c^2 \ll 1$. This is the characteristic difference of the transverse and longitudinal plasmas and they are schematically shown in Fig 2.12.

Experimentally, a uniform excitation over the layers is applied by a uniform oscillating electric field $\boldsymbol{E}_{\rm rf}$ parallel to $c$ axis, which is easily and surely obtained by using a rectangular cavity resonator described in Sec. 3.2.1 in detail. On the other hand, the transverse plasma can be generated by any excitations, which is usually uniform perpendicular to the layers but spatially variant over the layers. For example, parallel oscillating magnetic field ($\boldsymbol{H}_{\rm rf} \parallel ab$), which is employed for the transverse excitation in this study, induces spatially variant eddy currents, and the transverse plasma mode is excited inside the specimen. Although the preliminary experiment [43] had been performed without noting this point, we

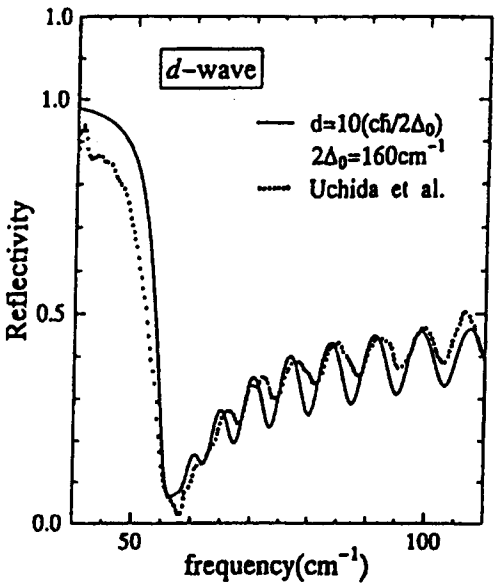


Figure 2.11: Reflectivity of film for the $d$ wave paring. The solid dots indicate the experimental data of $La_{1.85}Sr_{0.15}CuO_4$ film by Tamasaku *et al.*

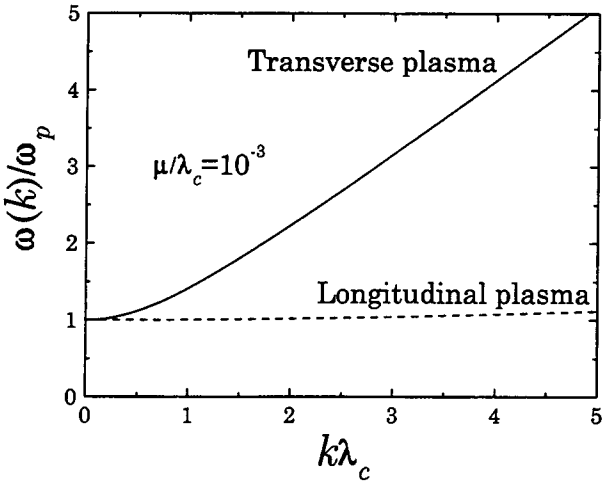


Figure 2.12: Dispersions for the plasma waves with $c$ axis polarization. The solid and dashed curves are the dispersions for the transverse and longitudinal plasma waves, respectively. The frequency $\omega$ is normalized by the plasma frequency $\omega_p = c/\sqrt{\epsilon}\lambda_c$.

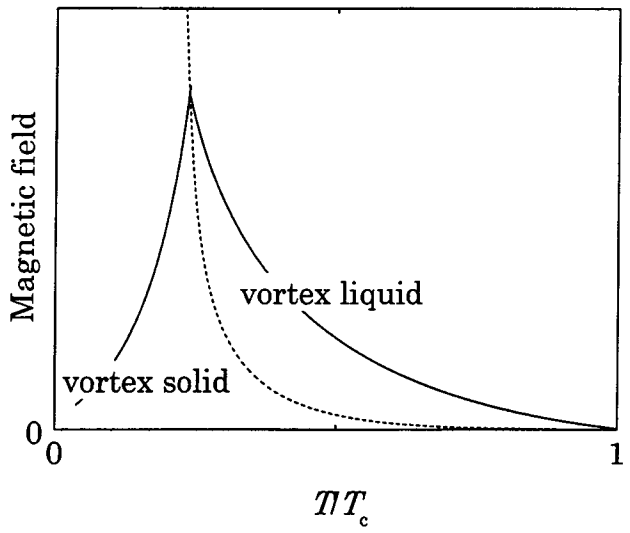


Figure 2.13: Schematic diagram of the temperature dependence of the resonance field of the Josephson plasma in the external fields parallel to the $c$ axis. The solid curve denotes the resonance field and the dashed curve denotes the boundary (formerly known as irreversibility line) which separates the vortex solid and the vortex liquid phases.

deduce that they observed the transverse plasma mode because the characteristics of the asymmetric and broad features of their observed a mixture of the transverse and the longitudinal modes because both of perpendicular and parallel oscillating magnetic field would be applied. Moreover, subsequent experiments [44] were interpreted without considering the longitudinal plasma mode despite that they might observe the longitudinal mode by using a cavity. In this study, newly resolved controversies as mentioned above by studying the Josephson plasma resonance in a cavity resonator, which gives us a clear view in the resonance mechanism. As a result, we were able to separate this two plasma modes by systematically utilizing the excitation conditions for two modes in a cavity resonator. We also emphasize that the transverse plasma mode is nothing but the Nambu-Goldstone mode in a superconductor as described above. The details are described in Chap. 4.

### 2.4.4 Interaction between plasma and vortices

Most of Josephson plasma measurement in microwave frequencies up to now are obtained by experiments with fixed microwave frequency and varying external magnetic field. Those resonance fields are strongly dependent on temperature, and have a maximum value on the phase boundary between the vortex solid (glass) and the liquid phases, when the external fields are applied parallel to the $c$ axis as schematically shown in Fig. 2.13. This fact indicates that the plasma is strongly affected by the vortices.

The effective Josephson coupling responsible for the plasma oscillation is influenced by the vortices in the following way [45]. The phase difference between the $\ell$ and $\ell+1$ th layer is divided into two parts; one is the contribution from the vortices $\varphi^v_{\ell,\ell+1}$ and another is the

contribution from the plasma $\varphi^p_{\ell,\ell+1}$:

$$\varphi_{\ell,\ell+1}(\boldsymbol{r}) = \varphi^v_{\ell,\ell+1}(\boldsymbol{r}) + \varphi^p_{\ell,\ell+1}(\boldsymbol{r}). \tag{2.72}$$

The vortex locating at $(x_{\ell,n}, y_{\ell,n})$ at $\ell$ th layer contributes to the phase $\varphi^v_{\ell,\ell+1}$ at $(x_{\ell+1,n}, y_{\ell+1,n})$ at $\ell+1$ th layer as

$$\varphi^v_{\ell,\ell+1} = \sum_n \Big[\tan^{-1}\frac{y-y_{\ell+1,n}}{x-x_{\ell+1,n}} - \tan^{-1}\frac{y-y_{\ell,n}}{x-x_{\ell,n}}\Big]. \tag{2.73}$$

The physical origin of Eq. (2.73) can be easily understood. In the $\ell$ th layer, a vortex located at $\boldsymbol{r}_{\ell,n} = (x_{\ell,n}, y_{\ell,n})$ contributes a phase $\varphi_\ell(\boldsymbol{r}_{\ell,n})$ at $\boldsymbol{r}_{\ell,n}$. The angle $\varphi_\ell$ is simply the polar angle around $\boldsymbol{r}_{\ell,n}$. Considered Eq. (2.72), the Josephson current $j_{\rm J}$ between the layers is written by

$$j_{\rm J} = j_{\rm cr}\sin\varphi_{\ell+\ell+1}(\boldsymbol{r}) \tag{2.74}$$

$$\approx j_{\rm cr}(\cos\varphi^v_{\ell,\ell+1}\cdot\varphi^p_{\ell,\ell+1} + \sin\varphi^v_{\ell,\ell+1}), \tag{2.75}$$

where $j_{\rm cr} = c\phi_0/8\pi^2\lambda_c^2 s$ is the Josephson critical current, and the higher order terms of $\varphi^p_{\ell,\ell+1}$ are neglected. If we pick up the term linear in $\varphi^p_{\ell,\ell+1}$, we have effective Josephson current as

$$j_{\rm J}^{\rm eff} = j_{\rm cr}\cos\varphi^v_{\ell,\ell+1}. \tag{2.76}$$

Equations (2.40) and (2.41) imply that the plasma frequency is proportional to $(j_{\rm J}^{\rm eff})^{1/2}$. By taking a proper space average the $c$ axis plasma frequency $\omega_c$ as a function of the external field $H$ and temperature $T$ is expressed as

$$\omega_c(H,T) = \omega_p(0,0)\langle\cos\varphi^v_{\ell,\ell+1}\rangle^{1/2}. \tag{2.77}$$

In a perpendicular field, vortices which penetrate $CuO_2$ layers (pancake vortices) are arranged along straight lines and form a triangular lattice if pinning and fluctuation are ignored. For this lattice, $\varphi^v_{\ell,\ell+1} = 0$ as follows from Eq. (2.73). In the case that the pancake vortices are not aligned but zigzag because of pinning or thermal fluctuation, $\cos\varphi^v_{\ell,\ell+1}$ is less than unity. Therefore Eq. (2.77) means that $\omega_c$ is a sensitive probe of the interlayer phase coherence $\cos\varphi^v_{\ell,\ell+1}$.

Field dependence of $\omega_c$ is phenomenologically described as

$$\omega_c^2(H) \propto H^{-\mu}, \tag{2.78}$$

where $\mu \approx 0.7 - 0.8$ in the vortex solid phase [43], and $\mu \approx 0.9 - 1$ in the vortex liquid phase [44]. This power-law of the filed dependence is theoretically controversial [50, 51], but overall features obey Eq. (2.78), so that the details of the controversy are not mentioned here. This field dependence can be explained by Eq. (2.73) qualitatively; vortices which are not aligned increases as the external field increases, thus $\cos\varphi^v_{\ell,\ell+1}$ approaches zero. The resonance occurs when $\omega_c(H)$ corresponds to the excitation (microwave) frequency with decrease of $\langle\cos\varphi^v_{\ell,\ell+1}\rangle$.

Figure 2.13 suggests that the plasma frequency in BSCCO has a maximum at a temperature on the phase boundary, and the frequency decreases as either temperature increases or decreases from the temperature. This temperature dependence of the plasma frequency may qualitatively be explained on the basis of Eq. (2.77) as follows. If one introduces point

pinning centers which are randomly distributed over the crystal, then the pancake vortices in each layer are pinned at the pinning centers at low temperatures. As a result, the phase coherence of the vortices between the layers is destroyed and $\langle \cos \varphi^v_{\ell,\ell+1} \rangle$ has a value less than unity. Therefore, the plasma frequency has a small value at low temperatures as seen from Eq. (2.77). When the temperature increases, the pinned vortices are thermally fluctuated and the phase coherence of the vortices between the layers is recovered. Due to this effect, the plasma frequency increases as temperature increases and attains a maximum on the phase boundary. When the temperature further increase, the phase coherence of the vortices are destroyed again by thermal fluctuations of the vortices and the plasma frequency decreases.

# Bibliography


[1] R. W. Wood, Phys. Rev. **44**, 353 (1933).

[2] C. Zener, Nature, **132**, 968 (1933).

[3] N. F. Mott and H. Jones, *The Theory of the Properties of Metals and Alloys,* Clarendon Press, 1936.

[4] H. Raether, *Excitation of Plasmons and Interband Transitions*, Springer, 1980.

[5] J. Daniels, C. v. Festenberg, H. Raether, and K. Zeppenfeld, "Optical constants of solids by electron spectroscopy," *Springer Tracts in Modern Physics*, edited by G. Hohler **54**, 78, Springer, 1970.

[6] Another reviews about solid state plasmas are as follows:
M. C. Steele and B. Vural, *Wave Interactions in Solid State Plasmas,* McGraw-Hill, 1969;
P. M. Platzman and P. A. Wolt, *Waves and Interactions in Solid State Plasmas,* Academic Press, 1973;
F. Forst and R. R. Gerhardts, *Metal Optics near the Plasma Frequency,* Springer, 1986.

[7] K. Onnes, Comm. Phys. Lab. Univ. Leiden, Nos. 119, 120, 122 (1911).

[8] J. Bardeen, L. N. Cooper, and J. R. Schrieffer, Phys. Rev. **106**,162 (1957); **108**, 1175 (1957).

[9] N. N. Bogoliubov, Soviet Phys. **34**, 41,51 (1958);
Bogoliubov, Tolmachev, and Shirokov, *A New Method in the Theory of Superconductivity*, Academy of Science of U.S.S.R., 1958.

[10] P. W. Anderson, Phys. Rev. **110**, 827 (1958).

[11] P. W. Anderson, Phys. Rev. **112**, 1900 (1958).

[12] G. Rickayzen, Phys. Rev. **111**, 817 (1958).

[13] M. J. Buckingam, Nuovo Cimento, **5**, 1763 (1957). J. Bardeen, Nuovo Cimento, **5**,1765 (1957). M. R. Scharfroth, Phys. Rev. **111**, 72 (1958). D. Pines and J. R. Schrieffer, Nuovo Cimento, **10**, 496 (1958).

[14] J. C. Ward, Phys. Rev. **78**, 182 (1950).

[15] Y. Takahashi, Nuovo Cimento, **6**, 370 (1957).

[16] Y. Nambu, Phys. Rev. **111**, 648 (1960).

[17] J. R. Schrieffer, *Theory of Superconductivity*, Benjamin, 1964.

[18] G. Rickayzen, *Theory of Superconductivity*, Interscience, 1965.

[19] Y. Nambu and G. Jona Lasinio, Phys. Rev. **122**, 345 (1961).

[20] J. Goldstone, Nuovo Cimento, **19**, 154 (1961).

[21] J. Goldstone, A. Salam, and S. Weinberg, Phys. Rev. **127**, 965 (1962).

[22] H. Umezawa, *Advanced Field Theory*, the American Institute of Physics Press, 1993; and references therein.

[23] P. W. Higgs, Phys. Rev. **156**, 145 (1966).

[24] T. W. B. Kibble, Phys. Rev. **155**, 1554 (1967).

[25] J. G. Bedonrz and K. A. Müller, Z. Phys. **64**, 189 (1986).

[26] V. L. Ginzburg and D. A. Kirzhnits (ed.), *High-Temperature Superconductivity*, Consultant Bureau, 1982.

[27] T. Ishiguro and K. Yamaji, *Organic Superconductors*, Springer-Verlag, 1990.

[28] J. C. Phillips, *Physics of High Temperature Superconductor*, Academic Press, 1989.

[29] W. E. Lawlence and S. Doniach, in *Proceedings of the 12th International Conference on Low Temperature Physics*, edited by E. Kanda, Academic Press of Japan, 1971.

[30] H. A. Fertig and S. Das Sarma, Phys. Rev. B **44**, 4480 (1991).

[31] S. Das Sarma and J. J. Quinn, Phys. Rev. B **25**, 7603 (1982).

[32] P. Olego, A. Pinczuk A. C. Gorssard, and W. Wegmann, Phys. Rev. B **31**, 2578 (1985).

[33] T. M. Mishonov, Phys. Rev. B **44**, 12033 (1991).

[34] D. E. Farrel, S. Bonham, J. Foster, Y. C. Chang, P. Z. Jiang, K. G. Vandervoort,D. J. Lam, and V. G. Kogan, Phys. Rev. Lett. **63**, 782 (1989).

[35] T. W. Noh, S. G. Kaplan, and A. J. Sievers, Phys. Rev. B **41**, 307 (1990).

[36] K. Tamasaku, Y. Nakamura, and S. Uchida, Phys. Rev. Lett. **69**, 1455 (1992).

[37] M. Tachiki, T. Koyama, and S. Takahashi, Phys. Rev. B **50**, 7065 (1994).

[38] R. Kleiner, F. Steinmeyer, G. Kunkel, and P. Müller, Phys. Rev. Lett. **68**, 2394 (1992).

[39] R. Kleiner and P. Müller, Phys. Rev. B **49**, 1327 (1994).

[40] G. Oya, N.Aoyama, A. Irie, S. Kishida, and H. Tokutaka, Jpn. J. Appl. Phys. **31**, L829 (1992).

[41] K. Kadowaki, T. Mochiku, Physica B **194-196**, 2239 (1994).

[42] F. X. Régi, J. Schneck, J. F. Palmier, and H. Savary, J. Appl. Phys. **76**, 4426 (1994).

[43] Ophelia K. C. Tsui, N. P. Ong, Y. Matsuda, Y. F. Yan, and J. B. Perterson, Phys. Rev. Lett. **73**, 724 (1994).

[44] Y. Matsuda, M. B. Gaifullin, K, Kumagai, K. Kadowaki, and T. Mochiku, Phys. Rev. Lett. **75**, 4512 (1995).

[45] L. N. Bulaevskii, M. P. Marley and M. Tachiki, Phys. Rev. Lett. **74**, 801 (1995)

[46] M. Tachiki, T. Koyama, and S. Takahashi, *Coherence in Superconductors*, p371, G. Deutscher (ed.), World Scientific, 1996.

[47] B. D. Josephson, Phys. Lett. **1**, 251 (1962); Adv. Phys. **14**, 419 (1965).

[48] P. W. Anderson, *"Special Effects in Superconductivity"* in *"Lectures on The Many-Body Problems, vol. 2"*, edited by E. R. Caianiello, 1964, Academic Press.

[49] T. Koyama and M. Tachiki, Phys. Rev. B **54**, 16183 (1996).

[50] L. N. Bulaevskii, V. L. Pokrovsky, and M. P. Maley, Phys. Rev. Lett. **76**, 1719 (1996).

[51] A. E. Koshlev, Phys. Rev. Lett. **77**, 3901 (1996).

# Chapter 3

# Experiment

## 3.1 Introduction

The Josephson plasma resonance (JPR) is a sort of electromagnetic absorptive phenomena which was discovered in the course of surface impedance measurements in $Bi_2Sr_2CaCu_2O_8$ by Tsui *et al.* [1] in 1994. Their experimental configuration was as follows.

- The external field was applied parallel to the $c$ axis.
- Incident electromagnetic wave frequencies were in a microwave range between 30 and 50 GHz.
- The specimen was set in the rectangular waveguide with $TE_{10}$ mode so that the $c$ axis is parallel to the microwave $\boldsymbol{k}$ vector.
- The absorption was detected by the bolometric method, which mainly consists of a sapphire sample stage and a bolometer (a tiny carbon resistor or a temperature sensor).

The sample was supported by the sample stage, which was thermally isolated and fixed on the waveguide flange in which the choke pattern was cut. The amplitude of incident microwave was modulated at a frequency of several hertz. This method is simple and sensitive enough for this purpose of surface impedance measurement, however, has disadvantages in the following two points.

First, it is uncertain what type of oscillating electromagnetic field ($\boldsymbol{E}_{\rm rf}$ and $\boldsymbol{H}_{\rm rf}$) is exciting the resonance. Considering the oscillating electromagnetic field distribution inside the $TE_{10}$ rectangular waveguide, there are equal possibility for $\boldsymbol{E}_{\rm rf}$ and $\boldsymbol{H}_{\rm rf}$ that can generate plasma waves by applying parallel to the $CuO_2$ plane of the sample. See Fig. 3.1. Therefore current parallel to both $c$ axis and $ab$ plane can be induced, and we cannot distinguish which current drives the observed resonance. In order to make this clear it is necessary to use a cavity resonator, in which $\boldsymbol{E}_{\rm rf}$ and$\boldsymbol{H}_{\rm rf}$ can be selected without ambiguity. By this reason, subsequent experiments have been employed in a rectangular cavity resonator with $TE_{102}$ mode [2, 3] or a cylindrical cavity resonator with $TM_{011}$ and $TE_{011}$ modes [4, 5]. Although the rectangular cavities have less quality factor $Q$ value, they have a unique modes for their dimensions without degeneracy. On the other hand, cylindrical cavities have higher $Q$ value of $\sim 10^3 - 10^4$, but different modes with similar resonant frequencies can exist in the same cavity. This is sometimes inconvenient to separate plasma modes excited by either $\boldsymbol{E}_{\rm rf}$ or $\boldsymbol{H}_{\rm rf}$.

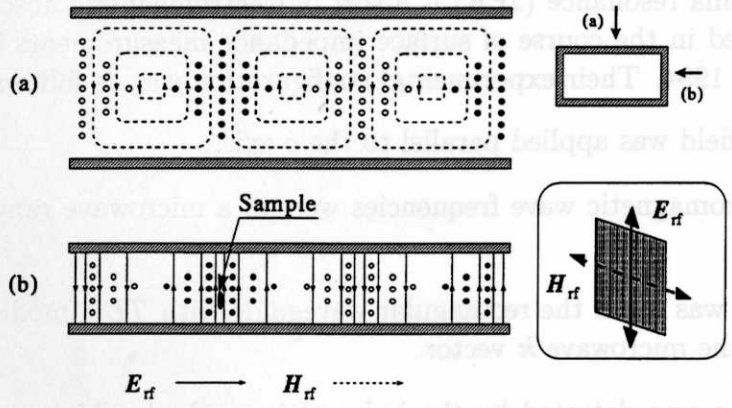


Figure 3.1: High frequency electromagnetic field distribution of rectangular waveguide with $TE_{10}$ mode and configuration of the experiment by Tsui *et al.* The solid symbol denotes a vector directed up out of the paper and the opened one into the paper. Dotted lines refer to $\boldsymbol{H}_{\rm rf}$ and Solid lines to $\boldsymbol{E}_{\rm rf}$. Inset shows the RF electromagnetic field close to the specimen in the previous experiment. (a) and (b) are the views from $E$ (wider) and $H$(narrower) planes of waveguide, respectively.

Second, the bolometric technique can detect only thermal absorption of the incident microwave dissipated in the specimen. This technique was developed to measure surface impedance of superconductors in finite external field [6], and it has high sensitivity: 1 nW absorption against 10 mW irradiation at several tens GHz microwave at 4.2 K. On the contrary, the microwave bridge method, which has been employed for conventional surface impedance, electron spin resonance (ESR) and cyclotron resonance (CR) observation, is not so sensitive as the bolometric technique. However, it has an advantage to extract the phase information of the electromagnetic response function of the specimen. The details are mentioned later. Therefore, the microwave bridge method with a rectangular cavity resonator was employed in this study.

In this chapter, the system and the principle of the Josephson plasma resonance measurements used in this study are introduced including superconducting magnets, variable temperature cryostat and so on. The method of sample preparation is also described.

## 3.2 Josephson plasma resonance measurement

All experiments described in Chap. 4 and a part of in Chap. 5 were performed at National Research Institute for Metals (NRIM), Tsukuba, and the rest of the experiments were done at Institute of Materials Science, University of Tsukuba. The measurement systems used in both laboratories are almost same, which consist of a microwave bridge, a sprit pair superconducting magnet with a cryogenic variable temperature cryostat, and a high precision goniometer. The block diagram is shown in Fig. 3.2.

### 3.2.1 Microwave bridge

The microwave bridge balance system used in this study is a refection type of bridge which consists of a cavity, a krystron, and the other components as shown in Fig. 3.2. This reflection type of bridge is one of bridge balance circuits. This is the heart of this experiments and detects signals as off-balanced signal between the sample loaded (cavity) arm and the reference (termination) arm. The operating principle of this balancing circuit is as follows. Microwaves generated by the krystron is fed into the magic tee and the microwaves split into two: one propagates to the cavity arm, and other to the termination arm. The microwave travels to the cavity arm and reflected back making standing wave in the whole waveguide. If the microwave frequency matches the resonant frequency, the cavity can resonates and stores microwave energy, up to an energy corresponding to the $Q$ value. If the resonance occurs inside the cavity, the reflected waves become weak because of the change of the cavity impedance corresponding to the electromagnetic response of the sample. Since the reflected microwave was balanced perfectly so as to make zero microwave at the detector from the magic tee off resonance, the reduction of the reflected microwave gives rise to an unbalanced signal as the magic tee, which can be detected by the detector.

In the following, we describe the principle of operation by parts used in this study.

#### Resonant cavity

The microwave cavity used in this study is shown in Fig. 3.3. This cavity consists of two pieces of copper rectangular waveguide of 35 GHz band (WRI-320 in JIS; inside dimension is 7.11mm×3.56mm), a bottom plate and a coupling iris, all parts are made by the author. The

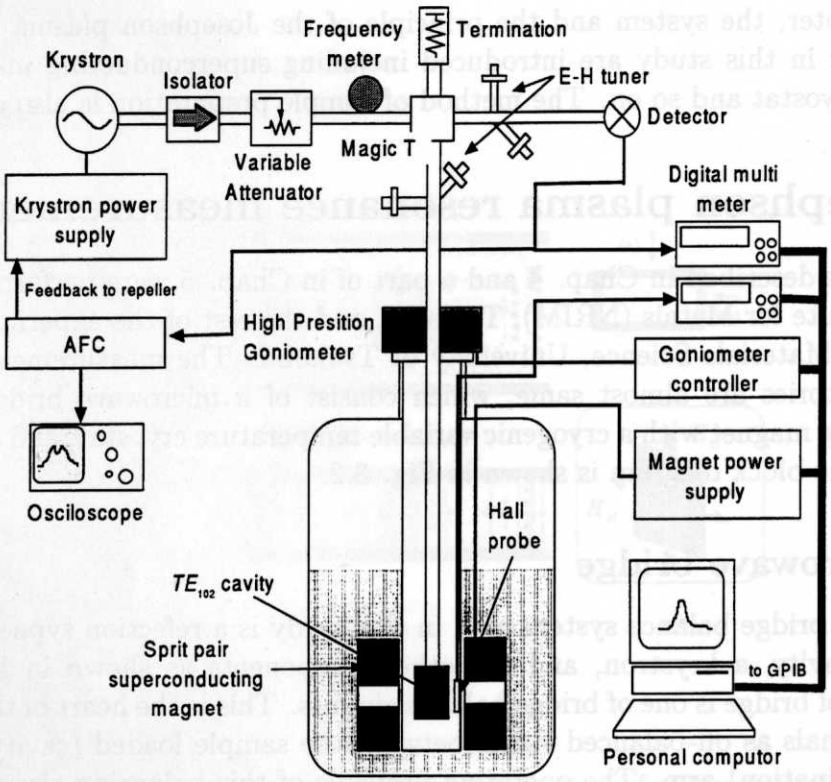


Figure 3.2: Block diagram of the measuring system used in this study. The incident microwave frequency is stabilized by the AFC (automatic frequency controller) and the absorption is detected by Shottky barrier diode. The superconducting magnet can generate horizontal magnetic field. The personal computer controls some devices, displays and stores acquired data. The cryogenic system is omitted.

bottom part of the cavity can be detached to insert a specimen at the height of $\lambda_g/4 = 2.7$ mm from the bottom, where $\lambda_g$ is the guide wavelength of 35GHz microwave. This construction is considered to keep highest $Q$ value. The cavity has unloaded resonant frequency of 35.1 GHz in $TE_{102}$ mode, which is the most fundamental mode of a cavity resonator. Specimens were placed at the position(a), where $\boldsymbol{E}_{\rm rf}$ is maximum and $\boldsymbol{H}_{\rm rf}$ is minimum, or (b), vice versa. When the specimen was placed at (a), a sample stage which is cut from a piece of Teflon® was used.

**Detection of absorption** A resonant cavity is the microwave analogue of an rf-tuned circuit as shown in Fig. 3.4, which has a characteristic resonance frequency $\omega_0 = 1/\sqrt{LC}$, where the impedance $Z$

$$Z = \frac{R + i\omega L}{1 - \omega^2 LC + i\omega CR} \tag{3.1}$$

becomes minimum. The quality factor $Q$, measure of the sharpness of the resonance of the cavity itself, is defined by

$$Q = \frac{\omega_0 L}{R} = \frac{1}{R\omega_0 C} \tag{3.2}$$

$$= \frac{2\pi(\text{energy stored})}{\text{energy dissipated par cycle}}. \tag{3.3}$$

This $Q$ factor plays a very important role in the theory of resonant cavities.

In practical cavities, the overall or loaded $Q$ may be a sum of the reciprocals of the $Q_u$ due to the ohmic losses in the walls of the cavities, the $Q_r$ due to the cavity coupling holes, and the $Q_m$ due to materials in the cavities, and in the following form

$$\frac{1}{Q} = \frac{1}{Q_u} + \frac{1}{Q_r} + \frac{1}{Q_m}. \tag{3.4}$$

Here $1/Q_m$ consists of the magnetic, the conductive and the dielectric losses, and the observations for their resonating variations coincide with ESR, CR and JPR measurements, respectively.

When a substance which has a nonlinear dielectric complex function $\epsilon = \epsilon' - i\epsilon''$ is placed inside the resonant cavity of frequency $\omega_0 = 2\pi\nu_0$, the dielectric contribution of the average power absorption par unit volume is given by

$$\wp = \frac{1}{2}\omega_0 E_{\rm rf}^2 \epsilon'', \tag{3.5}$$

where $E_{\rm rf}$ is the amplitude of the microwave electric field at the sample. The power absorption at resonance will manifest itself as a change in $Q$ of the cavity,

$$\frac{1}{Q} = \frac{1}{Q_0} + \frac{1}{Q_\epsilon}, \tag{3.6}$$

where $Q_0$ is the $Q$ of the cavity in the absence of resonant absorption and $Q_\epsilon$ is the contribution of the resonant absorption to the $Q$. This quantity $Q_0$ includes cavity losses plus the magnetic and conductive losses in the sample. At resonance, the $Q$ changes by an amount $\Delta Q$:

$$\Delta Q = -Q^2 \Delta\left(\frac{1}{Q}\right) = -\frac{Q_0^2}{Q_\epsilon}, \tag{3.7}$$

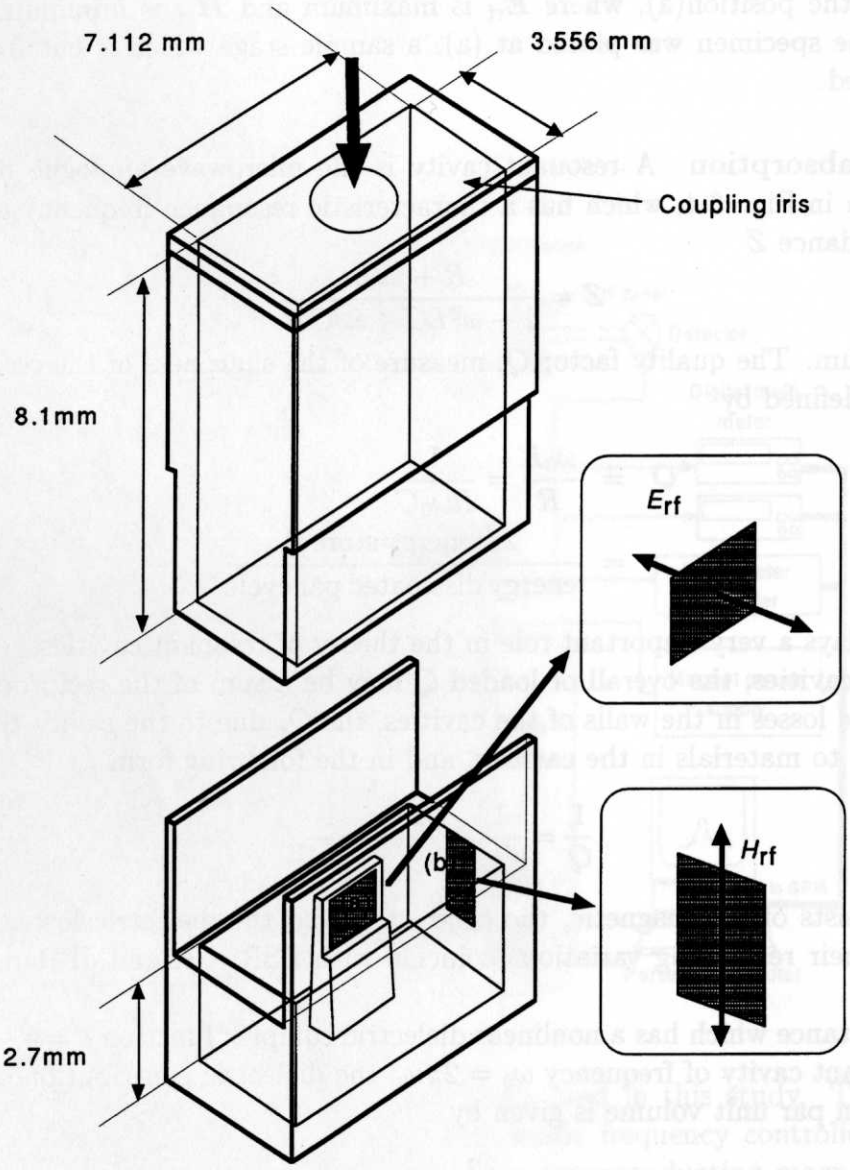


Figure 3.3: Schematic view of the cavity resonator and the position of the sample. The cavity is made of copper waveguide of WRI-320 (JIS; WR-28 in EIA), whose inner cross section is a rectangle of 7.11 mm × 3.56 mm. The resonance frequency of the cavity is 35.1 GHz without load. The samples can be placed at two positions where (a) $\boldsymbol{E}_{\rm rf}$ or (b) $\boldsymbol{H}_{\rm rf}$ is maximum. The insets show the geometrical relation between the sample and microwave $\boldsymbol{E}$ and $\boldsymbol{H}$ vectors The solid and thick arrow denotes incident microwave.

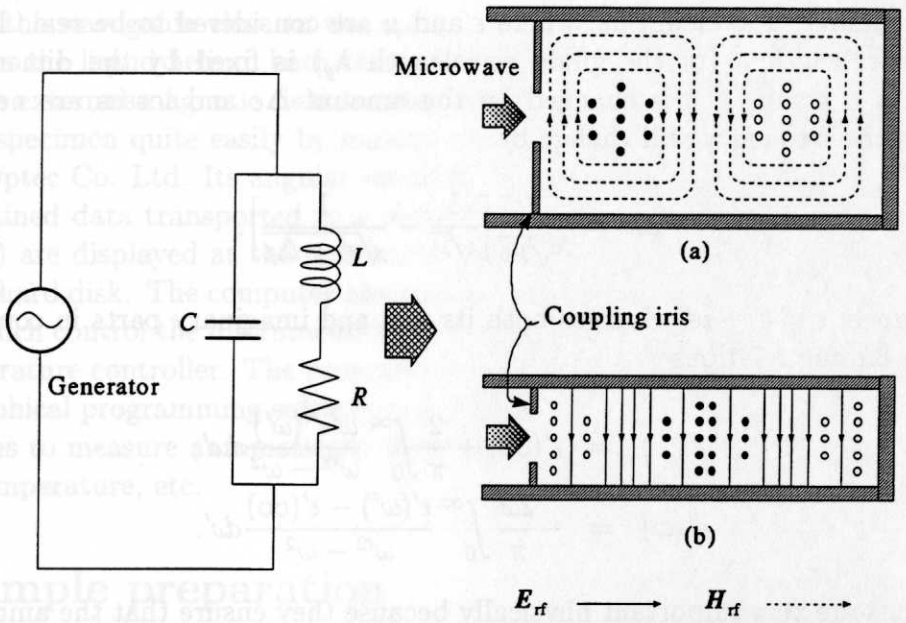


Figure 3.4: A microwave cavity and LCR equivalent circuit. Right panel shows a cavity with $TE_{102}$ mode, which is employed in this study. The notation follows Fig. 3.1.

where we assume $Q_\epsilon \gg Q_0$ and $1/Q_\epsilon$ off resonance is neglected. As defined by Eq. (3.3), $Q_\epsilon$ has the form

$$Q_\epsilon = \frac{(1/2)\int_{\text{cavity}} E_{\text{rf}}^2 dV}{(1/2)\int_{\text{sample}} E_{\text{rf}}^2 \epsilon'' dV}. \tag{3.8}$$

If $\epsilon''$ is homogeneous over the sample volume, then one has

$$Q_\epsilon = \frac{\int_{\text{cavity}} E_{\text{rf}}^2 dV}{\epsilon'' \int_{\text{sample}} E_{\text{rf}}^2 dV} = \frac{1}{\epsilon'' \eta}, \tag{3.9}$$

where $\eta$ is the filling factor. The filling factor is a measure of the fraction of the microwave energy that interacts the sample, and explicit values of $\eta$ are given in Sec. 5-H of Ref. [7] for commonly used sample arrangements. Equations (3.7) and (3.9) furnish the change in $Q$:

$$\Delta Q = \epsilon'' \eta Q_0^2, \tag{3.10}$$

where the negative sign is omitted for simplicity.

**Detection of dispersion** In the preceding paragraphs the change in $Q$ that results from the behavior of the absorption or the imaginary part of the dielectric function $\epsilon''$ at resonance has been discussed. During resonance there will also be a dispersion mode that corresponds to a change in the frequency of the resonant cavity as a result of the real part of the dielectric function $\epsilon'$. The reason for this frequency change may be deduced by considering the velocity $v$ of electromagnetic radiation in a dielectric medium

$$v = \frac{1}{\sqrt{\mu_0 \epsilon}} = \nu\lambda, \tag{3.11}$$

with a permeability in a vacum $\mu_0$, where $\epsilon$ and $\mu$ are considered to be real. In a resonant cavity the wavelength $\lambda$ (or the guide wavelength $\lambda_g$) is fixed by the dimensions of the resonator. As a result, if $\epsilon$ is changed by the amount $\Delta\epsilon$ and losses are neglected (i.e., $\epsilon'' = 0$), then the frequency will change by

$$\Delta\nu = \frac{1}{\lambda\sqrt{\mu_0}}\left[\frac{1}{\sqrt{\epsilon'}} - \frac{1}{\sqrt{\epsilon' + \Delta\epsilon}}\right]. \tag{3.12}$$

At resonance, $\epsilon = \epsilon' + i\epsilon''$ changes both its real and imaginary parts in conformity with the Kramers-Kronig relations

$$\epsilon'(\omega) = \epsilon'(\infty) + \frac{2}{\pi}\int_0^\infty \frac{\omega'\epsilon''(\omega')}{\omega'^2 - \omega^2}d\omega', \tag{3.13}$$

$$\epsilon''(\omega) = -\frac{2\omega}{\pi}\int_0^\infty \frac{\epsilon'(\omega') - \epsilon'(\infty)}{\omega'^2 - \omega^2}d\omega'. \tag{3.14}$$

These relations are very important physically because they ensure that the amplitude of the observed signal from $\epsilon'$ will be comparable to that observed from $\epsilon''$.

In this study, the klystron is stabilized on the sample resonant cavity by an automatic frequency-controller (AFC), so that it will "follow" the frequency variations, and the dispersion mode will be stabilized out. If a homodyne or balanced mixer detection is employed to vary the effect of line in front of the resonant cavity easily and effectively, then the dispersion mode can be observed and the phase information of the resonance is extracted from it.

#### Krystron, detector, and the other microwave components

A reflecting type of krystron 36V12 fabricated by Okaya Electronic Industries Co. Ltd. was employed as a microwave generator. It can output high-power microwave of 600mW at maximum, in the frequency range from 33 to 38 GHz. In the practical experiments, we have to choose a stable mode, whose output power may be less than half of the maximum. Moreover, the radiated microwave is attenuated by waveguides, the variable attenuator, and the other components, so that the incident power into the cavity may be roughly estimated at several tens mW without calibration.

A semiconductor detector (Model WDP-22, Farran Technology Ltd.) was used for microwave detection. The detector mounts zero biased Schottky barrier diodes, and has minimum sensitivity of 750 mV/mW in the range of 33-50 GHz.

The other components constructing the bridge circuit such as an isolator and an attenuator are not explained in detail because of simple functions of them [7].

### 3.2.2 Magnet, cryogenic system and goniometer

Two superconducting magnet systems with variable temperature inserts are used throughout this study, one is installed at NRIM and other is installed at University of Tsukuba. Both of the magnets are driven by magnet power supplies (Model 622, LakeShore Co. Ltd.) and produces horizontal magnetic filed, the maximum fields are 6 and 8 Tesla for the former and the latter, respectively.

The temperature of the sample is monitored by a Cernox® temperature sensor which placed just above the cavity and is controlled by a PID temperature controller with a heater

wounded to the waveguide close to the cavity. Cooling of the system was made by flowing cold gas from the liquid helium bath through the needle valve.

Since the external magnetic field is horizontal, we can change the direction of the field against the specimen quite easily by making use of one-axis high-precision goniometer fabricated by Optec Co. Ltd. Its angular resolution is designed as fines as $4.0\times10^{-5}$ degree.

The obtained data transported to a personal computer via GPIB (General Purpose Interface Bass) are displayed at the monitor of the computer with Microsoft Windows® and stored in its hard disk. The computer also carries out the measurement sequences by original programs which control the instruments such as digital multimeters, a magnet power supply, and a temperature controller. The programs were designed by the author with LabVIEW®, which is graphical programming software copyrighted by National Instruments Cooperation, and enable us to measure automatically with varying several parameters; the external field direction, temperature, etc.

## 3.3 Sample preparation

Single crystals of $Bi_2Sr_2CaCu_2O_{8+\delta}$ (crystal structure is shown in Fig. 2.7) used in this study have been grown by means of the traveling solvent floating zone (TSFZ) technique [8]. This technique has advantages in comparison with other techniques such as top seeded solution growth and flux-method, which are often used for the single crystal growth of oxides. The reason this is that the TSFZ method can overcome a problem of uncontrollable doping process of cationic elements as well as oxygen, which is essential for high-$T_c$ superconductivity. By the same token, the Czochralski method is very difficult to obtain high quality single crystals. The single crystals were grown in air with the growth rate of 0.5–1 mm/h using an infrared convergence type of floating zone furnace [9]. The as-grown boule can be easily cleaved into thin slabs of single crystals with *ab* plane and the slabs are cut by sharp knives and further cleaved by adhesive tape into proper sizes.

Several samples with columnar defects used in Chap. 5 are irradiated with heavy ions such as $I^{28+}$ and $Xe^{31+}$ generated by a tandem Van de Graaff accelerator, which is installed at Japan Atomic Research Institute (JAERI), Tokai. The density of defects is determined by exposed time and calibrated by a detector located behind the specimen.

# Bibliography


[1] Ophelia K. C. Tsui, N. P. Ong, Y. Matsuda, Y. F. Yan, and J. B. Perterson, Phys. Rev. Lett. **73**, 724 (1994).

[2] Y. Matsuda, M. B. Gaifullin, K, Kumagai, K. Kadowaki, and T. Mochiku, Phys. Rev. Lett. **75**, 4512 (1995).

[3] K. Kadowaki, M. B. Gaifullin, Y. Matsuda, K. Kumagai, S. Takahashi and M. Tachiki, Czechoslovak J. Phys. **46**, Suppl. S3 1625 (1996).

[4] S. Sakamoto, A. Maeda, T. Hanaguri, Y. Kotaka, J. Shimoyama, K. Kishio, Y. Matsushita, M. Hasegawa, H. Takei, H. Ikeda and R. Yoshizaki, Phys. Rev. **B 53**, R14749 (1996).

[5] T. Shibauchi, M. Sato, A. Mashio, T. Tamegai, H. Mori, S. Tajima and S. Tanaka, Phys. Rev. **B 55**, 11977 (1997).

[6] Y. Matsuda, N. P. Ong, Y. F. Yan, J. Harris, and J. B. Perterson, Phys. Rev. B **49**, 4380 (1994).

[7] Charles P. Poole. Jr., "*Electron Spin Resonance, A Comprehensive Treatise on Experimental Techniques*", 2 nd edition, John Wiley & Sons, 1983 and references therein.

[8] M. J. V. Menken, A. J. M. Winkelmen and A. A. Menovsky, J. Crystal Growth **133**, 9 (1991);
M. J. V. Menken, Ph. D. Thesis, University of Amsterdam, 1991.

[9] T. Mochiku and K. Kadowaki, Physica C **235-240**, 523 (1994).

# Chapter 4

# Mode separation of the Josephson plasma

[1]

## 4.1 Introduction

The electromagnetic resonance due to the plasma oscillation in a microwave frequency region was discovered by Tsui *et al.* [1]. in the surface impedance measurement of the *ab* plane of $Bi_2Sr_2CaCu_2O_{8+\delta}$ in a perpendicular external field ($\boldsymbol{H}_{\rm ext}\|c$). Subsequently, Matsuda *et al.* [2] observed a sharp resonance by the experiments in a perpendicular oscillating electric field ($\boldsymbol{E}_{\rm rf}\|c$) with a cavity resonator. They interpreted that this resonance is due to the Josephson plasma resonance as suggested by Bulaevskii *et al.* [3]. In those studies, it is also shown that the absorption line intensity, the width, and the position behave in a complicated fashion as functions of the external field $\boldsymbol{H}_{\rm ext}$, the microwave frequency $\nu$, and the temperature $T$, suggesting the existence of a strong coupling between the plasma modes and the vortex state. Since then, several theoretical [4, 5, 6] and similar experimental [7] works on the Josephson plasma phenomena in $Bi_2Sr_2CaCu_2O_{8+\delta}$ have been reported. Similar absorption phenomena have also been observed in $Bi_2(Sr,La)_2CaCu_2O_y$ [8], and in an organic superconductor $\kappa$-(BEDT-TTF)$_2$Cu(NCS)$_2$ [9]. These materials are also well known as layered superconductors which have arrays of SIS Josephson junctions similar to $Bi_2Sr_2CaCu_2O_{8+\delta}$.

A fundamental question has arisen from the recent theoretical studies. Since there exist two plasma modes, longitudinal and transverse, as collective excitations, the question is which mode has been observed experimentally. According to the theory, the two modes have very different dispersion relations: the longitudinal plasma mode ($\boldsymbol{k}\|c$) has a characteristic flat dispersion, whereas the transverse one ($\boldsymbol{k}\perp c$) shows a strong dispersion which tends to a linear dependence for $k \to \infty$ [10]. As a result, the line shapes of the resonances are expected to differ considerably: for the longitudinal mode, it should be sharp and almost symmetric, while the resonance of the transverse mode has a broad and asymmetric line shape because of the long tail on the higher field side of the resonance. In order to examine the character of the two modes, experiments have been performed with various configurations of sample position and microwave fields, $\boldsymbol{E}_{\rm rf}$ and $\boldsymbol{H}_{\rm rf}$. From these experiments, it is concluded that

[1] A large part of this chapter has been already published as I. Kakeya *et al.*, Phys. Rev. B **57**, 3108 (1998).

the resonance observed in the case of $\boldsymbol{E}_{\rm rf}||c$ is not the transverse plasma mode but the longitudinal one [11]. This conclusion contradicts earlier ones, [2, 3] which identified it as the transverse mode.

In this chapter, we discuss in detail how to distinguish the two modes experimentally by using two configurations of plasma excitations were found to be important among several possible configurations of microwave $\boldsymbol{E}_{\rm rf}$ and $\boldsymbol{H}_{\rm rf}$ vectors and the crystallographic axes of the sample: one is the case $\boldsymbol{E}_{\rm rf}||c$ and the other is the case $\boldsymbol{H}_{\rm rf}||ab$. Two plasma modes can be generated separately and independently by these two experimental conditions. The distinction of the two modes is done by making use of the sample size dependence of the plasma resonance: for the transverse mode excited in the configuration of $\boldsymbol{H}_{\rm rf}||ab$, a systematic shift of the resonance field was observed as a function of the sample size $L$ in the $ab$ plane, while for the longitudinal mode, it is independent of $L$ according to the theoretical prediction [12]. This sharp difference of the sample size effect is expected from the characteristic dispersion relation of the transverse mode.

This clear experimental evidence for two distinct plasma modes leads to an interesting corollary concerning a fundamental aspect of the superconducting phase transition. As is well known in the theory of phase transitions with the spontaneous symmetry breaking, the phase symmetry of the gauge field is spontaneously broken with the appearance of the superconducting phase. The collective excitations associated with the broken phase symmetry in a superconductor are known to be the longitudinal plasma mode, which is the Nambu-Goldstone mode [13, 14, 15, 16]. Therefore, the distinction of the two plasma modes made in the present experiments gives direct experimental confirmation of the existence of the Nambu-Goldstone mode in a superconductor [17]. The plasma mode in a charged system such as conventional superconductors has an energy gap of the order of eV. Thus, as pointed out by Anderson, the Nambu-Goldstone mode has never been observed experimentally in the past. Furthermore, the observed energy gap of the plasma mode proves directly the validity of the Anderson-Higgs-Kibble [18, 19, 20] mechanism for superconducting phase transition.

## 4.2 Experimental details

All experiments were performed at 35 GHz. A rectangular cavity resonator with $TE_{102}$ mode was used as described in Sec. 3.2.1. The measurements were performed for two samples. Superconducting transition temperatures are 90 and 84 K for sample A and B, respectively. This was checked after all measurements were done by magnetic-susceptibility measurements in a superconducting quantum interference device (SQUID) magnetometer. Both samples are rectangular thin plates with thickness about 20 $\mu$m. Sample A was carefully cut in several steps using a sharp knife from the initial size of 2.8 mm $\times$ 2.5 mm to final size of 0.73 mm $\times$ 0.72 mm. At each step, resonance experiments with varying temperature were carried out for different configurations of the sample (both $\boldsymbol{E}_{\rm rf}||c$ and $\boldsymbol{H}_{\rm rf}||ab$). The sample was placed at two positions in order to have the two different configurations shown in Fig. 3.3. In the first case, the sample is placed at the position where $\boldsymbol{E}_{\rm rf}$ is maximum and $\boldsymbol{E}_{\rm rf}$ and $\boldsymbol{H}_{\rm ext}$ are parallel to the $c$axis on the sample stage made of Teflon (position(a)). This configuration is same as in previous experiments [2, 11]. In the second case, the samples are glued on the $H$ plane of the cavity with grease so that $\boldsymbol{H}_{\rm rf}$ and $\boldsymbol{H}_{\rm ext}$ are parallel and perpendicular to the $ab$ plane, respectively (position (b)).

## 4.3 Experimental results

### 4.3.1 Resonance absorption in a perpendicular oscillating electric field

For both samples, a sharp plasma resonance is observed. As an example, typical resonance lines of sample A are shown in Fig. 4.1, where the absorption is shown as a function of $\boldsymbol{H}_{\text{ext}}$, applied parallel to the $c$ axis, for various temperatures below $T_c$. The resonance line begins to appear just below $T_c$ near zero field and the resonance field shifts to higher field as temperature is decreased. The resonance field shows a maximum around 25 K and decreases again as temperature is decreased. At temperatures lower than 25 K, the resonance line tends to show considerable hysteresis with field increase and decrease. It is noted that the hysteretic resonance line below 25 K shows relaxation behavior, indicating that the nonequilibrium magnetic properties are involved in this phenomenon. This hysteretic behavior is clearly seen in the data at 15 and 20 K in Fig. 4.1.

Another feature seen in Fig. 4.1 is that the resonance line shape is almost symmetric with a slight tail on the higher field side. This behavior contrasts with that for the case of $\boldsymbol{H}_{\text{rf}} \| ab$ as described below. All these behaviors are very similar to the previous results obtained in the same condition [2, 11]. When the sample dimension in the $ab$ plane is reduced, the position of resonance line does not move in this configuration ($\boldsymbol{E}_{\text{rf}} \| c$). This experiment was carried out on sample B whose dimension in the $ab$ plane was varied from 1.8 to 0.79 mm, the lines are shown in Fig. 4.2.

### 4.3.2 Resonance absorption in a parallel oscillating magnetic field

Resonance absorption at various temperatures below $T_c$=90 K is shown in Fig. 4.3 at 35 GHz with $\boldsymbol{H}_{\text{rf}} \| ab$ (see the inset of Fig. 4.3). The same sample as the one used for $\boldsymbol{E}_{\text{rf}}$ is used in this measurement by changing the sample position inside the cavity after each cutting for the case of sample B. The spikelike lines at 12.48 kOe are due to the ESR signal of DPPH (1,1-dyphenil-2-picryl hydragyl) as a field marker. The sample was a rectangular shape, 1.46 mm $\times$ 2.40 mm $\times 28\,\mu$m, in this particular case. In this case, two distinct peaks with different characters were observed: the resonance at the lower field is sharper and relatively weaker, while the one at a higher field is broader and stronger in absorption intensity. These characteristic features of the two lines for $\boldsymbol{H}_{\text{rf}} \| ab$ are in sharp contrast with the one in the case for $\boldsymbol{E}_{\text{rf}} \| c$, where only a single line is observed regardless of the sample dimension $L$. The number of lines are determined as a function of the sample dimension for $\boldsymbol{H}_{\text{rf}} \| ab$. In the case of larger sample dimension $L$, we observed multiabsorption lines (more than two). We have chosen the sample to be as large as possible for this experiment but it is restricted by the dimension of the cavity and the field homogeneity inside the cavity as seen in Fig. 3.3.

When the temperature is varied from 4.2 K, both resonance lines shift toward higher fields up to about 25 K, then turn to decrease to lower fields drastically. Below 25 K, the resonance curve shows the hysteretic behavior as seen in Fig. 4.3. It seems experimentally that such a temperature dependence of the resonance lines is common for both cases in $\boldsymbol{H}_{\text{rf}} \| ab$ and in $\boldsymbol{E}_{\text{rf}} \| c$. This behavior, in particular, for the case of $\boldsymbol{H}_{\text{rf}} \| ab$ is plotted in Fig. 4.4, where the sharp maximum of the resonance field as a function of temperature can be seen. These maximum positions reproduce very well the irreversibility line as pointed out

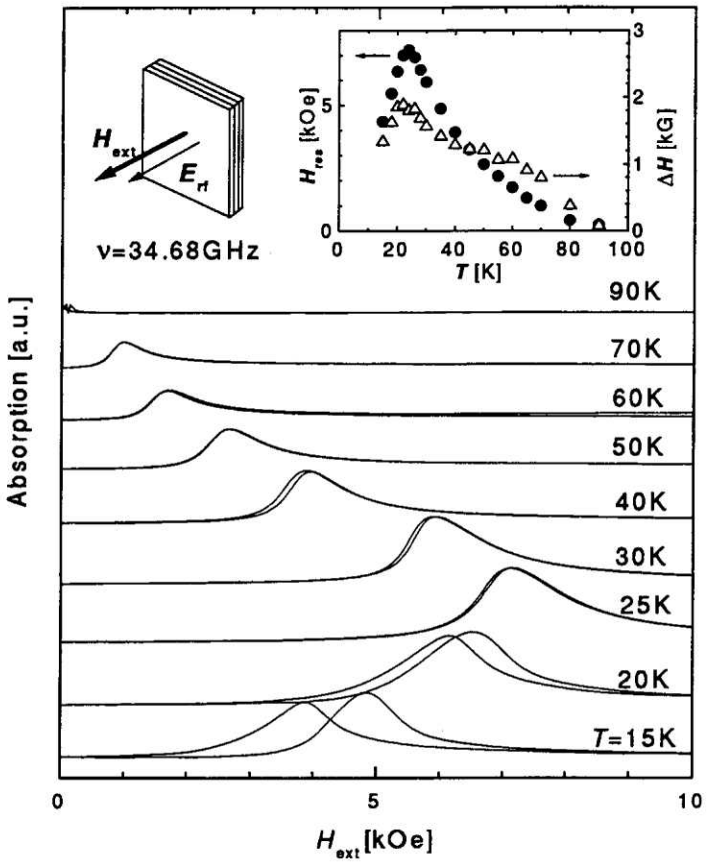


Figure 4.1: Temperature dependence of the resonance line of sample A in the configuration of $\boldsymbol{E}_{\rm rf} \| \boldsymbol{H}_{\rm ext} \| c$. The incident microwave frequency is 34.68 GHz. The shape of the resonance line is almost symmetric and has a only slight tail at a higher field side, which is the characteristic feature of the longitudinal plasma mode. The resonance field is maximum around 25 K and decreases as temperature increases approximately in proportion to $1/T$. The inset shows the plotted results of the resonance field (solid circles) and the linewidth (open triangles) as a function of temperature.

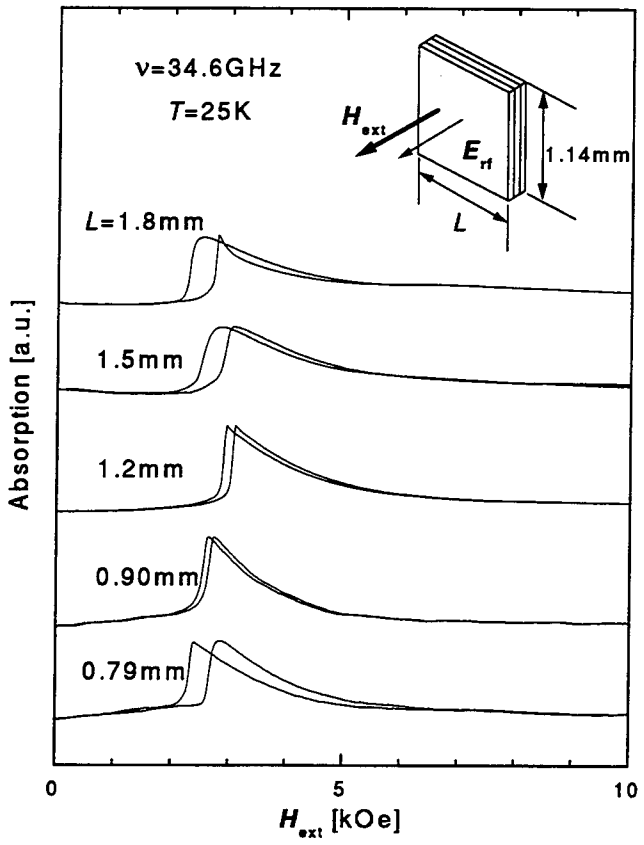


Figure 4.2: The resonance lines of sample B for various size of *ab* plane when the oscillating electric field is applied perpendicular to *ab* plane. The resonance peaks do not move despite the size being changed. One side of the rectangular specimen is varied by cutting with knife, and other side is kept constant of 1.14 mm. Asymmetric and hysteretic shape of the resonance is due to power saturation.

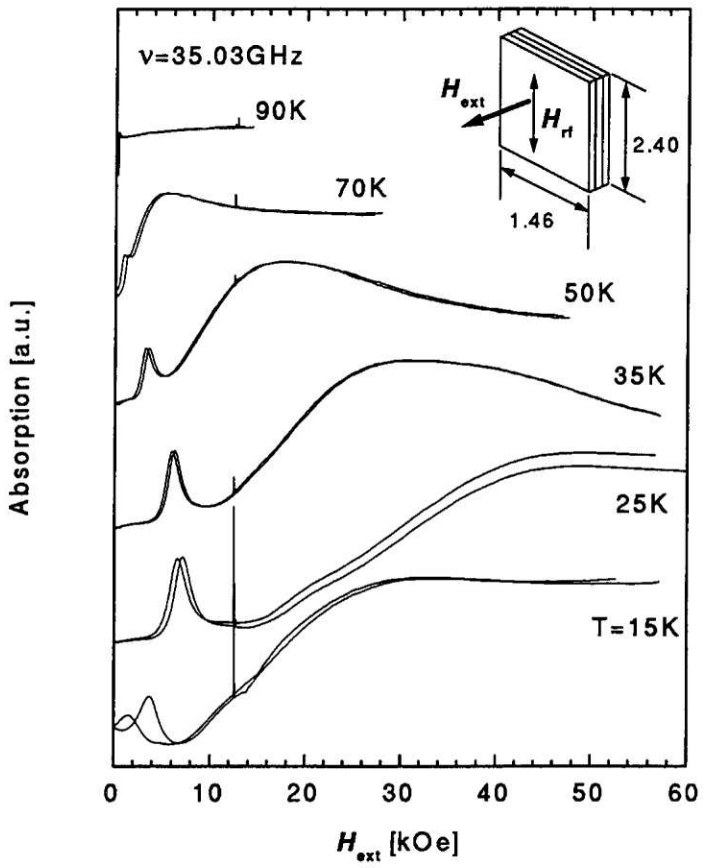


Figure 4.3: The resonance absorption of sample A for a fixed dimension of the *ab* plane at 35.0 GHz. The oscillating magnetic field ($\boldsymbol{H}_{\rm rf}$) is applied parallel to the *ab* plane. In this particular sample dimension, two transverse Josephson plasma resonance peaks can be observed. A sharp and rather symmetric resonance is observed at lower field, whereas a broad and asymmetric resonance is seen at a higher filed. A small and sharp spike at 12.48 kOe is due to ESR signal of DPPH as a magnetic field reference marker. The inset shows the sample geometry with configuration of microwave $\boldsymbol{H}$ vector and the external field.

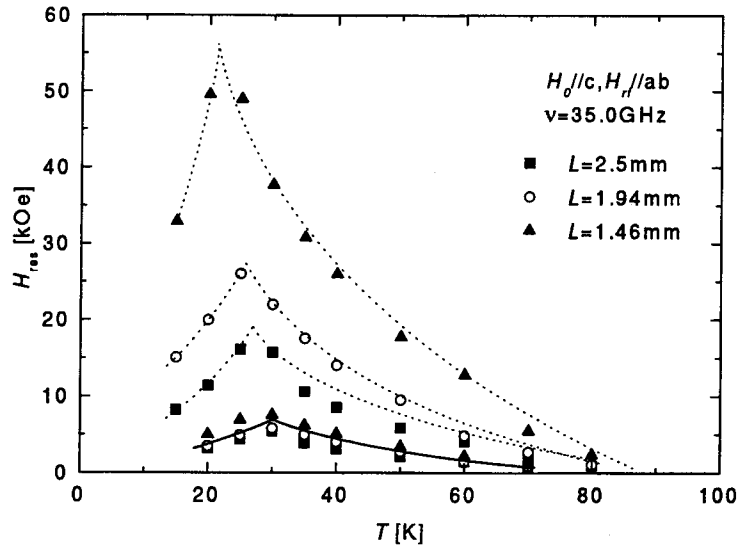


Figure 4.4: Temperature dependence of the transverse Josephson plasma resonance field for three different dimensions of the *ab* plane, 2.5 mm, 1.94 mm and 1.46 mm. Dotted and solid lines are the guide to the eye.

previously [1]. In this figure, the temperature dependence of the resonance lines for two other sample dimensions are also added.

The observed absorption lines at 25 K at various sample sizes are displayed in Fig. 4.5. Here, $L_\perp$, as shown in the inset of Fig. 4.5, is the sample length along the direction perpendicular to $\boldsymbol{H}_{\rm rf}$, which is varied, and the length along the parallel direction $L_\parallel$ to $\boldsymbol{H}_{\rm rf}$ is kept constant for all $L_\perp$. In this condition, the peak at higher field shifts to higher field as $L_\perp$ is reduced and the peak position sharply diverges at the critical length of $L^*$. The sample dimension $L_\perp$ is actually changed from 2.50 to 0.737 mm. The largest size is limited by the cavity size. In contrast, the lower resonance does not move despite changing the sample size. We note that the resonance absorption at the lower field remains at the same field, similar to the one for $\boldsymbol{E}_{\rm rf}||c$, although the intensity decreases as the size is reduced. We have checked the influence of the $L_\parallel$ on the resonance field $\boldsymbol{H}_{\rm res}$ for the case in $\boldsymbol{H}_{\rm rf}||ab$. It is experimentally confirmed that the resonance line did not shift at all.

As seen in Figs. 4.3 and 4.5, the characteristic feature in the case of $\boldsymbol{H}_{\rm rf}||ab$ is the line shape. The lower field line is sharp and has more or less a symmetric line shape, in strong contrast to the higher field line, which exhibits broad and rather asymmetric line shapes with a strong tail at the higher field side. When the sample size is reduced to the critical dimension $L^*$, the resonance line shifts sharply to the higher field side and becomes extremely broad, then disappears at $L^*$. Although the higher field resonance line is influenced by the dimension, the lower field line does not shift at all. The smallest sample dimension in this case was $L$=0.737 mm, limited by the detection limit of the resonance intensity.

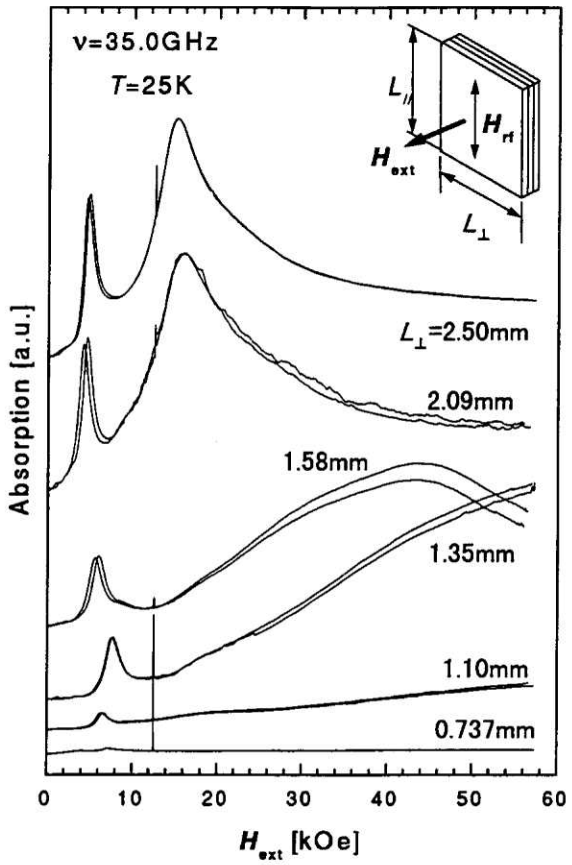


Figure 4.5: The absorption lines observed in sample A at 25 K at a various sample dimensions of the *ab* plane. The detailed sample geometry as well as the configuration between microwave $\boldsymbol{H}_{\rm rf}$ and external field $\boldsymbol{H}_{\rm ext}$ is shown in the inset. The sample size is reduced along one direction step by step, and the length along the other direction is fixed at 2.4 mm. The broad resonance at a higher field shifts to higher fields as $L$ decreases, while the sharp resonance at the lower field does not move. The absorption intensity decreases as $L$ is decreased.

## 4.4 Discussion

In this section, we will discuss the nature of the resonance which is observed under two different configurations, $\boldsymbol{E}_{\rm rf}\|c$ and $\boldsymbol{H}_{\rm rf}\|ab$. We take the $x$ and $y$ axes in the $ab$ plane and the $z$ axis along the $c$ axis of the samples in the following discussion.

### 4.4.1 Plasma excitation with a perpendicular oscillating electric field: longitudinal plasma

As described in Fig. 3.3, the sample is placed at the center of the cross section of the cavity at a distance $\lambda_g/4$ above the bottom of the cavity. In this case, the oscillating electric field $\boldsymbol{E}_{\rm rf}$ acts uniformly on the sample. (The inhomogeneity of the $\boldsymbol{E}_{\rm rf}$ in the sample with 1 mm $\times$ 1 mm size is estimated to be less than 5% over the sample.) Moreover, it is advantageous that, in this cavity mode, the electric vector $\boldsymbol{E}_{\rm rf}$ can be separated from the magnetic vector $\boldsymbol{H}_{\rm rf}$ without complication. This condition cannot be met by other cavity modes such as the cylindrical ones. If the external electric field $\boldsymbol{E}_{\rm rf}$ is uniform in the $ab$ plane, we can assume that the phase difference between the layers is also uniform in the direction parallel to the layers.

As discussed in Sec. 2.4.3, such excitation is generated as the longitudinal plasma, which has the dispersion relation;

$$\omega_{\rm L}(k_z) = \omega_p\sqrt{1+\epsilon\mu^2 k_z^2}. \tag{4.1}$$

As mentioned before $\epsilon\mu^2 \ll 1$ is satisfied, so that the dispersion can be neglected. Although the excited plasma is represented by the superposition of the standing waves with wave number $k_{2n+1} = (2n+1)\pi/d$, with $n$ and $d$ being integer and the thickness of the sample, the longitudinal plasma resonance has a sharp and little asymmetry of the line shape because of the dispersionless character of the longitudinal plasma expressed by Eq. (4.1). Similar results have been reported earlier by Bulaevskii *et al.* [21] for arbitrary $\boldsymbol{k}$, although they do not take into account the charge screening effect seriously.

In our experiment, $d$ is fixed for all $L$, and $\omega_{\rm L}$ is not sensitive to $k_z$, ensuring the flat dispersion. Therefore, $\omega_{\rm L}$ changes little unless $d$ varies drastically close to $L^*$. Experimental results [1] indicate that the plasma frequency $\omega_p$ depends on $H_{\rm ext}$ as $\omega_p \propto H_{\rm ext}^{-1/2}$, which enables us to rewrite $\omega_{\rm L}/\omega_p$ as $(H_{\rm ext}/H_0)^{1/2}$, where $H_0 = \Gamma^2/\omega_{\rm L}^2$ is the resonance field. Using this equations, it is found that the resonance field is also independent of $L$. The observed resonance field is indeed independent of $L$ within the experimental error. This agrees with the theoretical predictions discussed above.

### 4.4.2 Plasma excitation with a parallel oscillating magnetic field: transverse plasma

Let us consider a layered system whose dimension is $L$ along the $x$ axis and infinity along $y$ and $z$ axes as displayed in Fig. 4.6. When $\boldsymbol{H}_{\rm rf}$ is applied parallel to the $y$ axis with uniform intensity within the $ab$ plane, the screening current $\boldsymbol{j}$ is induced. As a result, the electric field $\boldsymbol{E}$ is formed in accordance with the London equations and the Maxwell's@bookMaxwel,'author="s equation" as follows:

$$\frac{4\pi}{c}\boldsymbol{j} = -\frac{1}{\lambda_c^2}\boldsymbol{A}, \tag{4.2}$$

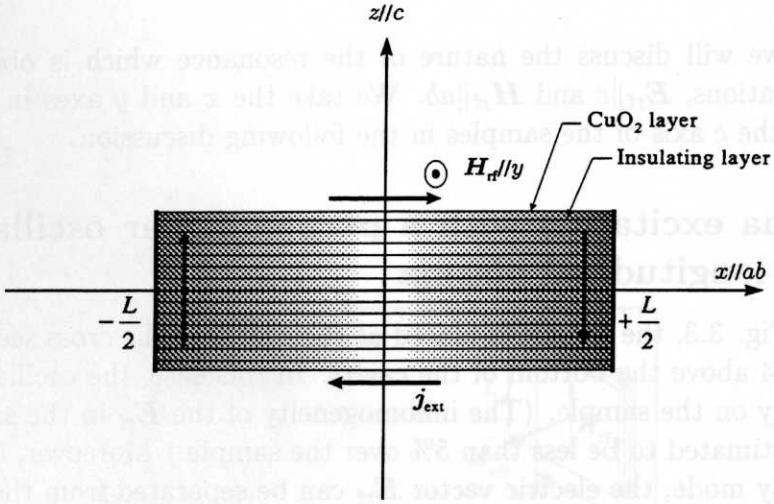


Figure 4.6: Schematic diagram of the crystal with microwave component $\boldsymbol{H}_{\rm rf}\|y$ for the transverse plasma excitation. The solid arrows indicate the hypothetical external current ($\boldsymbol{j}_{\rm ext}$) induced by $\boldsymbol{H}_{\rm rf}$. The current parallel to the $c$ axis penetrates much deeper than the one parallel to the $ab$ plane because $\lambda_c/\lambda_{ab}$ is as large as 1000 in $Bi_2Sr_2CaCu_2O_{8+\delta}$. This current along the $c$ axis drives the oscillating electric field of $\boldsymbol{E}_{\rm rf}$, which excites the transverse Josephson plasma.

$$\nabla \times \boldsymbol{B} = \frac{4\pi}{c}(\boldsymbol{j} + \sigma_{\rm qp}\boldsymbol{E}) + \frac{\epsilon}{c}\frac{\partial}{\partial t}\boldsymbol{E}, \tag{4.3}$$

$$\nabla \times \boldsymbol{E} = -\frac{1}{c}\frac{\partial}{\partial t}\boldsymbol{B}, \tag{4.4}$$

where $\boldsymbol{j} = (0, 0, j_z)$, $\boldsymbol{A} = (0, 0, A_z)$, $\boldsymbol{B} = (0, B_y, 0)$, and $\boldsymbol{E} = (0, 0, E_z)$. The normal mode of the electromagnetic wave inside the superconductor can be obtained by setting $B_y \propto \exp[ikx - i\omega t]$ into the Maxwell's equations (4.3) and (4.4). As a result, the following condition has to be satisfied:

$$k^2 + \frac{1}{\lambda_c^2} - \frac{4\pi}{c^2} i\omega\sigma_{\rm qp} - \frac{\epsilon}{c^2}\omega^2 = 0, \tag{4.5}$$

where $k$ is defined as $k = k' + ik'' = (\omega/c)\sqrt{\varepsilon(\omega)}$. Since $B_y$ must satisfy the boundary condition at $x = \pm L/2$ as $B(\pm L/2) = H_{\rm rf}$, $B_y$ can be obtained as

$$B_y = H_{\rm rf} e^{-i\omega t}\left[\frac{e^{ikx} + e^{-ikx}}{e^{ikL/2} + e^{-ikL/2}}\right]. \tag{4.6}$$

Therefore, the electric field $E_z$ can be displayed as

$$\begin{aligned} E_z &= -i\frac{\omega}{c}\int^x B_y dx \\ &= -\frac{\omega H_{\rm rf}}{ck} e^{-i\omega t}\left[\frac{e^{ikx} - e^{-ikx}}{e^{ikL/2} + e^{-ikL/2}}\right]. \end{aligned} \tag{4.7}$$

The power absorption $\wp = \int_{-L/2}^{L/2} dx \langle \mathrm{Re}j \cdot \mathrm{Re}E \rangle_t$ can be rewritten as

$$\begin{aligned} \wp &= \frac{1}{2}\sigma_{\mathrm{qp}} \int_{-L/2}^{L/2} dx |E_z|^2, \\ &= \frac{L}{2} H_{\mathrm{rf}}^2 \frac{\sigma_{\mathrm{qp}}}{\varepsilon(\omega)} \left( \frac{\sinh k''L/k''L - \sin k'L/k'L}{\cosh k''L + \cos k'L} \right), \end{aligned} \tag{4.8}$$

where $\varepsilon(\omega) = \epsilon(1 - \omega_p^2/\omega^2) + 4\pi i \sigma_{\mathrm{qp}}/\omega$. Since the resonance peaks originate from the pole of Eq. (4.8), this condition yields either $\varepsilon(\omega) = \epsilon(1 - \omega_p^2/\omega^2) = 0$ or $1 + \cos((\omega/c)\sqrt{\varepsilon(\omega)}L) = 0$. The former equation leads the fundamental resonance at $\omega = \omega_p$, while the latter equation gives the multiple resonance at the frequencies given as

$$\frac{\omega_n^2}{\omega_p^2} = \frac{1}{1 - \left[ \dfrac{(2n-1)\pi}{\sqrt{\epsilon}L/(c/\omega)} \right]^2} \quad (n = 1, 2, \ldots). \tag{4.9}$$

As mentioned before, we can rewrite $\omega^2/\omega_p^2$ for $H/H_0$, thus the resonance field is determined by Eq. (4.9),

$$\frac{H_n}{H_0} = \frac{1}{1 - \left[ \dfrac{(2n-1)\pi}{\sqrt{\epsilon}L/(c/\omega)} \right]^2}, \tag{4.10}$$

where $H_0$ denotes the resonance field of the large $L$ limit. This implies that the multiple-resonance lines may be observed, depending on the sample size $L$. For instance, double resonance lines are observable with condition of $4.05\,\mathrm{mm} \leq L \leq 6.75\,\mathrm{mm}$ for $\epsilon = 10$ and $\omega/2\pi = 35\,\mathrm{GHz}$, whereas a single resonance is expected in $1.35\,\mathrm{mm} \leq L \leq 4.05\,\mathrm{mm}$. It is noted that there is only a fundamental mode when the sample size is smaller than 1.35 mm.

Figure 4.7 shows the experimental results of the resonance field as a function of $L$ for two orientations of the $\boldsymbol{H}_{\mathrm{rf}}$ with respect to the $a$ and $b$ axes. The resonance lines for both configurations of $\boldsymbol{H}_{\mathrm{rf}}$ show the sharp divergent behavior as the sample size is reduced. The solid lines are the fitted curves using Eq. (4.10) with a single parameter $\epsilon$. As seen in Fig. 4.7 the agreement between the experimental results and the fitted curve is excellent. From this analysis the value of $\epsilon = 8.47$ is deduced for $\boldsymbol{H}_{\mathrm{rf}} \| a$.

## 4.5 Conclusions

The author has measured the Josephson plasma resonance as a function of the sample size $L$, and characterized the longitudinal and the transverse plasma modes. It is of importance to stress here that the two plasma modes were experimentally separated out and were identified independently.

The longitudinal plasma is excited by a perpendicular oscillating electric field ($\boldsymbol{E}_{\mathrm{rf}} \| c$), exerted uniformly in the $ab$ plane. Since the resonance field, which is equivalent to the Josephson plasma frequency, is independent of the dimension in the $ab$ plane in this case, the longitudinal plasma, which propagates with the wave vector $\boldsymbol{k}$ perpendicular to the layers, is actually independent of $|\boldsymbol{k}|$.

In contrast, by applying the parallel oscillating magnetic filed ($\boldsymbol{H}_{\mathrm{rf}} \| ab$), the transverse plasma can be generated, which propagates parallel to the $ab$ plane. Therefore, the Josephson

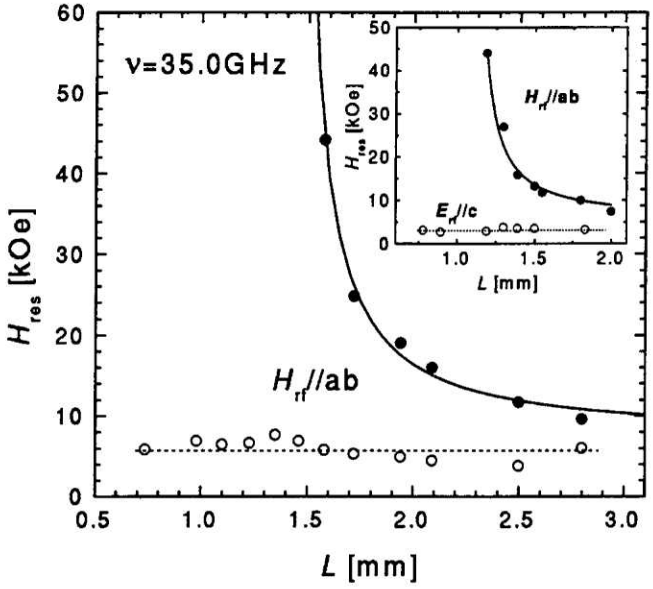


Figure 4.7: The resonance field diagram for sample A as a function of the sample size $L$ at 35 GHz and 25 K. The solid symbols indicate the transverse plasma resonance, which shows divergent character in the case of $\boldsymbol{H}_{\rm rf}||ab$, and solid lines indicate the fitted results by Eq. (4.10). The open symbols represents the sharp resonance field which appears at the lower filed. The horizontal dotted line is put as a guide to the eye. The inset displays the same diagram for sample B in which the size dependence of the resonance in $\boldsymbol{E}_{\rm rf}||c$ was also measured.

plasma resonance observed in this configuration strongly reflects the dispersion relation. This results in the appearance of the strong *ab* plane size dependence. The shift of the resonance field by reduction of $L$ is quantitatively explained by Eq. (4.10) with a single parameter $\epsilon$, and is in good agreement with the picture of the layered superconducting system with finite size of the plane [12]. The result of the fitting gives the value $\epsilon = 8.47$. This good agreement ensures that the theoretical model used here is appropriate to describe the Josephson plasma phenomena. This sharply contradicts the approach given by Bulaevskii *et al.* [3, 4, 5, 21], who do not take into account the charge screening effect in their treatment, although the final result is almost identical. This charge screening effect is the most essential difference in the layered system such as $Bi_2Sr_2CaCu_2O_{8+\delta}$ in comparison with the conventional Josephson junctions.

According to the concept of the spontaneously broken symmetry, the symmetry of the phase degree of freedom of the gauge field is broken in the superconducting transition [13, 14, 15, 16]. The longitudinal plasma mode is the collective excitation mode, also called the phason mode or the Nambu-Goldstone mode [17]. However the transverse plasma mode is not the Nambu-Goldstone mode in a superconductor.

In a conventional superconductor, the plasma modes (both longitudinal and transverse mode) have an energy gap, which is of the order of eV, far beyond the superconducting energy gap of a few meV. This energy gap was predicted by Anderson [13], who took into account the long-range Coulomb interaction effect in the theory of superconductivity. The energy level is identical to the plasma energy in the normal state, which lies at such high energies that the excitation mode cannot be distinguished from the quasiparticle excitations with the strong Landau damping. Therefore, there has been no experimental confirmation of the plasma mode in a superconductor, especially the longitudinal plasma mode (Nambu-Goldstone mode).

The Josephson plasma mode is nothing but the superconducting plasma mode associated with the Josephson Cooper pair tunneling through insulating layers and has been proved to exist in the present high-$T_c$ superconductor $Bi_2Sr_2CaCu_2O_{8+\delta}$ [5, 10, 17]. As explained in Sec. 4.4, we were able to separate the two Josephson plasma modes experimentally. This enables us to identify the longitudinal Josephson plasma mode separately from the transverse one. This was experimentally carried out by measuring the sample size dependence of the resonance, which is derived from the difference in the dispersion relations of the two modes. The experimental result agrees very well with the theoretical prediction as described in Sec. 4.4. Therefore, it is concluded that we have experimentally confirmed the existence of the Nambu-Goldstone mode in a superconductor, which has a finite gap as described by the Anderson-Higgs mechanism [16, 18, 19]. We also note that although the Carlson-Goldman mode [22] in a conventional Josephson junction was shown to be the Nambu-Goldstone mode, the excitation is only possible with strong coupling between Cooper pairs and quasiparticles. Therefore, this excitation may be only observable in the very vicinity of $T_c$.

# Bibliography


[1] Ophelia K. C. Tsui, N. P. Ong, Y. Matsuda, Y. F. Yan, and J. B. Peterson, Phys. Rev. Lett. **73**, 724 (1994).

[2] Y. Matsuda, M. B. Gaifullin, K. Kumagai, K. Kadowaki, and T. Mochiku, Phys. Rev. Lett. **75**, 4512 (1995).

[3] L. N. Bulaevskii, M. P. Maley, and M. Tachiki, Phys. Rev. Lett. **74**, 801 (1995).

[4] L. N. Bulaevskii, V. L. Pokrovsky, and M. P. Maley, Phys. Rev. Lett. **76**, 1719 (1996).

[5] L. N. Bulaevskii, D. Dominguez, M. P. Maley, A. R. Bishop, Ophelia K. C. Tsui and N. P. Ong, Phys. Rev. B **54**, 7521 (1996).

[6] A. E. Koshelev, Phys. Rev. Lett. **77**, 3901 (1996).

[7] Ophelia K. C. Tsui, N. P. Ong, and J. B. Peterson, Phys Rev. Lett. **76**, 819 (1996).

[8] S. Sakamoto, A. Maeda, T. Hanaguri, Y. Kotaka, J. Shimoyama, K. Kishio, Y. Matsushita, M. Hasegawa, H. Takei, H. Ikeda, and R. Yoshizaki, Phys. Rev. B **53**, R14 749 (1996).

[9] T. Shibauchi, M. Sato, A. Mashio, T. Tamegai, H. Mori, S. Tajima, and S. Tanaka, Phys. Rev. B **55**, 11 977 (1997).

[10] M. Tachiki, T. Koyama, and S. Takahashi, Josephson Plasma in High Temperature Superconductors, *Coherence in Superconductors*, edited by G. Deutscher, and A. Revcodevschi (World Scientific 1996).

[11] K. Kadowaki, M. B. Gaifullin, Y. Matsuda, K. Kumagai, S. Takahashi, and M. Tachiki, Czech. J. Phys. **46**, Suppl. S3, 1625 (1996).

[12] S. Takahashi, M. Tachiki, I. Kakeya, K. Kindo, T. Mochiku, and K. Kadowaki, Physica C **293**, 64 (1997).

[13] P. W. Anderson, Phys. Rev. **110**, 827 (1958).

[14] G. Ryckayzen, Phys. Rev. **111**, 817 (1958).

[15] Y. Nambu, Phys. Rev. **117**, 648 (1960).

[16] J. Goldstone, A. Salam, and S. Weinberg, Phys. Rev. **127**, 965 (1962).

[17] K. Kadowaki, I. Kakeya, M. B. Gaifullin, T. Mochiku, S. Takahashi, T. Koyama, and M. Tachiki, Phys. Rev. B **56**, 5617 (1997).

[18] P. W. Anderson, Phys Rev. **112**, 1900 (1958).

[19] P. Higgs, Phys. Rev. **145**, 1156 (1966).

[20] T. W. B. Kibble, Phys. Rev. **155**, 1554 (1967).

[21] L. N. Bulaevskii, M. Zamora, D. Baeriswyl, H. Beck, and John R. Clem, Phys. Rev. B **50**, 12 831 (1994).

[22] R. V. Carlson and A. M. Goldman, Phys. Rev. Lett. **34**, 11 (1975).

# Chapter 5

# Josephson plasma in the vortex state

## 5.1 Introduction

Physics of high temperature superconductors have widely attracted much interests of a great many physicists during past 10 years after the unprecedented historical discovery of the phenomena by Bednorz and Müller [1]. Although this phenomena is fascinating and leaving us opportunities to have been room temperature superconductors, no clear answer is yet established to be as the mechanism of high-$T_c$ superconductors. Besides the fundamental mechanism to the superconducting state is also bizarre enough in comparison with the conventional knowledge of superconductors. Large critical current densities and extremely high $H_{c2}$ (later to be replaced to the irreversibility line $H_{\rm irr}$) are most attractive features in the properties of type-II superconductors, especially for practical applications. However, it has been found shortly that these features are lost at higher temperatures, the superconducting state easily become sensitive even in a small magnetic field. Much effort and a number of approaches have been tried to understand such features on the basis of conventional flux dynamics without much success. This is because of neglecting the fundamental aspects of high temperature superconductors: short coherence length and layered characteristic structure. These two physical properties are essentials to understand correctly the nature of vortex state in high temperature superconductors. As a consequence, the vortex phase diagram in type-II superconductors has been renewed entirely and reinterpreted. Such a revolutional transition in physics after 50 years of its establishment is rare and unprecedented in the history of physics.

The research of the vortex state in high-$T_c$ superconductors is now one of the current subject being most important in the field of solid state physics. Macroscopic properties such as magnetization, critical currents, and resistivity have been studied based on an appropriate model for high temperature superconductors, which needed to be confirmed by microscopic experimental means, neutron scattering and muon spin rotation ($\mu$SR) techniques, for example. These are not easy at all. The Josephson plasma resonance is a unique experiments to provide microscopic informations as briefly explained in the previous chapter. This is our purpose to describe the results of Josephson plasma resonance in the vortex state of $Bi_2Sr_2CaCu_2O_{8+\delta}$ (BSCCO).

We have performed the Josephson plasma resonance experiments in the vortex state of highly 2D-like layered superconductor BSCCO with a special emphasis on the magnetic field orientation and two strengths of pinning forces. The applied magnetic field is rotated in the plane which includes the $c$ axis. Samples used in the present experiments are pristine

crystals and irradiated samples with doses equivalent to the magnetic field of $B_\phi = 0.2$, 0.5, and 2 T, in which columnar defects penetrated through the sample along the $c$ axis. This sort of defects are known to give enhancement in the vortex pinning, whose mechanism studied by the Josephson plasma resonance as a excellent example.

The most powerful idea is the relation to the gauge invariant phase difference between two adjacent layers [2, 3, 4, 5];

$$\langle \cos \varphi_{\ell,\ell+1} \rangle \propto \frac{1}{TH^{\mu}}, \tag{5.1}$$

where $\varphi_{\ell,\ell+1}$ is the gauge invariant phase difference between the $\ell$ and $\ell+1$ th layers. Here, $\mu$ is estimated to be $0.7 - 0.8$ in lower temperature range and $0.9 - 1$ in higher temperature range. This reation is not valid, especially in the vortex solid phase, and may be extented with a serious modifications. We also note here that the Josephson plasma resonance is observed even in $\boldsymbol{H} \parallel ab$, where the physical picture shown in Eq. (5.1) is no longer applicable. A possible mechanism for the resonance in such a case will also be discussed later.

The plasma resonance in oblique or parallel magnetic fields to the superconducting $CuO_2$ plane has been reported in samples without or with columnar defects. There are also some experimental reports for angular dependence of the resonance including results in a parallel magnetic field ($\boldsymbol{H} \parallel ab$) [6, 7, 8]. The Josephson plasma resonance in a parallel or a slightly tilted field is a very interesting phenomena in strongly two-dimensional layered superconductors such as BSCCO. In an *ideally* parallel field, no pancake vortex which drives the Josephson plasma resonance in a perpendicular field exists since vortices penetrate into the insulating layers as "Josephson vortices" not the superconducting layers. It is not clear yet, on the other hand, as to what dynamical mechanism causes the resonant absorption observed in the parallel magnetic field, although there have been theoretical arguments on this particular situation [9, 10]. We discuss experimental results in comparison with theoretical predictions.

The Josephson plasma resonance measurements in BSCCO with columnar defects have been also reported by several authors [11, 12, 13]. Although they presented the temperature dependence of the resonance with columnar defects and gave qualitative analyses, there are no systematic physical picture which connects the behavior of the Josephson plasma resonance in pristine and irradiated BSCCO samples quantitatively as a function of pinning strength. We propose a unified picture to account for the plasma resonance phenomenologically by considering the effective anisotropy parameter $\alpha$ in the scalling approach, where the $\alpha$ value is astrong function of the dose of the columnar defects. Finally, we mention that the Josephson plasma phenomenon is a very useful mean to study the nature of the quasi-particles in order to understand the dynamical features of superconducting electrons. Although this is another fascinating subject to be discussed, we focused on the subject of the vortex state and leave a possibility to describe it for the another occasion.

In this chapter, we demonstrate our experimental results of the Josephson plasma resonance in various sample with and without columnar defects. Here, the angular dependence in different amount of doses is a point of main concern. Moreover, the plasma resonance in external fields in a vicinity of the $ab$ plane is investigated in detail, in order to establish qualitative pictures of the Josephson plasma resonance in a parallel or slightly tilted fields. The basic picture of the vortex state in high-$T_c$ superconductors is shown before the experimental details and the arguments.

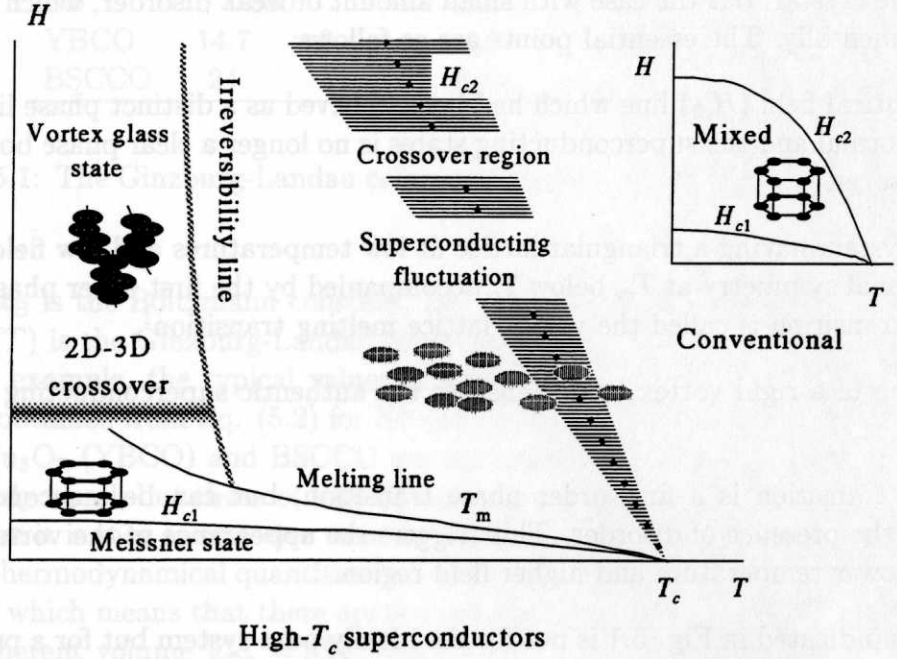


Figure 5.1: The magnetic field-temperature diagram of high-$T_c$ superconductors. The hatched ellipse indicates a pancake vortex. The substance is perfectly diamagnetic and no vortex penetrates in it in the Meissner state. Above $H_{c1}$, the penetrated vortices form a triangular lattice below the melting line, and the pancakes stuck along the $c$ axis. In the vortex glass state, although the vortices are not ordered to the regular lattice state, the arrangements of vortices is highly disordered due to pinning effect by pining centers which are distributed randomly. In this state, the vortices are ordered in a "glassy"solid phase. In the fluctuating state, the vortices are freely mobile just as liquid without having the translational symmetry. This state is no longer superconducting state, i.e., it is the normal state. The upper-right figure is the phase diagram of conventional type-II superconductors. In their "mixed" state, the vortices form a triangular lattice above the lower ($H_{c1}$) below the upper ($H_{c2}$) critical fields without serious fluctuations.

## 5.2 Vortices in high temperature superconductors

### 5.2.1 Field-temperature phase diagram in high temperature superconductors

The most striking development after the studies towards the more appropriate picture of high temperature superconductors in magnetic fields is a drastic revision of the field-temperature phase diagram of the vortex state in type-II superconductors. Although the vortex state is considered starting from a simple triangular (Abrikosov) lattice in the mixed state of conventional superconductors, it is not the case in high-$T_c$ superconductors. Many new names for the new vortex states have been created; pancake vortex state, vortex glass state, and state with superconducting fluctuations etc.

The phase diagram of high-$T_c$ superconductors when a magnetic field is applied parallel

to the $c$ axis ($\boldsymbol{H} \parallel c$) is shown in Fig. 5.1. We remind that this is not the case for the "pure" samples (pure single crystal) but the case with small amount of weak disorder, which cannot be removed experimentally. The essential points are as follows:

- The upper critical field ($H_{c2}$) line which had been believed as a distinct phase line separating the normal and the superconducting states is no longer a clear phase boundary but is a crossover.
- The vortex system having a triangular lattice at low temperatures and low fields loses the translational symmetry at $T_m$ below $T_c$ accompanied by the first order phase transition. This transition is called the vortex lattice melting transition[1].
- The formation of a rigid vortex lattice ensures the authentic superconducting transition.
- The melting transition is a first order phase transition, but can be a second order transition in the presence of disorder. This triggers the appearance of the vortex glass state in the lower temperature and higher field region.

The phase diagram indicated in Fig. 5.1 is not for the ideally pure system but for a practical substance with weak pinning centers. The boundary between vortex glass and superconducting fluctuating states is still obscure. It is yet controversial as to what is the nature of this phase transtio.

Since most of high-$T_c$ superconductors, especially for BSCCO, have layered structures which involve the Josephson coupling in the unit cell as described in Sec. 2.4, the superconducting order parameter spatially inhomogeneous. This fact provides the characteristic properties of high-$T_c$ superconductors, and make the phase diagram further complicated.

### Disappearance of the upper critical field

The phase diagram of the type II superconductors has been thought for a long time to be established in the form as shown in the inset of Fig. 5.1. The superconducting phase is sharply separated from the normal state by the upper critical field $H_{c2}$. In high $T_c$ superconductors this sort of phase diagram has been in doubt since there is no clear phase line to distinguish the normal and superconducting phase. It turns out after several years study of the vortex state that the upper critical field $H_{c2}$ does not exist not only for high-$T_c$ superconductors but also for conventional ones in the strict sense [19]. It is surprising that such a misinterpretation has been accepted for more than half century since the discovery of the type-II superconductors. The mixed state of the conventional superconductors is well described by the Ginzburg-Landau theory and the mean field approximation is very effective for conventional superconductors. In the mean field treatment, $H_{c2}$ appears as a second order phase transition, and its fluctuation of conventional type-II superconductors is so small that the effect is negligible. This is in fact an extremely good approximation. The shift in temperature due to the fluctuation effect is practically obtained by the Ginzburg criterion as [20]

$$\frac{T}{T_c} - 1 \leq \frac{1}{32\pi^2}\left[\frac{k_{\mathrm{B}}}{\Delta C \xi_{ab}^2(0)\xi_c(0)}\right]^2, \tag{5.2}$$

[1]The vortex lattice transition is confirmed by Zeldov *et al.* [14]. They observed a sharp discontinuity in the local magnetization measurement by micro Hall probes glued on the surface of the BSCCO single crystal.

| | $\xi_{ab}$[Å] | $\xi_c$[Å] | $\Delta C$[J/mol·K] | $T_c$[K] | $\Delta T$[K] | Reference |
|---|---|---|---|---|---|---|
| Nb | 380 | | 1.5 | 9.23 | $8.2 \times 10^{-10}$ | [15, 16] |
| YBCO | 14.7 | 2 | 4.6 | 92 | 0.2 | [17, 18] |
| BSCCO | 24 | 1 | 0.65 | 87 | 10 | [18] |

Table 5.1: The Ginzburg-Landau coference lengths and the fluctuations at $T_c$ derived by Eq. 5.2.

where $k_B$ is the Boltzmann constant, $\Delta C$ is the jump of the specific heat at $T_c$, and $\xi_{ab}(T)$ and $\xi_c(T)$ is the Ginzburg-Landau coherence lengths for $ab$ plane and $c$ axis, respectively.

For example, the typical values of some parameters and the fluctuation region $\Delta T \equiv T - T_c$ obtained from Eq. (5.2) for Nb (an example of conventional type-II superconductors), $YBa_2Cu_3O_7$ (YBCO) and BSCCO are summarized in Table. 5.1. The fluctuation of Nb is negligibly small, but those of high-$T_c$ materials, YBCO and BSCCO, are considerably large therefore it is easy to conceive that the superconducting fluctuations play an important role in the thermodynamical quantities in a wide range around $T_c$. The extremely short coherence length, which means that there are few number of the interacting superconducting electrons in a coherent volume $V_{\rm coh} = \xi_{ab}^2 \xi_c$ ($N_{\rm coh}^s \equiv N^s \times V_{coh} \simeq 0.8$ for BSCCO with $N^s$ being the supersonducting electron density), provides this noticeable difference of the superconducting fluctuation as indicated in Table 5.1.

The fluctuating region is enlarged by applying a magnetic field as the following:

$$\frac{T}{T_c(H)} - 1 \leq \left[\frac{k_B H}{\Delta C \phi_0 \xi_c(0)}\right]^{2/3}, \tag{5.3}$$

with $\phi_0$ being the flux quantum. Substituting the values in Table 5.1 into Eq. (5.3), $\Delta T \simeq 2.2$ and 15 K are obtained at $H = 50$ kOe for YBCO and BSCCO, respectively. The reason why the superconducting fluctuation is enhanced by externally applied magnetic field is that the effective number of electrons in $V_{\rm coh}$ is further reduced because the magnetic field suppresses the motion of superconducting electrons in the Landau orbits. In the region around $H_{c2}$, the properties of high-$T_c$ superconductors is dominated by the superconducting fluctuations and the phase transition is dimmed as described above. In this state, the long-range order of the vortex system is absent. Therefore, this state is equivalent to the normal state. The true superconducting ordered state cannot be realized neither having perfectly diamagnetism nor maintaining a rigid vortex lattice.

### 5.2.2 The vortex lattice in oblique field

Considering that the applied magnetic field is tilted from the $c$ axis to the $ab$ plane. We expect to observe various fascinating phenomena with reflecting the anisotropic superconducting properties of high-$T_c$ superconductors. Systems with small anisotropy can be described by the anisotropic three dimensional effective mass model. Champbell *et al.* [21] and Thiemann *et al.* [22] described the vortex lattice state assuming an uniaxial anisotropy using the London approximation when the magnetic field is tilted from the uniaxial symmetry axis. This approach may be applicable to YBCO with anisotropy parameter $\gamma \equiv \xi_{ab}/\xi_c \sim 8$. However, this model may not be adequate when the system is much more anisotropic such as BSCCO ($\gamma \sim 10^3$), which is well described as a stack of SIS Josephson junctions. In such a layered

superconductor, the flux line may be well defined in the strongly superconducting $CuO_2$ layer region, but it may not be well defined at the insulating interlayer region where the shielding current is not well established. As a result, the flux line can be approxmated as if it is quantized inside the $CuO_2$ layers. It may behave as a series of thin disk-like vortices, which are called as a pancake vortices. Clem [23] discussed the stability of the pancake vortices in arbitrary oblique magnetic fields in a weak coupling limit. They showed that the pancakes are aligned with the magnetic field even if it is tilted from the $c$ axis. Koshelev [24] also argued that the pancake vortices are treated regarding as kinks of the flux lines for the magnetic field close to the $ab$ plane. See Fig 5.2 (a).

Feinberg and Villard [25] have given a phenomenological treatment of the general cases in which $\boldsymbol{H}$ is applied to the direction with a finite angle $\theta$ from the planes. They predict that there is a finite lock-in angle $\theta_c$, such that when $\theta < \theta_c$, the flux lines run strictly parallel to the planes, and are "locked in" between the layers. Here, $\theta_c$ is represented as

$$H \sin\theta_c = H_{c1\perp}(1 - N_c) \equiv H^*, \tag{5.4}$$

with $H_{c1\perp}$ being the lower critical field in a perpendicular field, and $N_c$ being the demagnetization factor along the $c$ axis, and we define the effective lower perpenduicular crtical field $H^*$, here. This implies a "transverse Meissner effect," with the component of $\boldsymbol{B}$ perpendicular to the planes being zero, not just reduced in magnitude by the magnetization, as in continuum in GL theory. The confined vortices (Josephson vortices) make a triangular lattice, which is distorted according to the anisotropy value in low flux density regime (Fig. 5.2 (b)).

## 5.3 Experimental details

The measurements were performed for four BSCCO single crystals. All the specimens were crystallized by the TSFZ technique described in Sec. 3.3, the boules were cleaved and cut into thin plates with thickness of several tens micrometers along the $c$ axis and a few millimeter square in the $ab$ plane. Three of them were irradiated by heavy ions to produce columnar defects before the experiments. 650 MeV iodine and xenon heavy ions $I^{28+}$ and $Xe^{31+}$ are used for the irradiation produced by the tandem accerelator at JAERI. After irradiation, the sample has columnar defects, at which region become an amorphous material with a diameter of 60 – 70 Å. As a result, the columnar defects can be considered as the insulating, non superconducting region, which may be suited for ideal pinning centers. The density of columnar defects $N_{\rm col}$ is characterized by the matching field $B_\phi$. The matching field means the equivalent magnetic field corresponding to the flux density when every columnar defect is occupied by a single flux quantum $\phi_0$. For example, $B_\phi = 1.0\,\mathrm{T}$ corresponds to $N_{\rm col} = 5.0 \times 10^{10}\ \mathrm{cm}^{-2}$. The matching fields and their superconducting transition temperatures $T_c$ for four samples used in the present study are listed in Table 5.2. $T_c$ was measured in a SQUID magnetomrter.

All Josephson plasma measurements described in this chapter have been performed in the configuration of $\boldsymbol{E}_{\rm rf} \parallel c$, so that the specimens are always placed at the position (a) in Fig 3.3. The direction of the external field measured from the $ab$ plane is changed by horizontally rotating the cavity by the high precision goniometer with an accuracy of $10^{-3}$ degree.

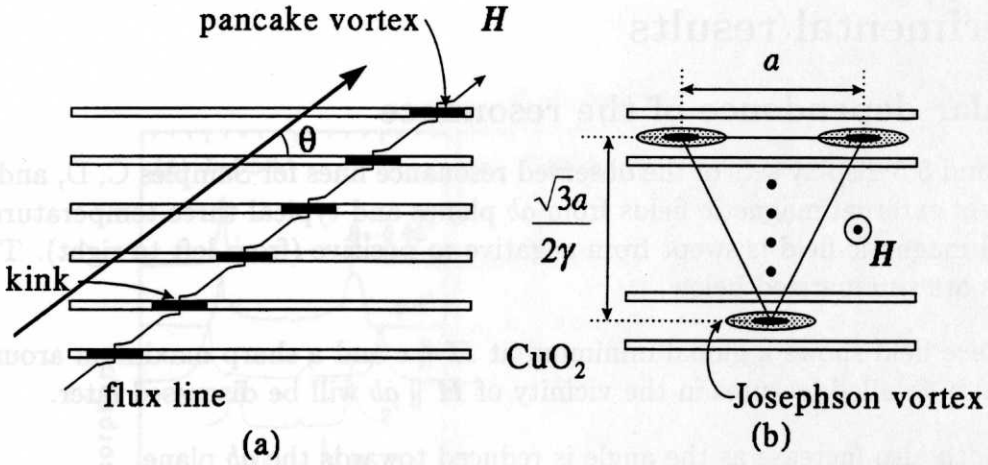


Figure 5.2: Schematic views of layered cuparate superconductors in (a) an oblique and (b) a parallel field. (a) Pancakes line up by forming kinks as if the vortex line penetrates straight. The net magnetization of the specimen is parallel to the $c$ axis despite that the field is tilted from the $c$ axis because the magnetization is contributed by only the pancake vortices. (b) In the low field region, the Josephson vortices are formed with a distorted triangular lattice in according with the anisotropy. It is noted that the vertical scale of this figure is not scaled. When $\theta$ is finite but less than the lock-in angle $\theta_c$ the Josephson vortex state is realized. The net magnetic moment points to the $ab$ plane in this case since the pancake contribution is absent.

| | Irradiated ion | $N_{\rm col}$ [cm$^{-2}$] | $B_\phi$ [T] | $T_c$ [K] |
|---|---|---|---|---|
| Sample C | – | 0 | 0 | 78 |
| Sample D | $I^{28+}$ | $1.0 \times 10^{10}$ | 0.2 | 91 |
| Sample E | $I^{28+}$ | $2.5 \times 10^{10}$ | 0.5 | 91 |
| Sample F | $Xe^{31+}$ | $1.0 \times 10^{11}$ | 2.0 | 87 |

Table 5.2: Matching fields $B_\phi$ and critical temperatures $T_c$ for every samples. $N_{\rm col}$ denotes the density of columnar defects. The density of defects is calibrated with a dry plate located behind the specimen during the irradiation.

In the following, the obtained experimental results as functions of external field $H$, temperature $T$, and field direction $\theta$ are shown and discussed. All of the data were measured by sweeping external field and by varying other parameters for the measurement.

## 5.4 Experimental results

### 5.4.1 Angular dependence of the resonance

Figures 5.3, 5.4, and 5.5 display sets of the observed resonance lines for Samples C, D, and F at various angles of external magnetic fields from $ab$ planes and typical three temperatures. Here the external magnetic field is swept from negative to positive (from left to right). The observed features are summarized below.

1. The resonance field shows a global minimum at $\boldsymbol{H} \parallel c$ and a sharp maximum around $\boldsymbol{H} \parallel ab$. More detailed features in the vicinity of $\boldsymbol{H} \parallel ab$ will be discussed later.

2. The line width also increase as the angle is reduced towards the $ab$ plane.

3. At higher temperatures above $T^* \sim 80\,\mathrm{K}$, the angular dependence of all samples C, D, and F looks similar. The resonance field and the line width monotonically increases with the field angle approaching the $ab$ plane. As a result, the resonance field shows a sharp peak at $\boldsymbol{H} \parallel ab$.

4. The resonance line intensity above $T^*$ seems to become weak and broad considerably near $\boldsymbol{H} \parallel ab$.

5. On the contrary, the resonance field shows complicated behaviors at low temperatures below $T^*$. In a very narrow angle region for the pristine sample, the resonance field has a hysteretic behavior with additional resonance lines. This feature will be described in the following part.

6. For the irradiated samples, the angular dependence has double peaks near $\boldsymbol{H} \parallel ab$. The opening angle for the outer peak depends strongly on the irradiated dose, whereas the opening angle for the inner peak hardly depends on the irradiation doses.

The detailed angular dependence in the vicinity of $ab$ plane ($|\theta| \leq 1°$) for the pristine sample (Sample C) is shown in Fig. 5.6. The fine features as a function of field angle can be seen, which cannot be seen in the irradiated sample, since the angular dependence is sharpest in the pristine sample. As seen in Fig. 5.6, at 35 K the additional resonance begins to appear within $\pm 2°$ from the $ab$ plane near zero field. As the external field approaches the $ab$ plane, this line grows and shifts to higher fields. The line shape and the position as functions of field angle and field intensity are not regular and systematic; sometimes it splits into multiple lines at an angle very close to the $ab$ plane (see Fig 5.6(a)). When $\boldsymbol{H} \parallel ab$, this line with complicated features appears only in the increasing field. With decreasing field, the resonance line is very sharp and symmetric as functions of both field angle and field intensity. At 55 K, the additional line becomes a sharper and single line. Note that this line appears even for the decreasing field. At 75 K as seen in Fig. 5.6 (c), the additional feature no longer appears and broadening of the main resonance line was observed. In the irradiated samples such a complicated feature can also be seen for $B_\phi = 0.2\,\mathrm{T}$ sample (Sample D) but not for

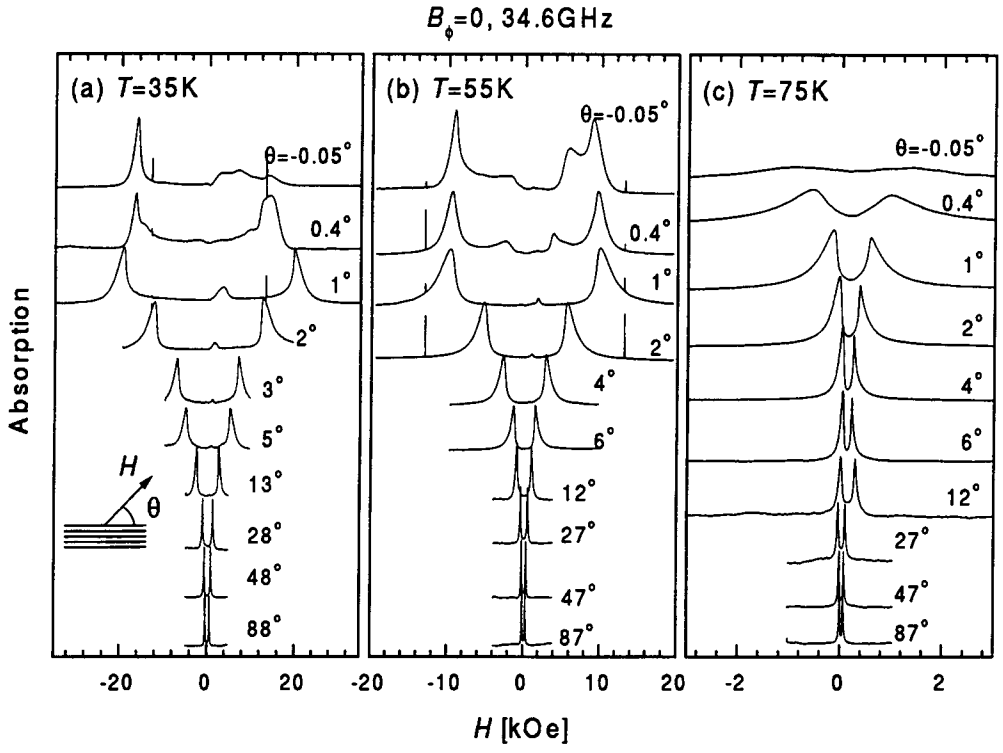


Figure 5.3: Angular dependence of the longitudinal Josephson plasma resonance in a pristine ($B_\phi = 0$) BSCCO single crystal at (a) 35 K, (b) 55 K, and (c) 75 K. The external magnetic field $\boldsymbol{H}$ is swept from negative to positive value for all panels, and $\theta$ is the angle between $\boldsymbol{H}$ and the $ab$ plane of the specimen as shown in the inset. Although the vertical scales of each panels are not exactly calibrated, resonance intensities in individual panels are comparable. It is noted that the vertical separations of the resonance line with different angles $\theta$ are not scaled. In higher angle regions (lower part of the panels), only a sharp and symmetric resonance is observed for all temperatures, and the resonance fields and the linewidths gradually increase as $\theta$ increases. In (a) and (b), the additional resonance appears at $\theta \simeq 5°$ with increasing field, and the resonance becomes quite asymmetric (hysteretic) with the field being closer to the plane. The details in the very vicinity of the plane are displayed in Fig. 5.6

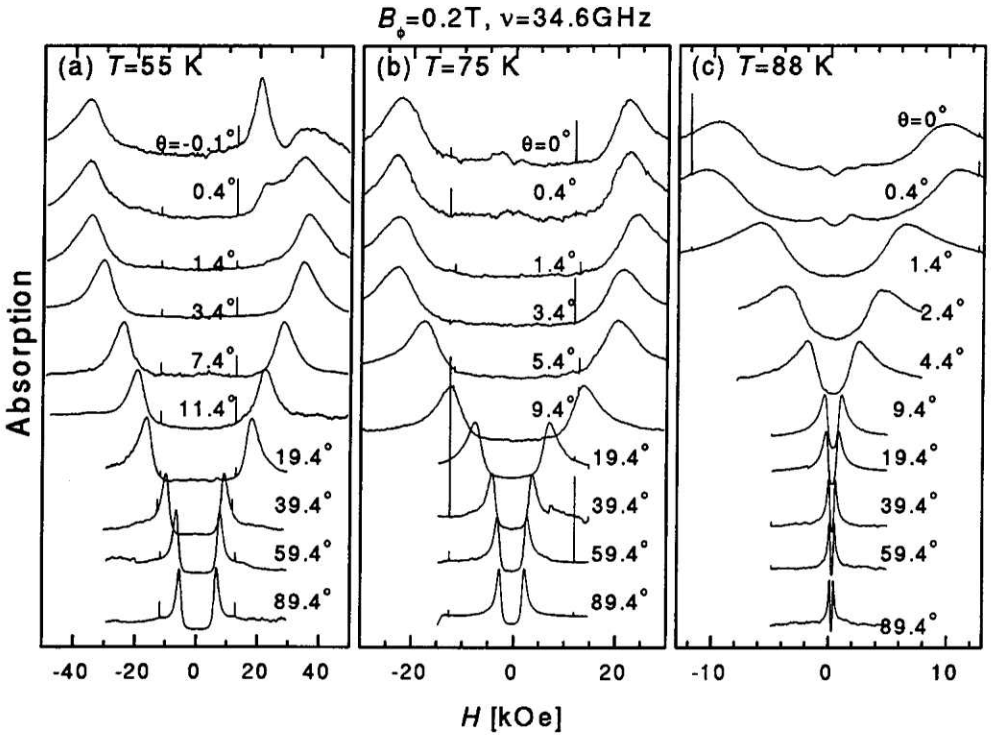


Figure 5.4: Angular dependence of the resonance in a dilutely irradiated ($B_\phi$ = 0.2 T) BSCCO single crystal at (a) 55 K, (b) 75 K, and (c) 88 K. The shifts of the resonance field with reducing field to $\boldsymbol{H} \parallel ab$ saturate in wider angle than that for the one of pristine sample. (Fig. 5.3). Additional resonance is observed in sufficiently small $\theta$ at low temperatures.

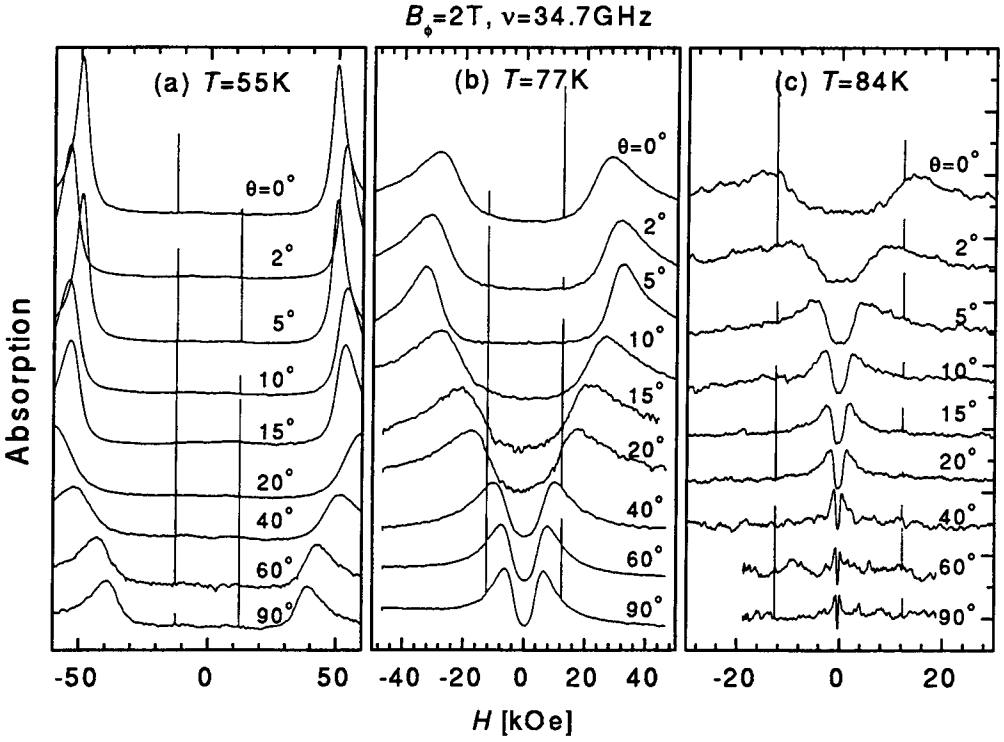


Figure 5.5: Angular dependence of the resonance for Sample F ($B_\phi = 2$ T) for various $\theta$ at (a) 55 K, (b) 77 K, and (c) 84 K. The anomalous hysteretic behavior at $\theta \sim 0$ found in the sample C and D was not observed in this sample.

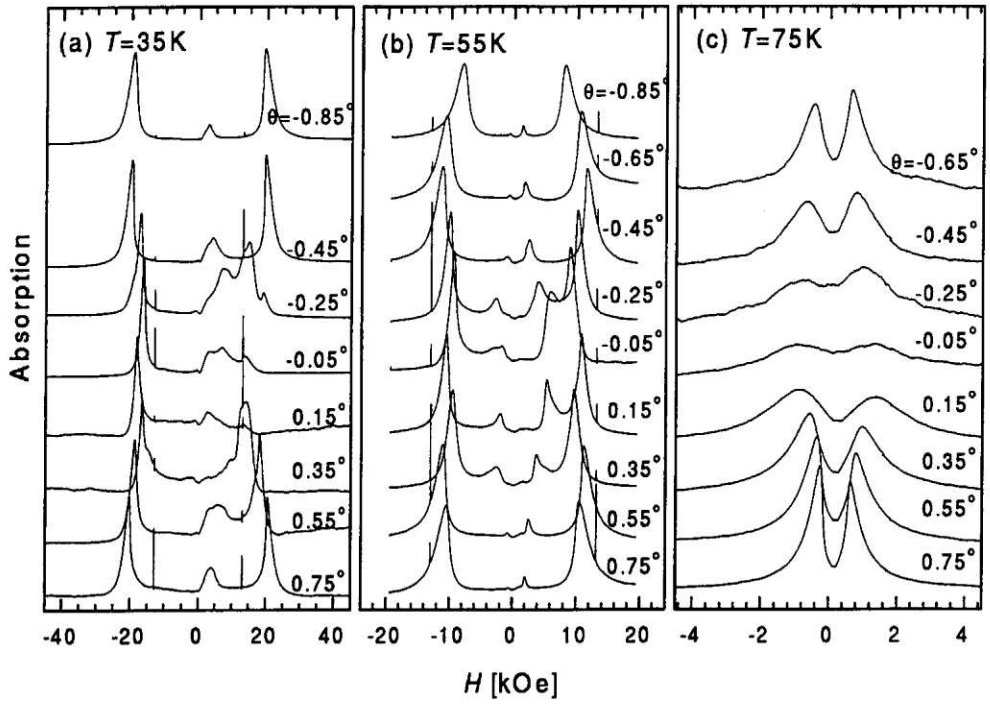


Figure 5.6: Angular dependence of the resonance lines in the very vicinity of parallel field $|\theta| < 1°$ at (a) 35 K, (b) 55 K, and (c) 75 K. In (a), utterly different behavior for decreasing ($H < 0$) and increasing ($H > 0$) field was observed. The line for decreasing field behaves systematic, while the one for increasing field is not systematic. In (b), an additional resonance is observed clearly in the lower field and becomes sharper than at 35 K. The main resonance is almost symmetric with respect to $H = 0$ for all $\theta$ but the additional one is not. At 75K (c), only one line is seen and the broadening becomes remarkable at angles very close to the $ab$ plane.

the higher dose sample. It should be stressed that in the highest dose sample $B_\phi = 2\,\mathrm{T}$ (Sample F) the resonance line becomes surprisingly sharp and larger at low temperatures and low angles (see Fig 5.5(a)).

### 5.4.2 Temperature dependence of the resonance

The temperature dependence of the resonance for the three samples in a perpendicular and a parallel magnetic fields is shown in Figs. 5.7, 5.8, and 5.9. In the perpendicular field ($\boldsymbol{H} \parallel c$), as shown in panels (a) of Figs. 5.7, 5.8, and 5.9 only symmetric resonance lines with little hysteresis (for field increasing and decreasing) are observed in the whole temperature region below $T_c$. The resonance fields decrease monotonically with increasing temperature and reach zero just at $T_c$ for the pristine sample C. However, this is not the same for the irradiated sample (D and F). The resonance field shows a sharp drop near $T^* \sim 80\,\mathrm{K}$ in the irradiated sample irrespective of the quantity of doses. Above $T^*$ the resonance line has a similar temperature dependence as the pristine one.

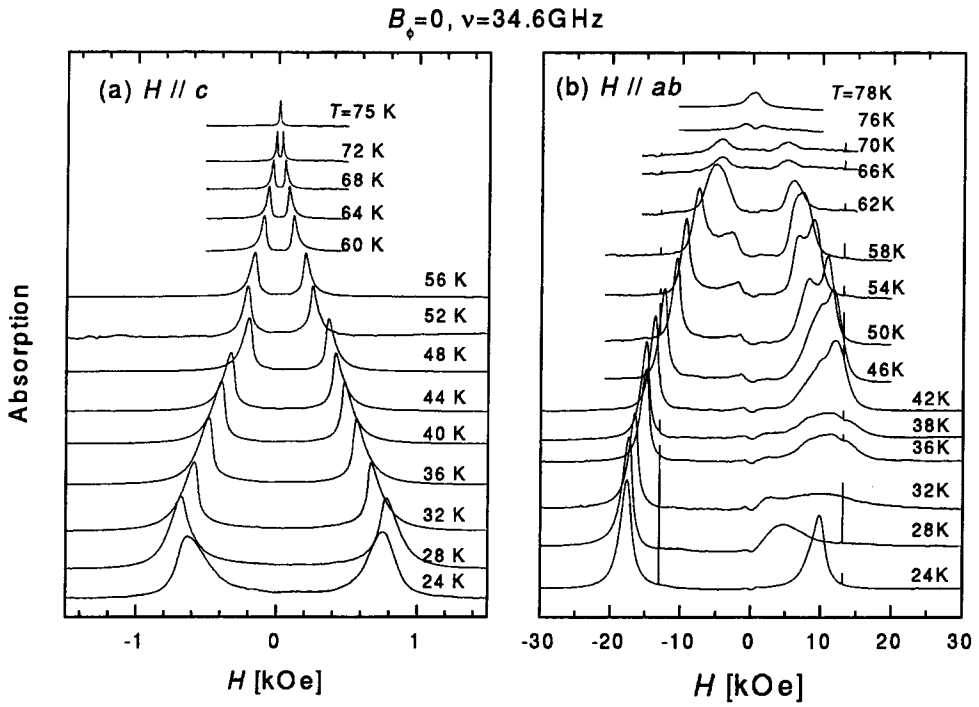


Figure 5.7: Temperature dependence of the resonance line of Sample C (pristine) in (a) perpendicular and (b) parallel magnetic fields. It is noted that the vertical separations between the data are taken so as to be proportional to the intervals of the temperatures. (a) When the external field is applied parallel to the $c$ axis ($\boldsymbol{H} \parallel c$), only a sharp and symmetric resonance line appears throughout the entire temperature range, and the resonance field decreases monotonically as the temperature increases. (b) When the external field is applied to the $ab$ plane ($\boldsymbol{H} \parallel ab$), a complicated feature can be seen at low temperatures below 66 K. Multiple resonance are observed with hysteresis to the magnetic field sweeping direction. At sufficiently low temperatures below 25 K, the additional resonance disappears.

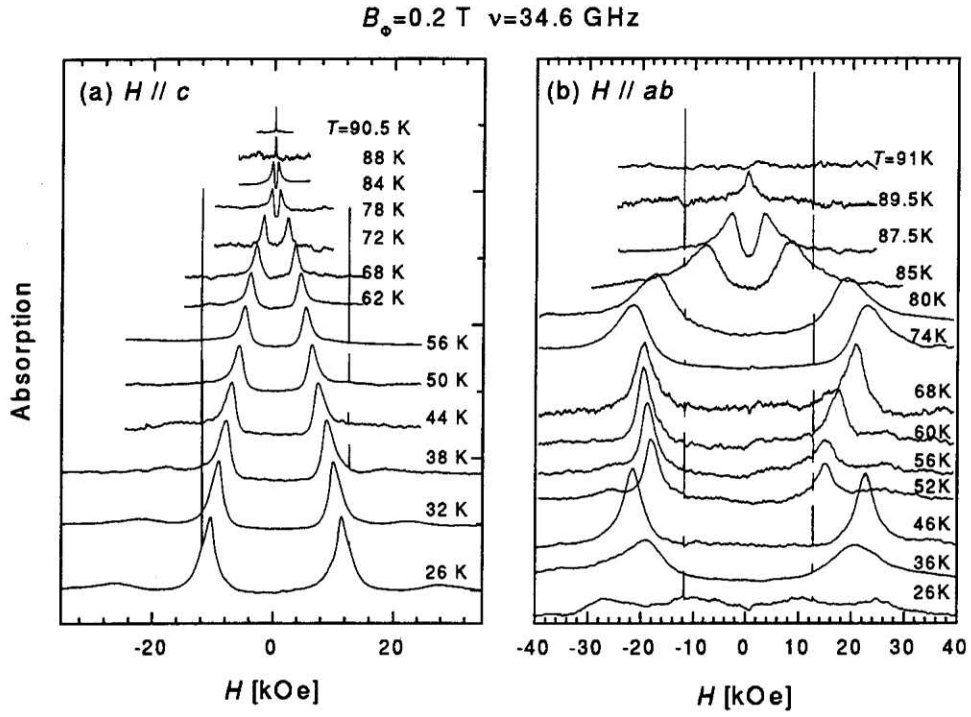


Figure 5.8: Temperature dependence of the resonance curve of Sample D ($B_\phi = 0.2$ T) in (a) perpendicular and (b) parallel magnetic fields to the *ab* plane. (a) Similar to the case for the pristine sample, the resonance field decreases steadily with increasing temperature. (b) Below $T^* \sim 80$ K, An anomalous behavior that was not seen in the pristine sample is observed. The temperature dependence shows an oscillatory behavior with hysteresis At high temperature, the hysteresis disappears and the line is broaden similarly to Fig. 5.7(b).

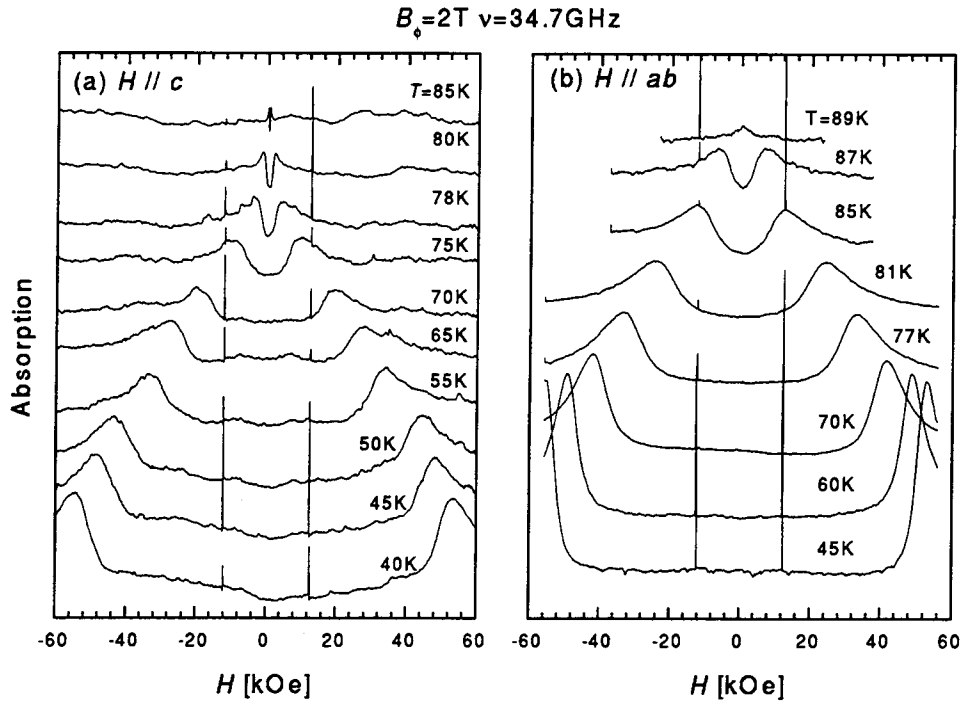


Figure 5.9: Temperature dependence of the resonance lines of Sample F ($B_\phi = 2$ T) in (a) perpendicular and (b) parallel fields. (a) Also in this sample, the resonance field decreases monotonically as the temperature increases. (b) An anomalous hysteresis was not observed in this sample. However, the broadening of the line in the higher temperature region is also observed, which is common feature in all samples.

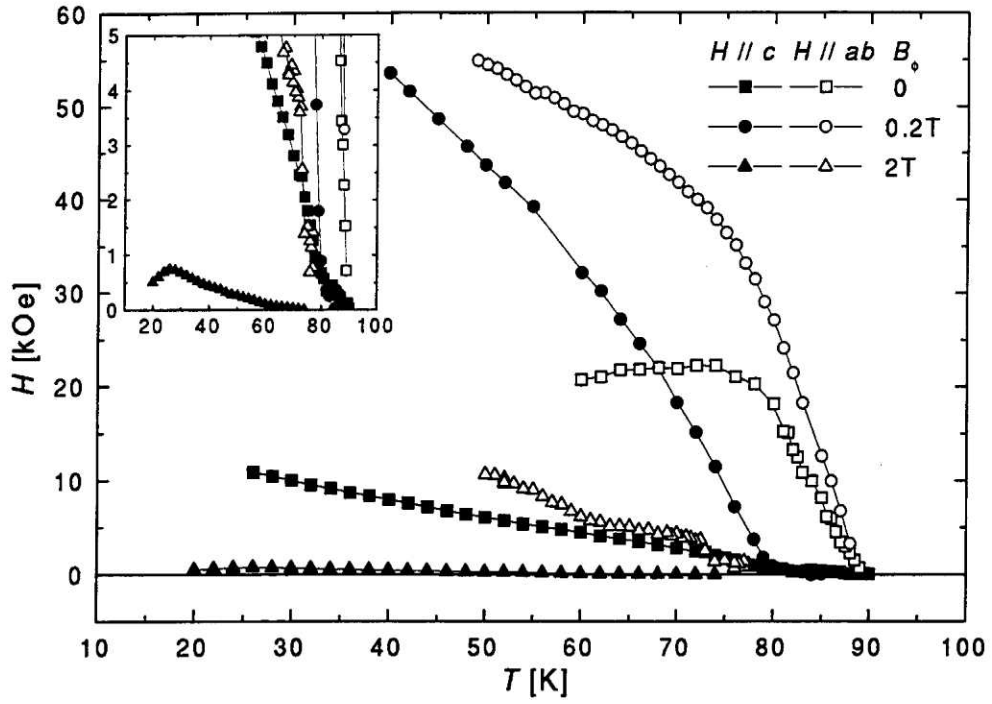


Figure 5.10: Temperature dependence of the resonance field for all samples in perpendicular (solid symbols) and parallel (open symbols) fields to the *ab* plane. Only the main resonance line is plotted and the data in the anomalous hysteretic temperature regions ($T < 50$ and 60 K for Sample D and F, respectively) are omitted to aviod complication. The inset shows the enlargement at low field resion of $H \leq 5$ kOe. Although the temperature dependence of the pristine sample is concave in the whole temperature range, the resonance fields of the irradiated samples in perpendicular fields have a convex temperature dependence in low temperature region, and drop to enough small value at $T^* \sim 80$ K. Subsequently, the temperature dependence shows concave feature in high temperatures.

The resonance line has a complicated hysteretic behavior, which also has strong temperature dependence as seen in Figs. 5.7(b) and 5.8(b). For Sample C ($B_\phi = 0$), the line which appears in the negative (decreasing) field is always observed the entire temperature range, but the one in the positive (increasing) field shows an anomalous temperature dependence. A symmetric and sharp line is observed at the lowest temperature of 24 K. As the temperature increases, the line once shifts to the lower field side and becomes broadened. With further increasing temperature, multiple peaks subsequently emerge, and the resonance line becomes approximately symmetric with $H =$ at further higher temperature region. For the sample D ($B_\phi = 0.2$ T), the abnormal hysteresis which is the different from the the pristine sample is observed. The resonance line in the decreasing field shows an anomalous temperature dependence similar to the one in the increasing field. However, in Sample F ($B_\phi = 2$ T), this anomaly is not found in all temperature range although the data below 45 K are not measured. It is remarked that the lineshapes in the high temperature range ($T/T_c > 0.8$) are common for all samples regardless of the density of defects. The temperature dependence of the resonance field for all samples in perpendicular and parallel fields are plotted in Fig. 5.10.

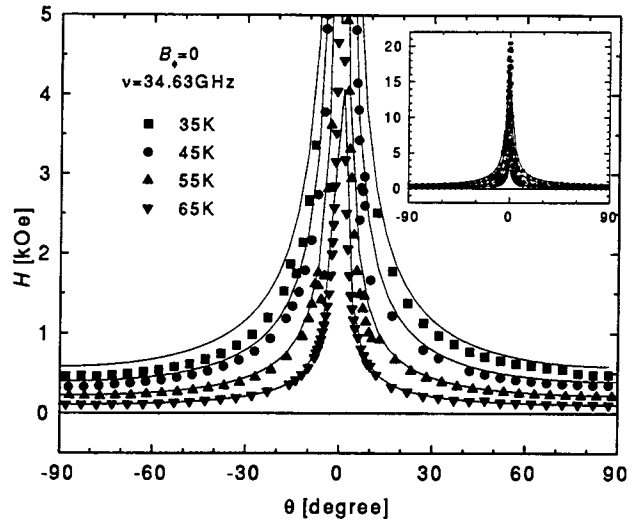


Figure 5.11: Angular dependence of the resonance field of Sample C ($B_\phi = 0$). The solid symbols indicate the experimental data and the solid line are the fitting results by Eq. (5.9). The inset shows the overall feature. The resonance line has a sharp peak in the vicinity of $\theta \sim 0$.

## 5.5 Discussion

### 5.5.1 Plasma resonance in perpendicular and oblique fields

The observed resonance fields as functions of $\theta$ and $T$ for Samples C, D, and F are plotted in Figs. 5.11, 5.12, and 5.13, respectively. Here, the resonance fields are obtained by averaging two values of the magnetic field where the resonance curves make peaks with increasing and decreasing fields as long as the curves are symmetric with respect to $H = 0$. In the pristine sample C, as shown in Fig. 5.11, the resonance fields shows a sharp increase of the resonance field near the $ab$ plane for the whole temperature region (see also the inset of Fig. 5.11). On the other hand, the angular dependence of Sample F ($B_\phi = 2$ T) indicates different features in comparison with the one for the pristine sample (Fig. 5.13). At the highest temperature of 84 K, the angular dependence of the resonance field shows a sharp peak at $\theta = 0$ similar to the one for the pristine sample. As the temperature is decreased the width of the peak becomes wider and wider and a double dip emerges around $\boldsymbol{H} \parallel ab$. This dip structure can be regarded as the lock-in transitions described in Sec. 5.2.2 and further discussed later. In Sample D with an intermediate dose of $B_\phi = 0.2$ T, the observed angular dependence has an intermediate feature between sample C and F.

We first discuss the angular dependence observed in the pristine sample. As described in Sec. 2.4.4, Josephson plasma frequency in the presence of magnetic field is written as

$$\omega_p(H,T) = \omega_p(0,T)\langle\cos\varphi_{\ell,\ell+1}\rangle^{1/2}, \tag{5.5}$$

where $\langle\cos\varphi_{\ell,\ell+1}\rangle$ denotes the thermal and disorder average of the cosine of the gauge invariant phase difference between $\ell$ and $\ell+1$ th layers $\varphi_{\ell,\ell+1}$ given by Eq. (2.72). Assuming that $\varphi_{\ell,\ell+1}$ is only affected by the density of pancake vortices, the perpendicular component of the external field $H_\perp \equiv H\sin\theta$ should be taken into account. Figure 5.14 displays the

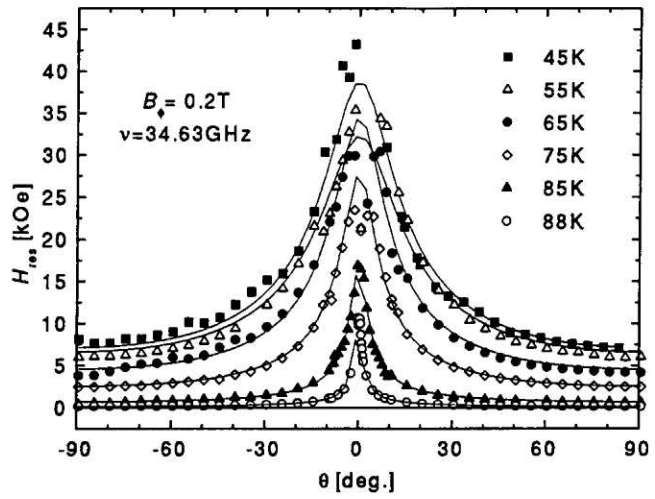


Figure 5.12: Angular dependence of the resonance field of Sample D ($B_\phi = 0.2$ T). The solid symbols indicate experimental data and the solid lines are the fitted results by Eq. (5.9). The resonance line has a peak as a function of angle at $\boldsymbol{H} \parallel ab$ with a wider than that of the pristine sample.

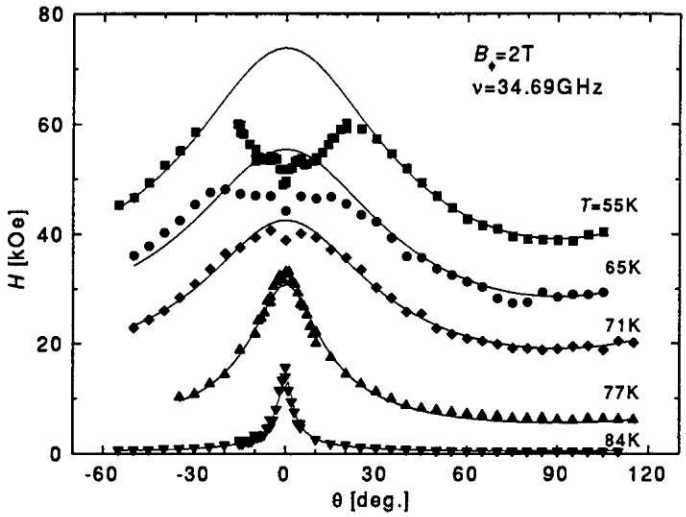


Figure 5.13: Angular dependence of the resonance field of Sample F ($B_\phi = 2$) T. The symbols represent experimental data points which are connected by the line obtained by fitting. At the lowest temperature of 55 K, the angular dependence clearly has a double dip structure.

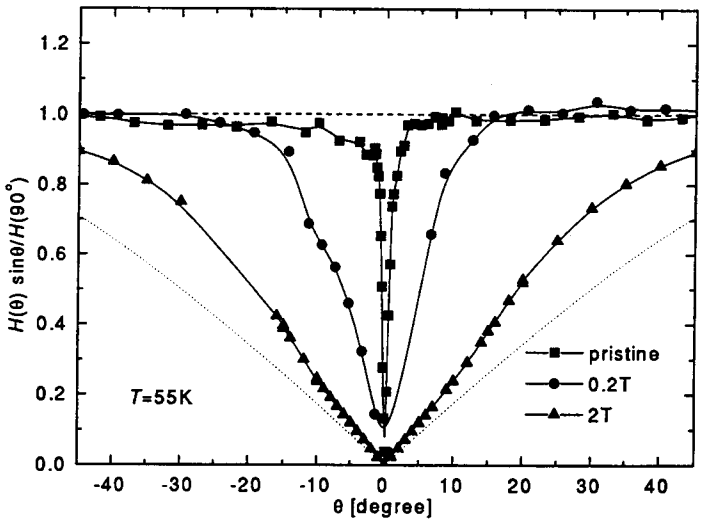


Figure 5.14: Angular dependence of the resonance field normalized by the perpendicular component of the applied field and the resonance field in perpendicular fields. The square, circle, and triangle symbols indicate for the data of Samples C ($B_\phi = 0$), D ($B_\phi = 0.2$ T), and F ($B_\phi = 2$ T), respectively. In all cases the normalized resonance field has a dip at $\boldsymbol{H} \parallel ab$. The width of the dip is sharpest for Sample C ($B_\phi = 0$) and widest for Sample F ($B_\phi = 2$ T). A broken and a dotted lines mean that the angular dependence is perfectly two-dimensional (resonance fields diverge at $\theta = 0$) and perfectly three dimensional (no angular dependence is seen), respectively. The solid lines are guides for the eye.

resonance fields which are normalized by $H_\perp$ and the resonance field in the perpendicular fields $H(90°)$ for the pristine and irradiated samples. The data of the pristine sample are well normalized except for the very vicinity of $\theta = 0$. This behavior is already reported in an earlier study of the Josephson plasma resonance [3]. Recently Koshlev [5] gives a theoretical approach based on the high-temperature expansion. He described the angular dependence of the plasma frequency in the superconducting fluctuation state as

$$\omega_p^2 = \frac{2\pi d\phi_0 j_{\rm cr}^2}{\epsilon H_\perp k_{\rm B} T} \exp\Big(-\frac{\pi d^2 H_\parallel^2}{H_\perp \phi_0}\Big), \tag{5.6}$$

where $j_{\rm cr}$ is the Josephson critical current in zero field and $H_\parallel$ is the parallel component of the magnetic field. This equation can be reduced to

$$\omega_p^2 \propto 1/TH_\perp \tag{5.7}$$

at higher angles because $\phi_0/\pi d^2 \sim 100$ T. This accounts for our experiment well.

Next we notice the data of the two irradiated samples in Fig. 5.14. The angular dependence of Sample D does not obey the sine-law within $\pm 20°$ from the plane. Moreover in Sample F, it departs from $H \sin\theta$ near the $c$ axis. This can be understood by the enhancement of interlayer coherence due to the existence of columnar defects which pierce $CuO_2$ layers. In other words, the columnar defects suppress the two-dimensionality that a pristine matrial possesses and the enhanced interlayer coherence causes the behavior which is closer to that of the three dimensional system. In Fig. 5.13, we have shown that the temperature

dependence of the resonance line behaves as more 3D fashion at low temperatures whereas it behaves as more 2D fashion at high temperatures. We can easily explain this phenomena as follows; the vortices confined strongly in the columnar defects in low temperatures are released because of the thermal fluctuation which exceeds the pinning force. As a result, the vortex system with columnar defects behaves similar to the pristine one in a high temperature limit. Although there has been experimental data of the Josephson plasma resonance in BSCCO with several doses of heavy ion irradiation given by some authors [11, 12], no quantitative analysis has been made yet.

According to the anisotropic Ginzburg-Landau regime, the angular dependence of the physical parameters such as the critical field $H_c(\theta)$ is given by the simple ellipsoidal form:

$$\left(\frac{H_c(\theta)\sin\theta}{H_{c\perp}}\right)^2 + \left(\frac{H_c(\theta)\cos\theta}{H_{c\parallel}}\right)^2 = 1, \tag{5.8}$$

where $H_{c\perp}$ and $H_{c\parallel}$ are the critical fields perpendicular and parallel to the $CuO_2$ plane, respectively. By analogy of this expression, we introduce a phenomenological equation for the angular dependence of the Josephson plasma resonance as

$$H(\theta) = \frac{H(90°)}{\sqrt{\sin^2\theta + \alpha^{-2}\cos^2\theta}}, \tag{5.9}$$

where $H(90°)$ is the resonance field in a perpendicular field and $\alpha$ is a new parameter which reflects the anisotropy in the presence of vortices in the superconducting state. In the case of $\alpha \to \infty$, the behavior as a function of $\theta$ is completely two dimensional, whereas the resonance field is independent of $\theta$ if $\alpha$ is unity, The solid lines in Figs. 5.11, 5.12, and 5.13 are the fitted results derived by the least square method by taking $H(90°)$ and $\alpha$ as fitting parameters. All show excellent agreement with the experimental data except the region near *ab* plane where the dip structure is observed.

Let us consider the behavior of $\alpha$ as a function of temperature. The obtained $\alpha$ and $1/\alpha$ values are plotted in Fig. 5.15 at various temperatures where the angular dependence has been measured. The resonance fields in $\boldsymbol{H} \parallel c$ were also plotted as a function of the temperature. The data of the sample with $B_\phi = 0.5\,\mathrm{T}$ are added (not presented in this place). This figure clearly indicate that the parameter $\alpha$ at lower temperatures considerably differs from the one at higher temperatures. Looking at the diagram, the temperatures where $\alpha$ begins to increase drastically correspond where the temperature dependence of the resonance field in a perpendicular field ($\boldsymbol{H} \parallel c$) for each sample makes a slight cusp.

The concave cusp at $T^*$ of the temperature dependence of the resonance field of irradiated BSCCO in perpendicular fields just below $T_c$ is previously reported by Kosugi *et al.* [12] and Sato *et al.* [13], and they pointed out this behavior is due to the coupling-decoupling transition of vortices between the layers. Also in our experiments, the angular dependence of the resonance fields of the irradiated samples above $T^*$ is almost identical to the one of the pristine sample which obeys the scaling law — in our phenomenological equation (5.9), $1/\alpha$ is reduced to zero.

### 5.5.2 Plasma resonance in slightly tilted fields

In a slightly tilted magnetic field from the plane, the perpendicular component of the field is still so small that there is no pancake exciting in the $CuO_2$ plane. In this situation,

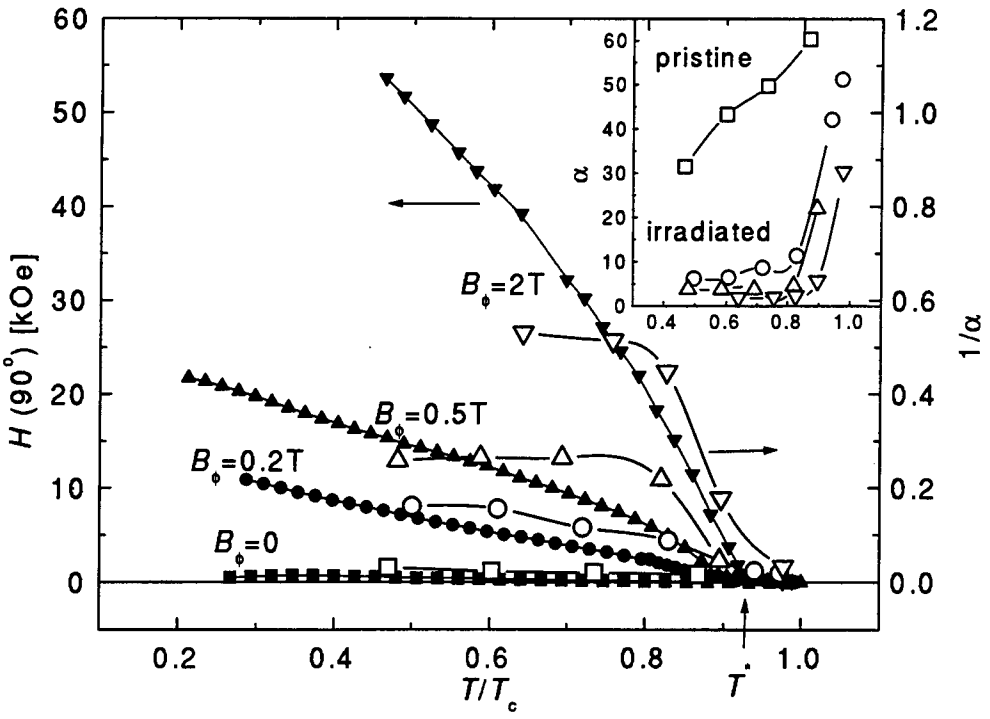


Figure 5.15: Temperature dependence of the resonance field for $\boldsymbol{H} \parallel c$ (left ordinate). Temperature dependence of inverse of the effective anisotropy parameter $1/\alpha$ is also plotted by open symbols (right ordinate). The inset indicates the temperature dependence of $\alpha$, and the symbols are corresponding to those in main panel. The drastic decrases of $1/\alpha$ (increase of $\alpha$) are observed at the temperatures where the temperature dependence of $H(90°)$ makes a slight cusp at $T/T_c \sim 0.8$. The solid lines are drawn to guide for the eyes.

the Josephson vortices are considered to play an important role in the plasma resonance, although no detailed theoretical work in this case is available. Experimentally, it is rather impossible to set magnetic field direction exactly parallel to the *ab* plane, so that in a practical sense misorientation of the field direction always results in the present slightly tilted field condition. Moreover, the single crystal always has a mosaic spread, which give rise to the effective misorientation of the field direction. The experimental accuracy of the field orientation for our case is less than $10^{-3}$ degree in the goniometer and the mosaic spread of the sample is as small as 0.03 degree in our single crystals.

As shown in the preceding section (Figs. 5.11, 5.12, and 5.13), the Josephson plasma resonance continues from sufficiently larger angles to the *ab* plane, although the angular dependence begins to deviate from a certain angle depending upon the irradiation doses. This continuous mode of the Josephson plasma resonance may be explained by the trapped pancake vortices due possibly to the misorienaion effect of the magnetic field. This vortex density should depend upon the field history, resulting in the hysteretic behavior in magnetic field directions. However, the experimental results cannot be explained by ordinary magnetic hysteresis phenomenon, because the resonance takes place in the higher field when the field is decreased, whereas in the lower field when field is increased as shown in Fig. 5.16. This is opposite from what one can expect from conventional magnetic hysteretic behavior.

Tsui *et al.* have recently reported a similar result in a parallel field orientation [8]. They interpreted this hysteretic behavior by considering a model called "camel humps," in which the effective lower perpendicular critical field $H^*$ (see Eq. (5.4)) is considered as a function of temperature as shown in Fig. 5.17. Although their interpretation seems to be accountable for the part of experimental results we have observed, the following points are left to be answered: First, in the camel humps model, it is impossible to explain multiple resonance, appearing differently in a sweeping-up and sweeping-down magnetic field. Second, the observed hysteresis by us for lower fields gives an opposite behavior for the field sweeping-up and sweeping-down. This is even contradictory against the results reported by Tsui *et al.*, and cannot be explained by their camel humps model.

It appears that as seen in Fig. 5.6 in the pristine sample the behavior of the resonance changes very drastically as a function of the angle within $\pm 0.5°$ in the *ab* plane. Such a sharp angular dependence cannot be expected by the simple hysteretic magnetization behavior and has to be considered the vortex state in a parallel magnetic field. In the anisotropic superconductor, the vortex configurations has been calculated theoretically using Lawrence-Doniach model. According to Bulaevskii *et al.* [26] the vortex configuration is the distorted hexagonal structure, which is elongated to the *ab* direction (in other word, compressed to the *c* direction) with a periodic arrangement of the empty vortex layers, when the applied magnetic field is smaller than the characteristic magnetic field of $H_0 \sim \phi_0/\gamma d^2$, where $\phi_0$ is the flux quantum, $\gamma$ is the anisotropic parameter, and $d$ is the interlayer spacing. When the magnetic field is higher than $H_1 \sim H_0/3$, all layers are completely filled by Josephson vortices, whereas in the field range $H_2 \sim H_0/8 < H < H_1$, every other layers are filled and the rest of the layers (half of the layers) are vacant. This sequential filling of the layers continues to happen as the field is lowered towards zero. The above situation is visualized in Fig. 5.18. For BSCCO, the physical parameters are well known to estimate the critical fields $H_1$, $H_2$, or so. Using $\gamma \sim 150$, $d = 15$ Å, $H_0 \simeq 6.1$ T, $H_1 \simeq 2$ T, and $H_2 \simeq 0.77$ T are obtained.

Although this is for the ideal case without having pinning effect at all, such sequential structural phases must have their vortex vibration modes, which can couple with the

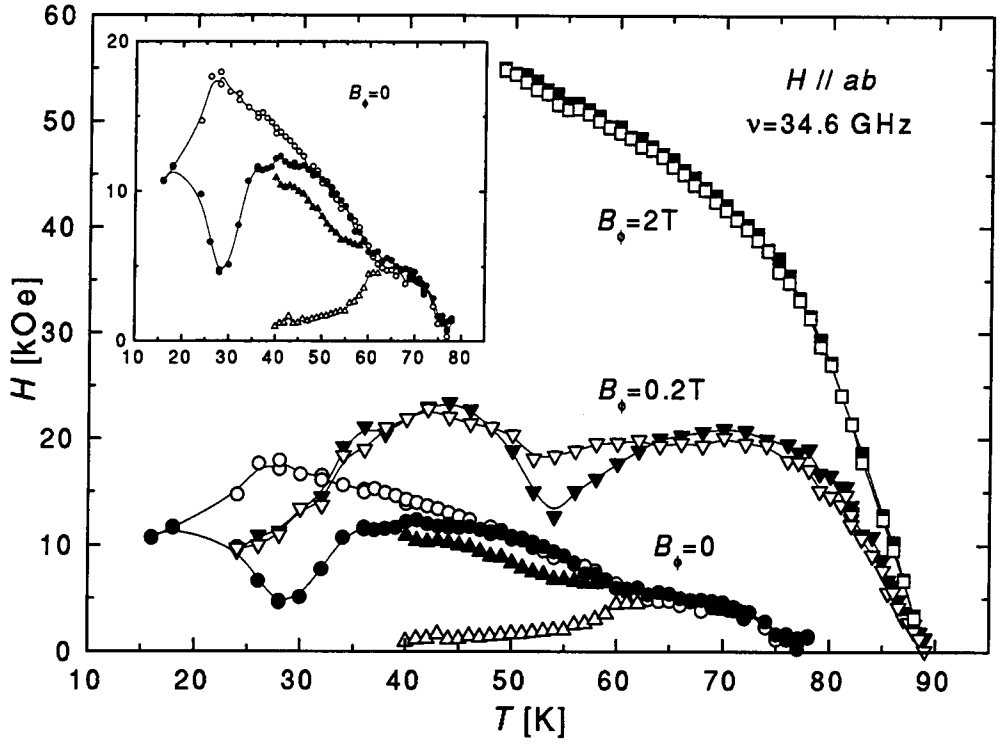


Figure 5.16: Temperature dependence of the resonance fields in $\boldsymbol{H} \parallel ab$ for Sample C (circles and triangles), Sample D (reversed triangles), and Sample F (squares). The solid (open) symbols indicate the resonance field with increasing (decreasing) field. The data of Sample C are extracted to the inset. Hysteretic behaviors appear in Samples C ($B_\phi = 0$) and D ($B_\phi = 0.5$ T) in finite ranges. The additional resonance in Sample C (triangle) has opposite response with the field increasing/decreasing. The two triangles are much separated at low temperature, but the one with increasing field may drastically decrease accompanied with the main resonance.

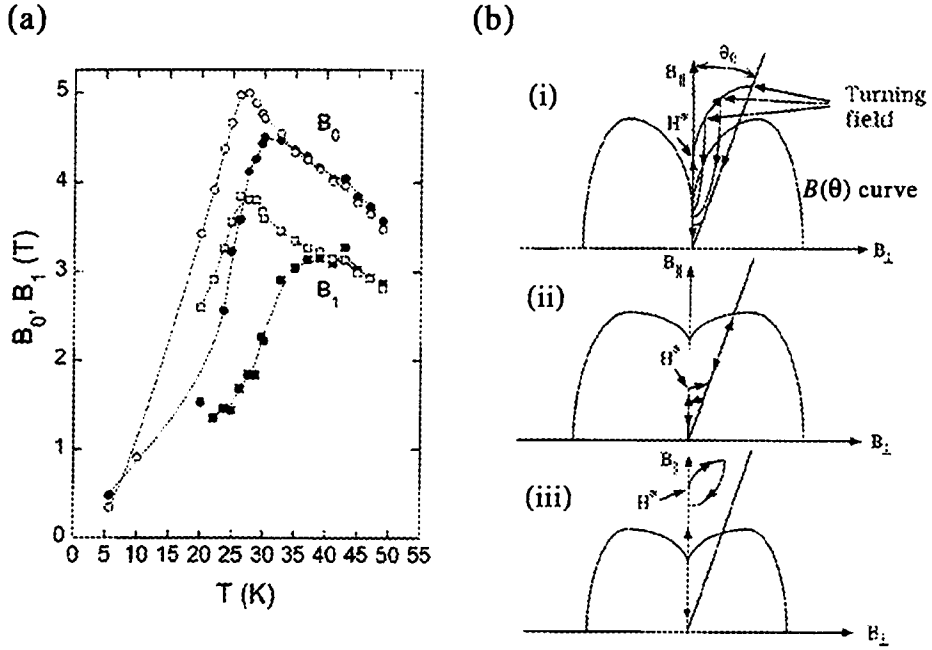


Figure 5.17: (a) Temperature dependence observed by Tsui *et al.* and (b) camel humps [8]. In (a), solid (open) symbols are data with increasing (decreasing) field. Two hysteretic resonances with same character are observed. Behavior of the lower resonance is strikingly different from our results. (b) shows hysteretic behavior in the $B_y$-$B_z$ plane for different temperature ranges of (i) hysteretic temperature, (ii) higher temperature, and (iii) lower temperature. The arrow lines represent the traces of magnetization $\boldsymbol{B}$. When the external magnetic field $\boldsymbol{H}$ is increased from zero, $\boldsymbol{B}$ traces on $B_{||}$ axis in the case of $H_\perp \leq H^*$ because of the lock-in transition. If $H_\perp > H^*$, $\boldsymbol{B}$ leaves from the $B_{||}$ axis and turns to be parallel to $\boldsymbol{H}$, and traces different path with making a large hysteresis when $\boldsymbol{H}$ is decreased. When the hystereric loop cross the $B(\theta)$ curve, the hysteretic resonance occurs as seen in (i). In higer (lower) temperature range, $H^*$ is so small (large) that the traces cross the curve at a point, therefore the hysteresis does not appear

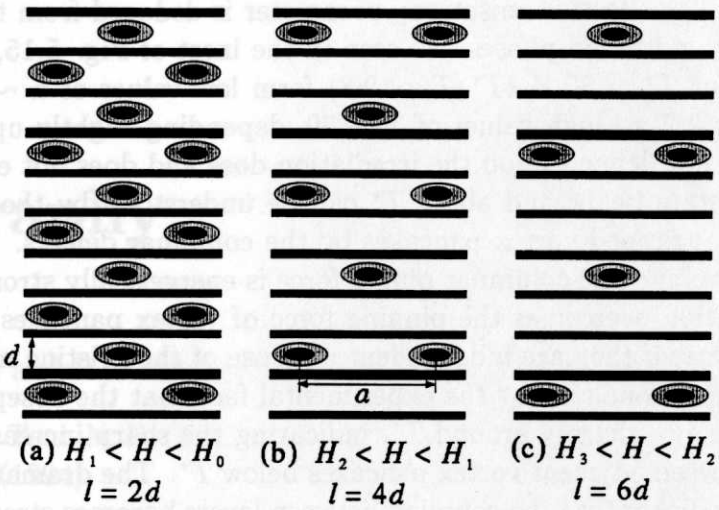


Figure 5.18: Sequential filling of Josephson vortices as a function of the external field. $l$ and $a$ denote the period of the Josephson vortex lattice along the $c$ axis and the $ab$ plane, respectively. In each magnetic field range, $a$ is varied with respect to the external field while $l$ is not.

Josephson plasma mode directly. This idea has been examined by the computer simulation technique by Takahashi [27]. He performed examination in the case of $H_3 < H < H_2$ for BSCCO and found the low lying mode, which is phonon-like mode and strongly couple with the Josephson plasma mode. It is interesting that there are two modes at $k = 0$ below the plasma resonance excitation frequency $\omega_p$ for both transverse and longitudinal propagation modes. As seen in Fig. 5.6(a), for example, one can find two additional resonance lines very close to the $ab$ plane only. It is speculated that those additional lines observed experimentally may not be caused by the Josephson plasma resonance mode due to pancakes observed at high temperatures, but may be related with the new modes as mentioned above. It is highly intriguing and necessary to carry out further experiments to this issue.

## 5.6 Conclusions

In this chapter, the Josephson plasma resonance in a pristine and heavy ion irradiated BSCCO single crystals was described as functions of external field direction $\theta$ and temperature $T$. A qualitative and a systematic understanding was shown by introducing the effective anisotropy parameter $\alpha$. The possible explanation observed only for $\boldsymbol{H} \parallel ab$ was argued based on the recent theoretical calculations [27].

In a pristine sample, the angular dependence of the resonance fields is shown to be described well by the two dimensional behavior. The angular dependence of the Josephson plasma resonance was found to be enhanced as the number of columnar defects are increased below $T^* \sim 80$ K. The scaling analysis was applied to account for the angular dependence except for the region close to the $ab$ plane. The angle region where the scaling law cannot be applied is different, and depending on the irradiation dose. This angle region, for the pristine sample, is only within $\pm 1°$ but for the irradiated samples it is about $\pm 5°$ for $B_\phi = 0.2$ T, and

$\pm 20°$ for $B_\phi = 2$ T. The effective anisotropy parameter is deduced from the scaling analysis in both solid (glass) and liquid phases. As seen in the inset of Fig. 5.15, the $\alpha$ values have sharp jumps at about $T^* \sim 80$ K ($T^*/T_c \simeq 0.8$) form low values of $\alpha \sim 6$ for $B_\phi = 0.2$ T and $\alpha \sim 2$ for $B_\phi = 2$ T to high values of 30 – 50, depending slightly upon the irradiation dose. Since $T^*$ dose not depend upon the irradiation dose and does not exist in the pristine sample, the vortex state below and above $T^*$ can be understood by the distinct difference of the number of the trapped vortex pancakes by the columnar defects. Below $T^*$, thermal agitation is ineffective and the columnar pining force is energetically stronger. On the other hand, thermal agitation overcomes the pinning force of vortex pancakes above $T^*$, so that the pancakes behave as if they are independent as those of the pristine material.

This view can be rationalized by the experimental fact that the Josephson plasma resonance field begins to rise sharply around $T^*$, indicating the sharp increase of the interlayer phase coherence between adjacent vortex pancakes below $T^*$. The dramatic reduction of the anisotropy value $\alpha$ indicate that the coupling between layers becomes stronger, and therefore it may suggest strongly some sort of ordered phase below $T^*$. This is also true for the pristine material, where the sharp first order vortex lattice melting transition exhibits below $T_m$. From magnetization measurements [28], the effective anisotropy value for the vortex lattice phase is as small as $\sim 10$, whereas it is 150 – 200 above the melting transition. Therefore, it is well understood that the scaling approach over wide temperature region is useful no matter what kind of the vortex phases are. This is the universal concept to deal with the vortex state in high temperature superconductors.

In the very vicinity of the *ab* plane, where a sharp dip feature is observed, the lock-in transition may occur. The vortex configuration in this state was argued according to the previous work based on the Lawrence-Doniach model, which implies collective phase transitions at $H_1$, $H_2$, $H_3$, ... corresponding to the vortex configurations shown in Fig. 5.18. The values for $H_1$, $H_2$, $H_3$, ... are in the range where our experiment was carried out. Therefore, it is speculated that the additional resonance line observed only in a very narrow angle region in the pristine sample and the sample with irradiation dose of 0.2 T may be due to the resonance coupled with such peculiar vortex phases as predicted by a computer simulation [27]. If this is the case, these resonances have entirely different origin from the resonance in $\boldsymbol{H} \parallel c$ and would be new resonance modes. It is very interesting to resolve this question.

# Bibliography


[1] J. G. Bednorz and K. A. Müller, Z. Phys. B **64**, 189 (1986).

[2] Ophelia K. C. Tsui, N. P. Ong, Y. Matsuda, Y. F. Yan, and J. B. Perterson, Phys. Rev. Lett. **73**, 724 (1994).

[3] Y. Matsuda, M. B. Gaifullin, K. Kumagai, K. Kadowaki, and T. Mochiku, Phys. Rev. Lett. **75**, 4512 (1995).

[4] L. N. Bulaevskii, V. L. Pokrovsky, and M. P. Maley, Phys. Rev. Lett. **76**, 1719 (1996).

[5] A. E. Koshelev, Phys. Rev. Lett. **77**, 3901 (1996).

[6] O. K. C. Tsui, N. P. Ong, and J. B. Peterson, Phys. Rev. Lett. **76**, 819 (1996).

[7] Y. Matsuda, M. B. Gaifullin, K. Kumagai, K. Kadowaki,T. Mochiku, and K. Hirata, Phys. Rev. B **55**, 8685 (1997).

[8] O. K. C. Tsui, S. P. Bayrakel, N. P. Ong, K. Kisio, and S. Watauchi, Phys. Rev. B **56**, 2948 (1997).

[9] L. N. Bulaevskii, M. Maley, H. Safar, and D. Dominguez, Phys. Rev. B **53**, 6634 (1996).

[10] L. N. Bulaevskii, D. Dominguez, M. Maley, and A. R. Bishop, Phys. Rev. B **55**, 8482 (1997).

[11] T. Hanaguri, Y. Tsuchiya, S. Sakamoto, and A. Maeda Phys. Rev. Lett. **78**, 3177 (1997)

[12] M. Kosugi, Y. Matsuda, M. B. Gaifullin, L. N. Bulaevskii, N. Chikumoto, M. Konczykowski, J. Shimoyama, K. Kishio, K. Hirata, and K. Kumagai, Phys. Rev. Lett. **79**, 3763 (1997).

[13] M. Sato, T. Shibauchi, S. Ooi, T. Tamegai, and M. Konczykowski, Phys. Rev. Lett. **79**, 3759 (1997).

[14] E. Zeldov, D. Majer, M. Koncykowskii, V. B. Geshkenbein, V. M. Vinokur and H. Strikman, Nature **375**, 373 (1995).

[15] C. Kittel "*Introduction to Solid State Physics*," seventh edition, John Wiley & Sons, 1996.

[16] H. A. Leupold and H.A. Boorse, Phys. Rev. **134A**, 1322 (1964).
T. McConville and B. Serin, Phys. Rev. **140A**, 1169 (1965).

[17] C. Meingast, R. Ahrens, B, Blank, H. Burkle, B. Rudolf, and H. Wuhl, Physca C **173**, 309 (1991).
S. E. Inderhees, M. B. Salamon, J. P. Rice, and D. M. Ginsberg, Phys. Rev. B **47**, 1053 (1993).

[18] A. Junod, E. Bonjour, R. Calemczuk, J. Y. Muller, G. Triscone, and J. C. Vallier, Physica C **221**, 304 (1993).

[19] T. Tsuneto, J. Phys. Soc. Jpn. **57**, 3499 (1988).

[20] M. Tinkham, *Introduction to Superconductivity,* second edition, McGraw-Hill, 1996.

[21] L. J. Champbell, M. M. Doria, and V. G. Kogan, Phys. Rev. B **38**, 2439 (1988).

[22] Sara L. Thiemann, X. Radovic, and V. G. Kogan, Phys. Rev. B **39**, 11 406 (1989).

[23] John R. Clem, Phys. Rev. B **43**, 7837 (1991).

[24] A. E. Koshlev, Phys. Rev. B **48**, 1180 (1993).

[25] D. Feinberg and C. Villard, Phys. Rev. Lett. **65**, 919 (1990).

[26] L. N. Bulaevskii, M. Ledvji, and V. G. Kogan, Phys. Rev. B **46**, 366 (1992).

[27] S. Takahashi, private cominucation.

[28] K. Kadowaki and K. Kimura, to be published in Phys. Rev. B.

# Chapter 6

# Summary

Josephson plasma phenomena in high temperature superconductors are described in the preceding chapters, which have been carried out in the course of my Ph.D. graduate study. This subject has been brought up at the beginning of my graduate study timely and has attracted much attention in the part a few years, especially after the discovery of microwave absorptive phenomena by Tsui *et al.* in one of typical high temperature superconductor $Bi_2Sr_2CaCu_2O_{8+\delta}$. Although they could not fully disclose the origin of the absorption, however, their experimental observation certainly triggered and made an impulse to investigate this extraordinary phenomena further. What is described here in this thesis is merely the part of the experimental features and associated theoretical understanding of the phenomena, since the physics related to this phenomena is so deep and wide that may related problems from basic to applied subject will appear. Although the most fundamental nature of the Josephson plasma phenomena may be included in this study, much variety of phenomena such as microwave coherent emission, ultrafast switching, dynamic microwave filters, detectors at THz frequencies, etc. are not studied unfortunately and are waiting for experimental proofs. Some of those phenomena are related to the development of technologies at the microwave to infrared frequencies, so that this subject is widely open for the applied science and technology in near feature.

We begun this thesis with describing some historical development concerning the electromagnetic interactions with superconducting electrons. The full understanding of the superconductivity in electron systems has not been achieved until the fieldtheoretic understanding based on the broken symmetry concept in the gauge field was extremely successful in the field of elementary particle physics. We note this importance in this thesis.

In the first part of the thesis, plasma phenomena induced by the interaction with electromagnetic waves are summarized and further extended to the Josephson plasma. In the course of my Ph.D. study, we come up an important idea that strongly suggests the experimental distinction of the two independently existing Josephson plasma modes: one is the longitudinal mode and the other is the transverse mode. The longitudinal mode of plasma is known to be the Nambu-Goldstone mode, which is elementary excitations associated with the superconducting phase transitions due to the breaking of the gauge symmetry, and the transverse mode induces the transverse current flow, which causes Meisnner effect. Although such interpretation has been put forward in early sixties by Anderson, experimental separation of two modes has not been done until our experiments. This is partly become the experimental excitations of two mode separately was impossible in the conventional superconductors without having large anisotropy, which reduces the plasma frequencies and the

corresponding wavelength to the size comparable with the wave length of the electromagnetic wave in superconductors. This condition cannot be made in the electromagnetic wave at infrared or higher frequencies in conventional superconductors.

Here we have succeeded in performing clear distinctions of two mode experimentally and this is described in this thesis as a main contribution together with the detailed experimental techniques bared on the theoretical calculations. It is worthwhile noting that this achievement is another experimental proof that the concept of the broken symmetry can perfectly describe the nature of the electron system interacting with the electromagnetic fields. This understanding of superconductivity lead us to complete the theoretical framework describing the nature of electron systems interacting with electromagnetic waves. Finally, we fully understood the fundamental nature of superconductivity at this moment.

In the second part of this thesis we detail with the vortex state of high temperature superconductors by making use of Josephson plasma technique developed in the first part. Since this phenomena senses the superconducting phase difference between the Josephson coupled layers in highly anisotropic superconductors such as $Bi_2Sr_2CaCu_2O_{8+\delta}$, it gives a unique opportunity to understand the nature of layer coupling in this system. Many new vortex states, — the pancake state, the vortex glass state, Bragg glass state, superconducting fluctuation state, and etc.— which dose not exist in conventional superconductors, have been discovered in high $T_c$ superconductors. The unified understanding of these phases are the subject in this part of study.

We have studied, during my Ph.D. work, in particular, the effect of the columnar defects on the interlayer Josephson coupling. The samples studies here are the pristine one (as grown), and three heavy ion irradiated columnar defect samples with the equivalent flux density of $B_\phi = 0.2$, 0.5, 2 T.

We found a dramatic increase of pinning strength in the irradiated samples with columnar defects as previously known. This feature is directly proved by the Josephson plasma resonance to be induced by the increase of the phase coupling strength between superconducting layers below $T^* \approx 80$ K, i.e., increase of Josephson coupling. This is attributed to the thermal confinement of pancake vortices into columnar defects are considerably less significant. We have also studied angular dependence of the Josephson plasma resonance. We paid much attention to the angular behavior near the *ab* plane, where the resonance dramatically changes the character. We proposed the extended concept of the anisotropy parameter $\alpha$ to the problem and found a coherent description of the vortex state as functions of both temperature and angles in all samples by using the effective anisotropy parameter $\alpha$. This generalization of the anisotropy parameter can describe nicely the vortex state no matter what sort of vortex states are in the system. However, it was found that this description is violated and is not applicable to the region where the angle is closer to the *ab* plane than the critical angle, at which the generalized scaling theory dose not work anymore. Within the critical angle, we have to take into account the new effect of parallel component of magnetic fields by which Josephson vortices are created. In this situation, it is known that the Josephson vortices play an essential role for the Josephson plasma resonance. Some additional features such as multiple branches of resonance, the coupled mode of vortex motion to the plasma oscillations etc. are theoretically predicted. In the present study, however, we could not resolve much interesting features, although some anomalous behaviors reminiscent of some of those new phenomena which were predicted. Further studies beyond my Ph.D. thesis are needed in order to elucidate these fascinating phenomena related to the Josephson plasma resonance.

# Acknowledgments

This work has been performed at three laboratories, High Magnetic Field Laboratory of Osaka University, Kadowaki Laboratory at University of Tsukukba, and National Research Institute for Metals (NRIM). And quite many researchers engaged in this collabration.

First, I would like to express my gratitude to Professor Koichi Kindo at Research Center for Materials Science at Extreme Conditions (KYOKUGEN), who gave me a chance to carry out this research. Although he was not involved in this work directly, I was often helped by his advices concerning experimental techniques and attitudes toward physics during courses of my graduate education.

I would like to express my supecial thanks to Professor Kazuo Kadowaki in Institute of Materials Science at University of Tsukuba, for his continuous suggestion and instruction throughout this work, his guidance was indispensable for completing this thesis and is especially acknowledged. I also appreciate for his hospitality during my stays at Tsukuba.

I am indebted to Emeritus Professor Muneyuki Date at Osaka University (President of Advanced Research Center of JAERI at present), and Emeritus Professor Masashi Tachiki at NRIM, for their arrangements to carry out this cooperative research program smoothly.

I am grateful to Dr. Takashi Mochiku at NRIM, for preparing high quality BSCCO single crystals, and to Dr. Saburo Takahashi at Institute for Materials Research of Tohoku University, for his model calculation of the sample size dependence described in Chap. 4. Also, I would like to thank to Dr. Satoru Okayasu and Dr. Masao Sataka at JAERI and Dr. Yukio Kazumata at Nihon Advanced Technology, to make columnar defects by means of heavy ion irradiation.

I greatly appreciate all members of High Magnetic Field Laboratory (Dr. Kiyohiro Sugiyama, Dr. Tetsuya Takeuchi, Mr. Kazuya Taniguchi, Mr. Yasuo Narumi, Dr. Terufumi Hamamoto, Dr. Melike Abliz, Miss Toshiko Yura, and other present and former menbers) and Kadowaki Laboratory (Mr. Tetsu Wakabayashi, Mr. Ryo Nakamura, Miss Yoko Taniwaki, and the others), and all of my friends for their fruitful discussions, encouragement, helps, and cordialities.

Finally, I would like to thank my parents for their economical helps and understandings.

# Published Works

1. H. Hori, M. Furusawa, R. Akimoto, M. Kobayashi, **I. Kakeya**, and K. Kindo, "ESR and magneto-optical measurements in EuTe films and thin films of EuTe/Fe", Physica B **216**, 347 (1996).

2. S. Kawamata, K. Okuda, **I. Kakeya**, K. Kindo, T. Sasaki, and N. Toyota, "ESR study on $\alpha$-(BEDT-TTF)$_2$KHg(SCN)$_4$ single crystal," Synthetic metals, **86**, 2015 (1997).

3. K. Kadowaki, **I. Kakeya**, M. B. Gaifullin, T. Mochiku, S. Takahashi, T. Koyama, and M. Tachiki, "Longitudinal Josephson-plasma excitation in $Bi_2Sr_2CaCuO_{8+\delta}$: Direct observation of the Nambu-Goldstone mode in a superconductor," Phys. Rev. B **56**, 5617 (1997).

4. K. Kadowaki, **I. Kakeya**, and T. Mochiku, "Longitudinal Josephson plasma: A new aspect of superconductivity," Physica B **239**, 123 (1997).

5. **I. Kakeya**, K. Kindo, T. Mochiku, and K. Kadowaki, "Sample size dependence of the Josephson plasma resonance in $Bi_2Sr_2CaCuO_{8+\delta}$", Physica C **282-287**, 1599 (1997).

6. K. Kadowaki, I. Kakeya, K. Kindo, and T. Mochiku, "Direct observation of the Nambu-Goldstone (NG) mode in $Bi_2Sr_2CaCuO_8$ by means of microwave excitation technique," Physica C **282-287**, 2423 (1997).

7. K. Kadowaki, **I. Kakeya**, S. Takahashi, T. Koyama, and M. Tachiki, "Phase coherence and Josephson plasma in $Bi_2Sr_2CaCuO_{8+\delta}$," Physica C **293**, 130 (1997).

8. S. Takahashi, M. Tachiki, **I. Kakeya**, K. Kindo, T. Mochiku, and K. Kadowaki, "Josephson plasma excitation in high-$T_c$ superconductors with finite dimensions," Physica C **293**, 64 (1997).

9. **I. Kakeya**, K. Kindo, K. Kadowaki, S. Takahashi, and T. Mochiku, "Mode separation of the Josephson plasma in $Bi_2Sr_2CaCuO_{8+\delta}$," Phys. Rev. B **57**, 3108 (1998).